Challenge Journal of STRUCTURAL MECHANICS

Vol.1 No.2 (2015)

ISSN 2149-8024

TULPAR ACADEMIC PUBLISHING

Challenge Journal of Structural Mechanics

E-mail: *cjsmec@challengejournal.com*

Web page: *cjsmec.challengejournal.com*

TULPAR Academic Publishing
www.tulparpublishing.com

Challenge Journal of Structural Mechanics

CONTENTS

TULPAR ACADEMIC PUBLISHING

Challenge Journal of Structural Mechanics

Probabilistic assessment of earthquake insurance premium rates for the Gumusova-Gerede Motorway Section

Mehmet Semih Yücemen *, Çetin Yılmaz

Department of Civil Engineering, Middle East Technical University, 06531 Ankara, Turkey

ABSTRACT

A probabilistic model is developed for the assessment of the earthquake insurance premium rates for the structures taking place in the Bolu Mountain Crossing in the Gumusova-Gerede Motorway Section. The model requires two types of studies, namely: seismic hazard analysis and estimation of potential damage to structures. The computations are carried out according to the proposed model by using the seismic hazard results obtained from the time-dependent renewal model and the best estimate damage probability matrices developed in the study.

ARTICLE INFO

Article history:
Received 12 May 2015
Accepted 7 June 2015

Keywords:
Seismic hazard
Earthquake engineering
Earthquake insurance
Damage probability matrix
Risk premium
Insurance premium

1. Introduction

Bolu Mountain Crossing, being a stretch of Gumusova-Gerede Motorway project and named as Section 2, has a total length of 27.2 km, in which 25.6 km of it is motorway and 1.6 km is the connection road. Motorway is designed as two by three-laned and covers earthworks, structures, tunnel and pavement works. Bolu Mountain Crossing, being included within the motorway project along Edirne-Istanbul-Ankara route, which is the main artillery of the highway network in the country, and aiming to meet local and international transportation demands, is the sole section of the project which was completed in 2007. When completed and opened to traffic it ensured the integrity of a very important alignment as a high standard and access control road and safe continuous traffic flow along the motorway.

Within the scope of the road there is one tunnel with two tubes of 2.9 km and 2.8 km long, four viaducts of totally 4.6 km long, three bridges of totally 76 m long, one under-bridge and twelve over-bridges of totally 682 m long. Bolu Mountain Crossing starts from Kaynasli, travels towards east along Asarsuyu Valley, crosses Bolu Mountain through a tunnel and ends at Yumrukaya. The commencement date of the project is 19.02.1990 and initially the expected completion date was 15.12.2006. The initial contract price was 570,500,000 US dollars, whereas later the revised new contract value reached to 670,000,000 US dollars. The contractor of the project is Astaldi S.p.A. and the project is financed by foreign credit.

The earthquake of November 12th 1999 hit the motorway system and caused damages at Viaduct 1 and partial collapse of the Elmalık (Ankara) side of the tunnel for a length of 350 m. The insurance company, after negotiations had agreed to reimburse 105 million US dollars for the losses of the client. After making such a high payment, the insurance company refused the renewal of the earthquake insurance coverage. Consequently, the international insurance companies are invited to make offers for the earthquake insurance coverage of the motorway system. Only one insurance company made an offer with an extremely high premium rate. The client found the offer too high and required a realistic evaluation of the pure risk premium.

In this paper a probabilistic model is presented to obtain a realistic estimate of the earthquake insurance premium for the Bolu Mountain Crossing in the Gumusova-Gerede Motorway Section. The model integrates the information on seismic hazard and the information on expected earthquake damage on engineering facilities in a systematic way, yielding to estimates of the earthquake insurance premium rates.

* *Corresponding author*. Tel.: +90-312-2102459 ; Fax: +90-312-2101163 ; E-mail address: yucemen@metu.edu.tr (M. S. Yücemen)
ISSN: 2149-8024 / DOI: http://dx.doi.org/10.20528/cjsmec.2015.06.012

2. Probabilistic Model for the Estimation of Earthquake Insurance Premium Rates

The assessment of earthquake insurance premium rates requires two types of studies, namely: seismic hazard analysis and estimation of potential damage to structures. In the following, first a brief explanation is provided on these two types of studies and then the model is developed.

2.1. Seismic hazard analysis (SHA)

In the probabilistic sense seismic hazard can be defined as the probability of exceeding different levels of a selected earthquake "severity" or ground motion parameter at a given site and within a given period of time due to expected seismic activity in the region. Many models have been developed for seismic hazard analysis. Most of the earlier models of seismic hazard assessment were based on the assumption that earthquake occurrences are independent events in space and time, and utilized the Poisson model (also known as the classical SHA model) or the extreme value statistics. Later studies considered the temporal or spatial dependence of earthquakes only, like the renewal or Markov models. In recent studies, the occurrence of earthquakes is treated as a space-time process and the spatial and temporal correlations are taken into consideration. A detailed discussion of different stochastic models for seismic hazard analysis is given in (Yücemen and Akkaya, 1996). The probabilistic formulation adopted in this study is based mainly on the time-dependent renewal model. The results obtained based on the classical SHA model are also presented and taken into consideration.

2.2. Estimation of potential seismic damage to structures

Another important component of the model is the assessment of damage to a specified type of structure as a result of earthquakes. Damage is commonly described by a loss ratio that varies with the strength of shaking and type of structure. Due to the uncertainties involved, the damage that may occur during future earthquakes has to be treated in a probabilistic manner. For this purpose damage probability matrices (*DPM*) can be constructed from observational and estimated data (Whitman, 1973; ATC-13, 1985; Gürpınar and Yücemen, 1980; ATC-25, 1991).

A *DPM* expresses what will happen to structures during earthquakes of different intensities. An element of this matrix $P_k(DS, I)$ gives the probability that a particular damage state (*DS*) occurs when the structure of k^{th}-type is subjected to an earthquake of intensity, *I*, where *I* denotes a selected earthquake "severity" or ground motion parameter, like modified Mercalli intensity (*MMI*), magnitude, peak ground acceleration (*PGA*), etc. The identification of damage states is achieved in two steps:

- (i) The qualitative description of the degree of structural and non-structural damage by words. In the most general classification five levels of damage states are specified. These are: No damage (N), light damage (L), moderate damage (M), heavy damage (H), and collapse (C) states. The above categorization of damage states is also used in this study.
- (ii) The quantification of the damage described by words in terms of the damage ratio (*DR*), which is defined as the ratio of the cost of repairing the earthquake damage to the replacement cost of the structure. For mathematical simplicity it is convenient to use a single *DR* for each *DS*. This single *DR* is called the central damage ratio (*CDR*). Based on the opinion of experts in charge of damage evaluation and based on similar studies, the damage ratios corresponding to the five damage states are estimated and are shown in Table 1.

Depending on the type of structures, different *DPM*'s exist. In this study *DPM*'s are developed for the different type of structures taking place at the Bolu Mountain Crossing in the Gumusova-Gerede Motorway Section, namely: viaduct, tunnel, cut and cover and "other structures", consisting of box culverts, embankments, slope supports, pavements, landscaping, river training, etc. Damage probability matrices can be obtained in the most reliable way based on the seismic damage data assessed from past earthquakes and also by using subjective judgment of experts. Techniques based on theoretical analyses for developing *DPM*'s are also available (Whitman, 1973). The form of a *DPM* is illustrated in Table 1.

Table 1. Damage probability matrix.

Damage State (*DS*)	Damage Ratio (*DR*) %	Central Damage Ratio (*CDR*) %	Selected Intensity Parameter (*I*)				
			I_1	I_2	I_3	I_4	I_5
None	0 - 1	0	Damage State Probabilities $P(DS, I)$				
Light	1 - 10	5					
Moderate	10 - 50	30					
Heavy	50 - 90	70					
Collapse	100	100					

2.3. Determination of the pure risk premium

The expected annual damage ratio ($EADR_k$) is used as a measure of the magnitude of earthquake damage to a k^{th}-type of structure that will be built in certain seismic zone and is defined as:

$$EADR_k = \sum_I MDR_k \times (I)SH_I \,, \quad (1)$$

where, MDR_k = average damage ratio for the k^{th}- type of structures subjected to an earthquake of intensity *I* and SH_I = annual probability (seismic hazard) of an earthquake of intensity *I* occurring and affecting the construction site.

It is to be noted that for the computation of *EADR*, one needs only the *MDR*'s corresponding to different intensity levels, rather than the whole *DPM*. The information contained in the damage probability matrix and in the damage ratios can be combined by defining the MDR_k as follows:

$$MDR_k = \sum_{DS} P_k\,(DS, I) \times CDR_{DS}\,, \tag{2}$$

where, CDR_{DS}= central damage ratio corresponding to the damage state *DS*.

After calculating $EADR_k$, the pure risk premium (*PRP*) is computed based on the insured value of the building (*INSV*) under consideration from the following relationship:

$$PRP_k = EADR_k \times INSV\,. \tag{3}$$

2.4. Determination of commercially charged insurance premium

The commercially charged insurance premium (CP_k) for the k^{th}-type of structure is found by increasing the PRP_k by some margin as follows:

$$CP_k = PRP_k/(1 - LF)\,, \tag{4}$$

where, *LF* = load factor which covers the hidden uncertainties, business expenses and a reasonable profit allowance. A common value for *LF* is 0.4 (Gürpınar and Yücemen, 1980). Thus, the commercially charged earthquake insurance premiums will be obtained by multiplying the pure earthquake insurance premium values by an adjustment factor of {1/(1-0.4)}=1.667.

3. Estimation of the Earthquake Insurance Premium Rates for the Gumusova-Gerede Motorway Section

The probabilistic model presented in Section 2 will now be utilized to obtain a realistic estimate of the earthquake insurance premium rates for the structures taking place in the Bolu Mountain Crossing in the Gumusova-Gerede Motorway Section (BMC-GGMS) excluding Viaduct-1. The period of earthquake insurance coverage is assumed to be between January 1, 2003 and the scheduled end of the construction, which was initially set as December 31, 2006, a total period of four years.

3.1. Seismic hazard analysis

In order to use the proposed model for computing the earthquake insurance premium for the structural components of the BMC-GGMS, it is first necessary to carry out a probabilistic seismic hazard analysis for the site where the mountain crossing is located. Extensive probabilistic seismic hazard analyses have been conducted in the past for this site by utilizing the classical seismic hazard model based on the independent Poisson model. These studies are carefully examined and the results of the most recent one (Yılmaz and Erdik, 2000), are summarized in Table 2.

Table 2. Seismic hazard results for the time-independent (memoryless) Poisson process (Yılmaz and Erdik, 2000).

Return Period (years)	*PGA* (g)
9.5	0.084
47.5	0.239
95	0.324
475	0.557
950	0.673
4750	0.985
9500	1.137

In the current study, the probabilistic seismic hazard analysis is conducted based on the time-dependent renewal model, which is believed to represent the current short-time seismic hazard more realistically, in view of the recent major earthquakes that took place in the region. Results of the time-dependent seismic hazard assessment study for the same return periods are presented in Table 3. The details of this seismic hazard analysis can be found in Yılmaz et al. (2003).

Table 3. Seismic hazard results based on the time-dependent (renewal) model.

Return Period (years)	*PGA* (g)	*MMI*
9.5	0.02	IV-V
47.5	0.06	VI
95	0.09	VI-VII
475	0.26	VIII
950	0.36	VIII-IX
2000	0.54	IX
4750	0.60	IX.¼
9500	0.70	IX-X

3.2. Damage probability matrices

In order to compute the *EADR* values from Eq. (1), it is necessary to obtain the *DPM*'s that are applicable for the major structures (i.e. viaducts, tunnel, cut and cover) as well as for the other structures (e.g. box culverts, embankments, slope supports, pavements, landscaping, river training, etc.) taking place in the motorway system. Since no sufficient damage data were available at this site for developing empirical *DPM*'s and the utilization of techniques based on theoretical methods is infeasible, *DPM*'s used in this study are constructed based on expert opinion and *DPM*'s available in the literature for such structures. Although intensity is not a reliable and objective measure of the severity of ground shaking, it is used in this study mainly because earthquake damage to structures is much better correlated with *MMI*. *MMI* scale provides twelve discrete levels of intensity with increasing severity. In this study consistent with the expected seismic activity only the levels V to IX are considered.

In order to estimate damage state probabilities by making use of the subjective judgment of experts, a questionnaire was prepared and sent to seven experienced engineers involved with the design and construction of the "Bolu Mountain Construction Project". Each engineer is asked to fill out the blank *DPM* tables by writing down the subjective probabilities reflecting his opinion on the likelihood of different levels of damage under different intensities.

It is to be noted that in these *DPM*'s two sets of subjective damage probabilities, labeled as UC and NUC, are given. The damage potential for sections under construction (UC) is expected to be considerably higher compared to those that are either completed or not under construction (NUC). This difference is taken into consideration by giving two sets of damage state probabilities under each intensity level. The *MDR* values of these seven engineers are averaged to obtain the "best estimate" subjective *MDR*'s and these are used in the subsequent analysis.

In order to crosscheck the subjective *MDR*'s obtained in this way and to supplement them, a literature survey was conducted. A very useful and dependable reference on this matter is the publications of the Applied Technology Council (ATC), namely ATC-13 (1985) and ATC-25 (1991). The ATC-13 report includes background information, detailed descriptions of the methodology used to develop the required damage/ loss estimates and inventory information, and tables and figures showing the damage/loss estimates developed. Included are damage probability matrices for 78 different facility types as well as estimates of time required to restore damaged facilities to their pre-earthquake usability. In Table G.1 of ATC-13, *MDR* values are given for different intensity levels based on expert opinion for major bridges, tunnels, cut and cover tunnels, highway roadways and pavements and earth retaining structures. The values given in this table correspond to the NUC case.

While ATC-13 provides the *MDR*'s directly, ATC-25 describes the distribution of expected damage in terms of fragility curves based on *PGA*. However, in the case of bridges and highway tunnels, curves showing the degree of damage versus intensity are given. From these curves the *MDR* values corresponding to different intensity levels are extracted for bridges and highway tunnels.

The *MDR*'s based on expert opinion and those obtained from ATC-13 (1985) and ATC-25 (1991) are combined and modified to form the "best estimate" *MDR*'s corresponding to different intensity levels for the viaducts, tunnel, cut and cover and other structures. Here, because of space limitation only the resulting weighted average *MDR* values are given in a tabular form (Table 4). For the details of the computation of these *MDR* values the reader is referred to Yılmaz et al. (2003).

Table 4. "Best estimate" *MDR* values (%) (UC: Under Construction; NUC: Not Under Construction).

Structure Type	*MMI* = V		*MMI* = VI		*MMI* = VII		*MMI* = VIII		*MMI* = IX	
	UC	NUC	UC	NUC	UC	NUC	UC	NUC	UC	NUC
Viaducts	0.003	0	0.014	0.0021	0.66	0.146	3.91	1.02	15.26	10.19
Tunnel	0	0	0.81	0.10	1.79	0.325	4.53	1.16	13.87	5.20
Cut and Cover	0	0	0	0	0.83	0.19	3.26	1.22	14.01	5.72
"Other" Structures	0	0	0	0	0.83	0.25	3.26	1.30	14.01	6.03
Viaducts	0.003	0	0.014	0.0021	0.66	0.146	3.91	1.02	15.26	10.19

Note: UC=Under Construction; NUC=Not Under Construction

3.3. Computation of expected annual damage ratios

In computing the expected annual damage ratios (*EADR*) for the different components of the system, the best estimate mean damage ratio values (Table 4) and the seismic hazard values obtained from the time-dependent model (Table 3) are to be used. The seismic hazard is assumed to be the same at the whole site where the components of the system are located. The resulting *EADR* values, computed from Eq. (1), can be interpreted as the pure risk premiums (*PRP*) to be charged per annum for every one million dollar of insured "property" and are shown in Table 5. The computations are also carried out based on the seismic hazard values obtained by using the independent Poisson model (Table 2). These *EADR* values are also shown in Table 5. As expected the memoryless Poisson model yields higher *EADR* values (about 3 times more) compared to those obtained from the time-dependent renewal model for the UC and NUC cases and for all components of the system. The *EADR* values corresponding to the sections of viaduct, tunnel, cut and cover and other structures that are under construction are respectively, about 2.2, 4.4, 2.8 and 2.5 times higher than the *EADR*'s estimated for the sections that are not under construction in both of the seismic hazard models. This difference in the *EADR*'s is due to the fact that during the construction phase, the viaducts, the tunnel, the cut and cover and the "other" structures will be more vulnerable to earthquake excitation.

As observed in Table 5 the *EADR* values (and consequently the premium rates) are sensitive to the assumptions on seismic hazard analysis and damage probability matrices. In the case of seismic hazard analysis, we believe that the values obtained from the time-dependent model describe the current level of seismic hazard as well as the hazard for the next four years more realistically compared to the independent Poisson process. This is due to the fact that the Poisson model, because of its memoryless stochastic mechanism, ignores completely the large magnitude earthquake that occurred in the region during the

year 1999, whereas the time-dependent (renewal) model takes into consideration the past seismic activity.

In view of the above discussion, it was decided to find a weighted average *EADR*. In other words, although the time-dependent model is preferred to the Poisson model, the more conservative seismic hazard values obtained from the Poisson model are not completely disregarded. A weight of 80% is assigned to the *EADR*'s obtained from the time-dependent (renewal) model and 20% to the *EADR*'s calculated based on the Poisson model. The resulting *EADR*'s are called as our "best estimate" values and are also shown in Table 5.

Table 5. "Best estimate" *EADR* values based on the renewal and Poisson models.

System Component	*EADR* for NUC (10^{-6})			*EADR* for UC (10^{-6})		
	Renewal	Poisson	Best Estimate	Renewal	Poisson	Best Estimate
Viaducts	134.11	428.92	193	298.84	954.06	430
Tunnel	127.37	376.58	178	576.59	1591.45	780
Cut and Cover	99.39	320.13	144	276.07	879.10	397
"Other" Structures	113.49	358.52	163	276.07	879.10	397

Note: UC=Under Construction; NUC=Not Under Construction

3.4. Computation of the pure earthquake insurance premiums

Using the best estimates *EADR*'s given above and the insured values (*INSV*) of the "property", the pure risk premium (*PRP*) values can be computed from Eq. (3). For this purpose the monetary values given by Astaldi S.p.A. are taken as the inputs for the insured values and distinction is made between the work that is completed and work under construction according to the construction schedule. The resulting pure risk premium values corresponding to sections under construction (UC) and sections completed (NUC), as well as the total pure risk premium values are shown in Table 6 for the viaducts, tunnel, cut and cover and "other" structures for each year of the construction period in US dollars. The sum of the annual pure insurance premiums to be paid during the period of 2003-2006 is calculated as 473,811 US dollars.

Table 6. Pure earthquake insurance premium values (in US dollars) for the viaducts, tunnel, cut and cover and other structures corresponding to the different years of construction.

	2003		2004		2005		2006	
Viaducts	*INSV*	*PRP*	*INSV*	*PRP*	*INSV*	*PRP*	*INSV*	*PRP*
NUC	35,385,001	6,830	58,608,961	11,312	112,209,953	21,657	170,479,915	32,903
UC	23,223,960	9,987	53,600,992	23,049	58,269,962	25,056	827,498	356
Total *PRP*		16,817		34,361		46,713		33,259
Tunnel	*INSV*	*PRP*	*INSV*	*PRP*	*INSV*	*PRP*	*INSV*	*PRP*
NUC	127,327,630	22,665	145,012,196	25,813	191,527,234	34,092	241,886,927	43,056
UC	17,684,566	13,794	46,515,038	36,282	50,359,693	39,281	18,252,897	14,238
Total *PRP*		36,459		62,095		73,373		57,294
Cut And Cover	*INSV*	*PRP*	*INSV*	*PRP*	*INSV*	*PRP*	*INSV*	*PRP*
NUC	0	0	12,867,211	1,853	18,631,805	2,683	18,631,805	2,683
UC	12,867,211	5,109	5,764,595	2,289	0	0	0	0
Total *PRP*		5,109		4,142		2,683		2,683
"Other" Structures	*INSV*	*PRP*	*INSV*	*PRP*	*INSV*	*PRP*	*INSV*	*PRP*
NUC	108,672,475	17,714	110,358,330	17,989	128,246,419	20,905	138,512,810	22,578
UC	1,685,855	670	17,888,088	7,102	10,266,391	4,076	19,619,379	7,789
Total *PRP*		18,384		25,091		24,981		30367
Total Pure Risk Premium:		76,769		125,689		147,750		123,603

Note: *INSV*=Insured Value; *PRP*=Pure Risk Premium; NUC=Not Under Construction; UC=Under Construction

4. Conclusions

Using the best estimate seismic hazard values together with the best estimate *MDR* values, the total earthquake insurance premium for the period of 2003-2006 is computed as 473,811 US dollars. This amount corresponds to the pure risk premium, reflecting only the risk of damage due to earthquakes and has to be increased to account for hidden uncertainties, business expenses and a reasonable profit allowance for the insurance firm. This adjustment can be done by using Eq. (4) with a load factor, $LF = 0.4$, yielding to an adjustment factor of 1.667. With this adjustment, the corresponding commercially charged earthquake insurance premium value for the period of 2003-2006 will be: 789,843 US dollars.

The best estimate *EADR* values computed in this study and the resulting earthquake insurance premiums obtained under different assumptions are within our expectations and are consistent among them. We also emphasize on the existence of two favourable factors that have decreased the seismic risk of the system and consequently the insurance premiums, namely: the upgrading of the seismic design criteria after the 12 November 1999 Düzce earthquake has reduced the seismic vulnerability of the system considerably and also the probability of a large magnitude earthquake occurring in the region during the next four years (construction period) has decreased significantly due to the energy released by the 12 November 1999 Düzce earthquake (Lettis and Barka, 2000).

Acknowledgements

The authors thank Prof. Dr. Mustafa Erdik of Boğaziçi University for providing the seismic hazard results and the Turkish Office of Astaldi S.p.A. for providing the general and technical information concerning the Gumusova-Gerede Motorway Section.

References

ATC-13 (1985). Earthquake Damage Evaluation Data for California. Applied Technology Council, Funded by FEMA, USA.

ATC-25 (1991). Seismic Vulnerability and Impact of Disruption of Lifelines in the Conterminous United States. Applied Technology Council, Funded by FEMA, USA.

Gürpınar A, Yücemen MS (1980). An obligatory earthquake insurance model for Turkey. *Proceedings, International Conference on Engineering for Protection from Natural Disasters, Asian Institute of Technology*, Bangkok, Thailand, 895-906.

Lettis W, Barka A (2000). Geologic characterization of fault rupture hazard Gumusova-Gerede Motorway. Technical Report prepared for Astaldi S.p.A.

Whitman RV (1973). Damage probability matrices for prototype buildings. Seismic Design and Decision Analysis Report No.8, Department of Civil Engineering Report R73-57, MIT, Cambridge.

Yılmaz Ç, Erdik M (2000). Memo submitted to Astaldi-Bayındır JV.

Yılmaz Ç, Yücemen MS, Erdik M (2003). Probabilistic assessment of earthquake insurance premium rates for the Bolu Mountain crossing in the Gümüşova-Gerede Motorway Section. Technical Report, METU, Ankara.

Yücemen MS, Akkaya A (1996). A comparative study of stochastic models for seismic hazard estimation. *Land-Based and Marine Hazards*, Kluwer, Netherlands, 7, 5-24.

Challenge Journal of Structural Mechanics

Use of optical fibre technology to measure structural performance

Laurie F. Boswell *, Brett McKinley

Department of Civil Engineering, School of Engineering and Mathematical Sciences, City University, London EC1V 0HB, UK

ABSTRACT

Structural monitoring using optical fibre technology may be undertaken to establish the long-term behaviour of structures, components and materials of construction. Condition monitoring may be used as an aid to repair and strengthening schedules. The establishment of material durability is also part of the monitoring process. The paper describes and discusses the application and development of the use of optical fibres to monitor structures. Examples have been given in which strain, temperature and moisture content have been determined for structural elements and materials of construction. Of particular interest is the use of an optical fibre monitoring system to determine the performance of an actual bridge, which has been subjected to controlled loading conditions. The results, which have been described, demonstrate the enormous potential to monitor structures using optical fibres.

ARTICLE INFO

Article history:
Received 14 May 2015
Accepted 3 June 2015

Keywords:
Structural monitoring
Optical fibres
Bridge maintenance
Durability
Composite construction

1. Introduction

There has been considerable effort in recent years for increasing the understanding of the long-term behaviour of civil engineering and other structures through the use of advanced monitoring techniques using optical fibre based instrumentation (Ferdinand et al., 1994; Measures et al., 1995; Ning et al., 1998; Grattan and Meggitt, 2000a; Grattan and Meggitt, 2000b; Betz et al., 2002; Maurin et al., 2002).

This paper highlights some of the recent research activity conducted at City University in collaboration with other national and international institutions. This activity has seen the establishment of monitoring systems for strain and temperature, which have been deployed in steel, concrete and composite structures in the laboratory and concrete, steel-concrete composite and polymer composite structures in the field.

The existing ability to monitor extensively large structures has been limited by the available strain sensors which rely on electrical instrumentation that is time consuming to install, requires a large amount of electrical inter-connections, can be difficult to distribute over large distances and to embed during the construction process. The quasi-distributed, multiplexed optical fibre sensor systems developed will provide invaluable information regarding the stress relief, shrinkage, creep, dead loading, post tensioning and structural degradation manifested by the appearance of cracks, fissures and corrosion. Further, it will permit the possibility for monitoring the static and dynamic loading history that is essential in both setting controlled maintenance procedures and scheduling and for structural design assessment. This provides a powerful means to determine the service quality and safety in a continuous fashion, both during and after construction, throughout the structures lifetime and especially approaching its designed life-span and following unusual phenomena such as subsidence, earth-quakes, impact, high wind, fire and flooding to avoid catastrophic failure.

Considerable attention has been directed towards the possible application of optical fibres for civil engineering use. Although a range of possible transducer principles has been investigated including strain, temperature, acceleration, moisture and various chemicals, the development of the in-fibre Bragg grating has provided a step forward in the potential capabilities of the technology for large structure monitoring. This and compatible temperature systems has been the basis of research activity at City University.

* *Corresponding author*. Tel.: +44-20-70408140 ; Fax: +44-20-70400119 ; E-mail address: l.f.boswell@city.ac.uk (L. F. Boswell)
ISSN: 2149-8024 / DOI: http://dx.doi.org/10.20528/cjsmec.2015.06.011

2. Optical Fibre Instrumentation Technology

2.1. Strain measurement

The Bragg grating structure is written as a periodic variation in the refractive index of a photosensitive fibre providing a strain and temperature dependent optical filter. The grating effectively acts as a wavelength specific mirror whilst allowing all other light to pass almost perfectly in order to interrogate further gratings if used in a multiplexed system, Fig. 1.

The grating forms the basis of optical strain measurements, which can be monitored by measuring the changes in the wavelength spectrum of the reflected optical signal. It allows an absolute measurement that is independent of potential intensity fluctuations caused by light source variation, fibre bending loss or connector attenuation. It is simple and encapsulates all the benefits of optical fibre technology. This is a major advantage of Bragg grating sensors for long term monitoring in large engineering structures where the service lifetime of the structure is considerable. As passive optical sensing devices, immune to electromagnetic interference, Bragg gratings encapsulate all the advantages of fibre optic sensors (Grattan and Meggitt, 2000a). As they are written directly into the fibre, they are hence unobtrusive and small in size (barely visible in Figs. 2 and 3), allowing easy sensor embedment for smart structure applications. In addition, several gratings can be written in series along a single fibre at different wavelengths for quasi-distributed sensing, a major advantage of the use of this approach.

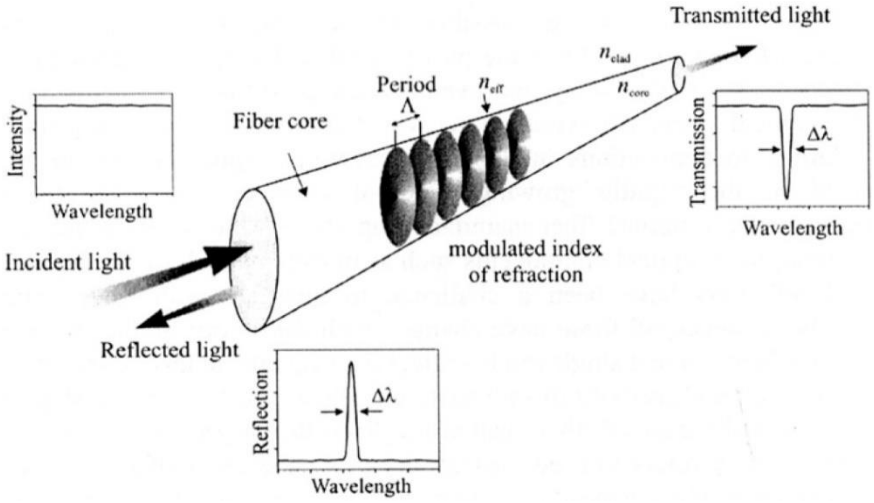

Fig. 1. Schematic representation of operation of FBG based strain instrumentation.

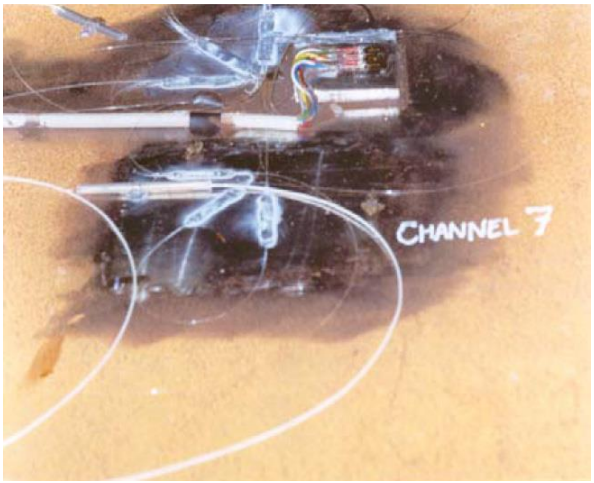

Fig. 2. Installed optical fibre sensors on steel structure.

Fig. 3. Strain gauges and optical fibre sensors on failed concrete specimens.

2.2. Temperature determination

The prime aim of recent activity is the development of a fibre-based sensor system for temperature monitoring, using a technique complementary to the Bragg grating based system for strain monitoring.

This would allow the measurement of temperature during the exothermic process of concrete curing; and would provide a mechanism to compensate changes in the strain measurements within a structure caused by changes in temperature. The method proposed requires the use of small temperature-sensitive elements of

doped fluorescent fibre, the fluorescence decay time of which can be monitored as a function of temperature. This technique is sensitive over the whole range of temperatures to be measured in the structure (-20 to +300°C) and utilises the same wavelengths as the strain measurement system, to simplify the optical system used. The signal processing can be constructed using readily available electronic components, to yield a precision of ±2°C with the probe in-situ. Fig. 4 shows the probe design.

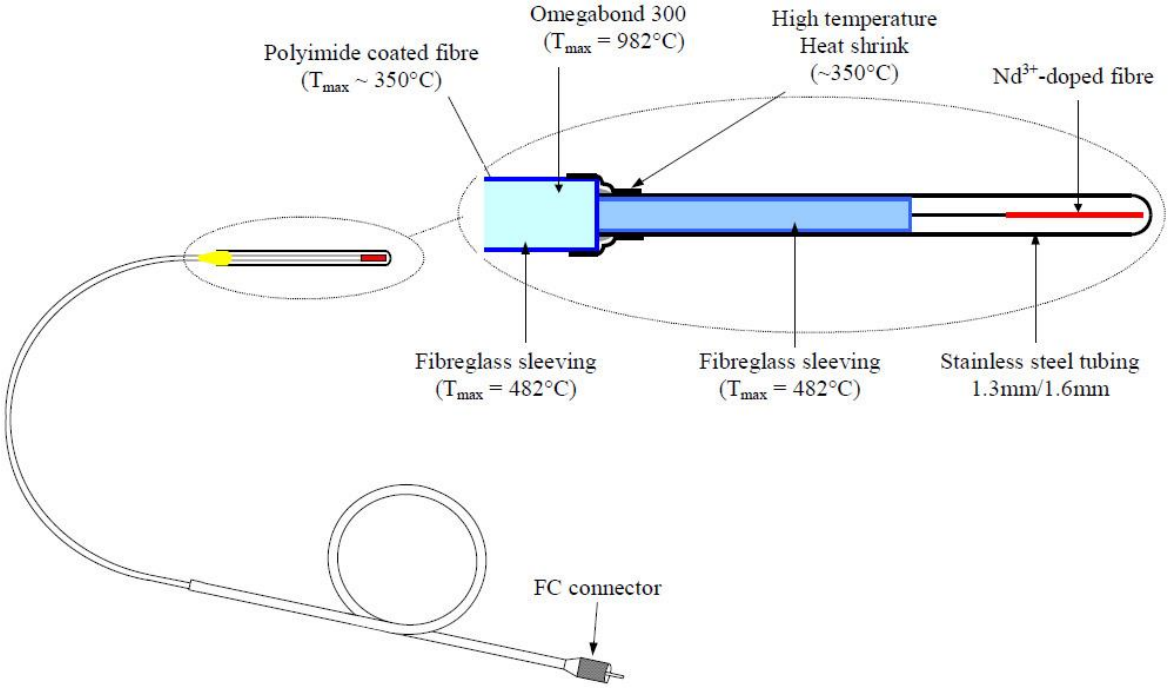

Fig. 4. Design of optical fibre temperature probe for temperatures up to 350°C, and installed in a reinforcement cage.

3. Applications

The application of optical fibre sensors to civil engineering structures has been developed and proven through extensive laboratory testing prior to being implemented on a number of bridges made from a range of materials including steel, concrete and polymer composites. Some examples of the work are given.

3.1. Strain and temperature measurements for concrete beams

A series of tests using reinforced concrete beams was used to evaluate the durability of the optical fibre sensors exposed to high temperature. The dimensions of the beams were: length 850 mm, height 85 mm and width 60 mm and were tested using existing apparatus capable of applying structural loads to failure and thermal loads to 800°C. This work was carried out using the optical fibre based temperature sensor as well as FBG optical fibre sensors for strain and temperature, electrical resistance strain gauges and thermocouples.

Initially the beam was loaded up to approximately 10kN (40% static capacity) at ambient temperature, during which the temperature of the beam was monitored using both a K-type thermocouple and an optical fibre temperature probe. After the initial loading of the concrete beam the temperature of the beam was raised in stages of approximately 100°C, up to a maximum of 300°C, with the beam temperature being allowed to stabilise for each heating stage. Once the beam had stabilised at each of the set temperatures the applied load was increased back to 10kN. The reduction in the load applied to the beam during each of the heating stages was due to expansion of metal components in the test rig.

Some small changes in temperature readings that occurred during the test were accompanied by failure of two strain gauges mounted on the steel reinforcement of the concrete beam, indicating that a substantial change in the beams' mechanical properties has occurred. Further evidence of this fact was indicated when visual inspections of the beam upon later removal from the test rig found flexural cracks of the concrete in the middle section of the beam allowing more direct and rapid heating of the area around the sensors.

FBG sensors were also used to measure strain and to compensate for temperature variations within concrete beams subjected to structural and thermal loads. Two FBG sensors were installed in the concrete beam with one attached to the steel reinforcement and the other inserted into a glass capillary in order that it would only be subjected to thermal variations and was located adjacent to the first sensor. The strains measured by the FBG sensor on the reinforcement were successfully compensated as indicated by a comparison with the conventional gauges, Fig. 5.

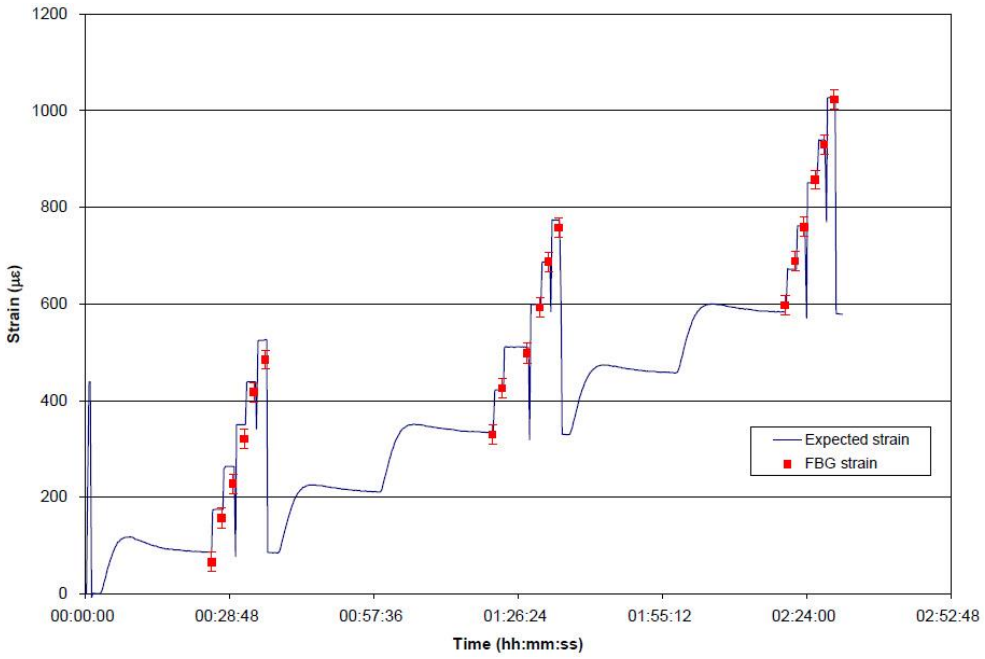

Fig. 5. Comparison of temperature compensated FBG sensors to strain gauge measurements.

3.2. Durability of concrete cylinders

A programme of work to characterise and catalogue the effect of damage development in dry and preconditioned concrete cylinders and cubes as a function of applied load and curing environment was undertaken. The specimens were cured under four different conditions and then loaded to a series of pre-defined levels and then unloaded, sectioned, inspected and the results catalogued. The damage behaviour as a function of load and environment was correlated to the output from the FBG sensors attached to the cylinders and to ultrasonic pulse velocities, which is a common method of measuring relative, in-situ degradation of concrete structures.

The measured ultrasonic pulse velocities indicate change from approximately 30% of the concrete cube strength. The changes at this level were within the noise variations of the system and would only be detectable after many readings. The method was, therefore, assessed to be only of use once significant load had been placed on the specimen.

The data from the FBG sensors was correlated to the behaviour of concrete cylinders under load before and after compensating for non-axial loading. This showed significant difference in the stress- strain behaviour between the concrete cylinders cured under the different environmental conditions. The strength of the concrete under the different curing regimes is as expected based on the amount of moisture available for concrete hydration. The specimens cured under control conditions achieved near design 28 day strengths of 40 N/mm^2 with the higher humidity levels causing increased strength.

The samples cured in air had reduced strength. There was a clear change in the stress-strain response between the specimens, as measured using the optical fibre sensors, which is easily detectable from low level and, therefore, significant better than any visual inspection.

3.3. Fatigue tests on concrete beams

A series of tests using reinforced concrete beams were subjected to dynamic fatigue loading at various load levels to determine the performance of sensors at low loading (up to 10^6 cycles), intermediate and high loading (<1000 cycles). A single FBG optical fibre sensor together with two electrical resistance strain gauges was used for monitoring the compression strains at the centre of the test specimens, Fig. 3. The design of the beams is such that failure will occur by concrete compression at the mid span.

A beam loaded at low levels was seen to steadily increase the strain range response throughout the test until after 6.5x10^5 cycles, where it remained steady. The specimen did not fail and the test was halted after 10^6 cycles. Specimens that were highly loaded showed rapid degradation of the beam by the continuously increasing strain range and increasing residual strain within the beam. Some sudden drop-offs in the signal were caused by the wavelength of the reflected light from the Bragg falling outside the range of the detection system indicating the need to match the Bragg sensor to the requirements.

Fig. 6 shows the number of cycles to failure from nine concrete beam tests, which have been subjected to various load ranges. Two of the specimens did not actually fail and are highlighted by the dotted lines indicating when the failure might be expected to occur. Some degree of scatter has occurred in the results, which is attributed to the nature of concrete. When results from the beam tests unexpectedly occurred, concrete cube tests were taken but little discrepancy in their results was ever found. Fig. 6 shows that most of the scattered results occurred when loaded around 50 to 60% of the maximum static capacity. The results from this work have enabled a fatigue curve to be generated for concrete in compression, although this only applies to one concrete specification.

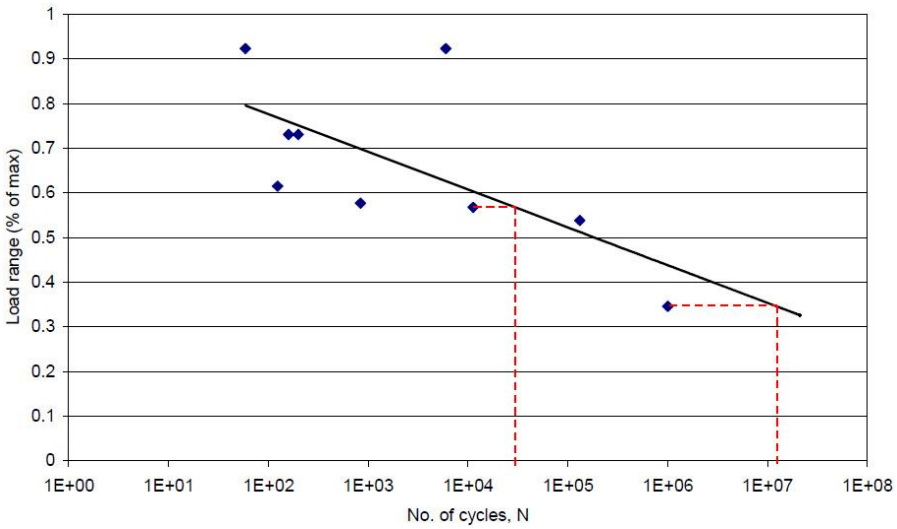

Fig. 6. Fatigue curve for concrete beam specimens tested.

3.4. The measurement of moisture absorption in concrete

A fibre-optic based humidity sensor has been developed and used for the measurement of moisture absorption in concrete. The sensor was fabricated using a fibre Bragg grating (FBG) coated with a moisture sensitive polymer. To investigate the use of this sensing technique for the detection of moisture ingress in concrete, the sensor was embedded in various concrete samples of different water to cement ratios which were then immersed in a water bath. A direct indication of the humidity level within a sample is given by the shift of the Bragg wavelength caused by the expansion of the humidity-sensitive material coated on the fibre. The sensor itself exploits the inherent characteristics of the FBG, with its operation being based on the strain effect induced in the Bragg grating, through the swelling of the polymer coating.

It was found that optical fibre based humidity sensors of this type form a basis for determining the changes in the moisture content in different concrete samples, indicating potential new applications of the sensor system to ensure the integrity of civil engineering structures in which they are used.

Due to the nature of concrete structures and their exposed environmental conditions (e.g. a bridge), corrosion can occur internally without this being evident from the outside. This is often due to the ingress of water corroding the reinforcements, which is hastened by the salts and chlorides dissolved in it. Concrete itself is made up by simply mixing cement, aggregate and water together, but its properties and strength reside in the specifics of the quantities used and the way that it is cured. The durability of concrete however lies in its ability to withstand the process of deterioration to which it is exposed. This may be due to both chemical attack and the repeated 'freeze-thaw' effects of water absorbed into the concrete.

There are three principal fluids that can enter and damage the concrete: water (pure or carrying chemicals) carbon dioxide and oxygen. They travel through the concrete primarily via the hydrated cement. The permeability is defined as the ease with which a fluid flows due to the pressure differential while the porosity is a measure of the proportion of the total volume of concrete occupied by pores formed in the structure. If the porosity is high and the pores are interconnected, the permeability will also be high. There can however, also be diffusion and sorption of the concrete.

As tests for permeability of concrete have not been standardized, the permeability values quoted from different sources may not be readily comparable. The conditioning of concrete in service is nearly impossible as there is no generally accepted method, but this does not detract from the need to perform effective monitoring, and work undertaken here addresses this issue.

The humidity sensor scheme used in this work is based on an expansion principle, using a fibre Bragg grating (FBG). The influence of humidity on a polymer-coated FBG was first discussed by Giacarri et al. (2001), and the technique described for humidity detection was further explored by various authors (Laylor et al., 2002; Yeo et al., 2005). In summary, the humidity sensor is created by coating an optical fibre containing an FBG with a moisture-sensitive polymer that absorbs the moisture present, causing it to swell. This swelling effectively stretches the fibre and thereby causes a strain in the FBG contained with it. This consequently changes the wavelength of the reflected signal of the FBG which can be monitored using an optical spectrum analyser or any other similar wavelength-based interrogation technique. Different chemical coatings will have different response to humidity change. Polyimide was used as the coating material as a linear response is preferred.

In use, samples of concrete with a humidity sensor embedded inside were placed in water and the rate of water absorption was measured from the rate of the humidity change resulting in the concrete.

Due to the fragile nature of the fibre into which the sensitive FBG was written and the need to use it as a probe, it was appropriate to find a way to protect the sensor from damage in use in the concrete specimens examined. It was found to be best achieved by using a thin metal tube to cover the sensor and having holes drilled along each side to allow the free circulation of fluids. This

was fixed to the sensor using epoxy resin. The probes constructed could also require temperature compensation in some applications, and this could be done by monitoring the temperature (e.g. using the approach of previous work by some of the authors (Pal et al., 2004) and applying a correction, as required, for temperature changes. However, the tests reported in this study were carried out in a water bath, at controlled temperatures, to minimize the need for correction and maintain comparable conditions for the different concrete samples evaluated.

Standardized cylindrical samples of concrete were made with a diameter of 100 mm and depth 100 mm (Fig. 7(a)). They were cast with a 4 mm diameter hole at the centre, with a depth of 80 mm into which the sensor could be placed. The mix was manufactured using ordinary Portland cement (OPC) CEM-I 42.5 conforming to BS EN 197 Part 1 (BS EN 197-1:2000) manufactured by Lafarge (previously Blue Circle Cement Ltd.). The mix designs of the specimens were based on the guidelines from the BRE (Building Research Establishment) in the UK (BR106:1988) and have a mix proportion ratio of 1:2:2 for cement, fine and coarse aggregate. Sharp sand with a maximum coarse size of 5 mm was used as the fine aggregate and river gravel with a maximum coarse size of 10 mm was used as the coarse aggregate. To allow for different response time in saturating a specimen, three different mixes were made, with water/cement (w/c) ratios of 0.5, 0.6 and 0.7 respectively. The concrete cylinders were removed from their casts after a period of 24 hours, after which they were left to cure in a water tank for 28 days at ~20°C and finally, removed and left to dry under laboratory conditions with an average temperature of 16°C for approximately one month.

To obtain comparative data, concrete cubes of dimensions 100 mm x 100 mm x 100 mm were cast from each mix to determine the average mix strength. Four cubes from each mix were cast and their compressive strengths after 28 days were measured using a compression test machine. Data from this test are shown in Table 1. For each test, a sample was set up with the probe placed in the centre of the concrete cylinder (Fig. 7(b)).

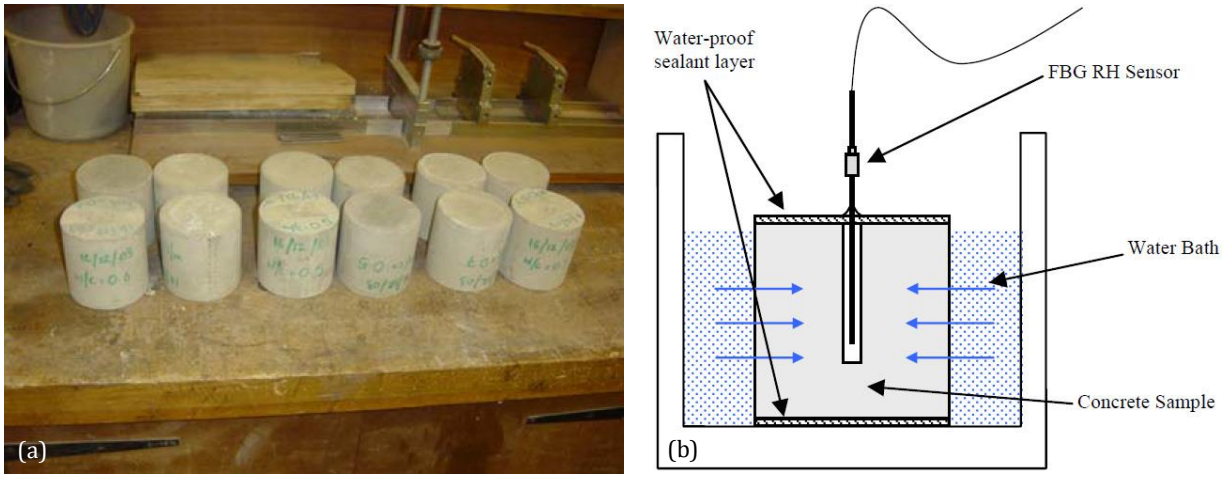

Fig. 7. a) Standardized cylindrical concrete samples of different water/cement ratio.
b) Schematic of a concrete sample with a RH sensor in the water bath.

Table 1. Compressive strength of the concrete samples of different water/cement ratios.

Mixture (Water/Cement Ratio)	Sample	Compressive Strength (N/mm^2)	Average
0.5	a	36.4	36.5
0.5	b	36.9	
0.5	c	36.5	
0.5	d	37.3	
0.6	a	25.6	26.9
0.6	b	27.7	
0.6	c	27.1	
0.6	d	27.3	
0.7	a	14.1	14.4
0.7	b	14.3	
0.7	c	14.8	
0.7	d	14.3	

Results for a series of humidity measurements, which show the response of the same sensor to different samples (pre-conditioned at different temperature and drying duration) when immersed in water bath, are shown in Figs. 8-11. This investigation of the concrete samples, through tests with the probe itself was carried out to determine its reaction to the change of moisture content within the concrete.

In summary, it can be clearly seen that from this laboratory study, fibre optic based humidity sensors can be used effectively to monitor moisture changes in concrete. It has been shown through the data produced using several different concrete samples subjected to water ingress that concrete can be monitored effectively in this way.

3.5. Bridge monitoring using an optical fibre monitoring system

Mjosundet Bridge is located in Aure, about 50 kilometres north of Kristiansund on the west coast of Norway and in the County of More and Romsdal. The bridge is a five span continuous composite bridge, Figs. 12 and 13. It is practically symmetrical with two end spans of 41m, two intermediate spans of 82m and a centre span of 100m giving a total length of 346m. Both ends are supported on concrete abutments with bearings providing free movement in the horizontal direction. Piles support the two central columns (axis 3 and 4) and the intermediate columns are founded directly on to rock. All connections between the bridge deck and columns are monolithic.

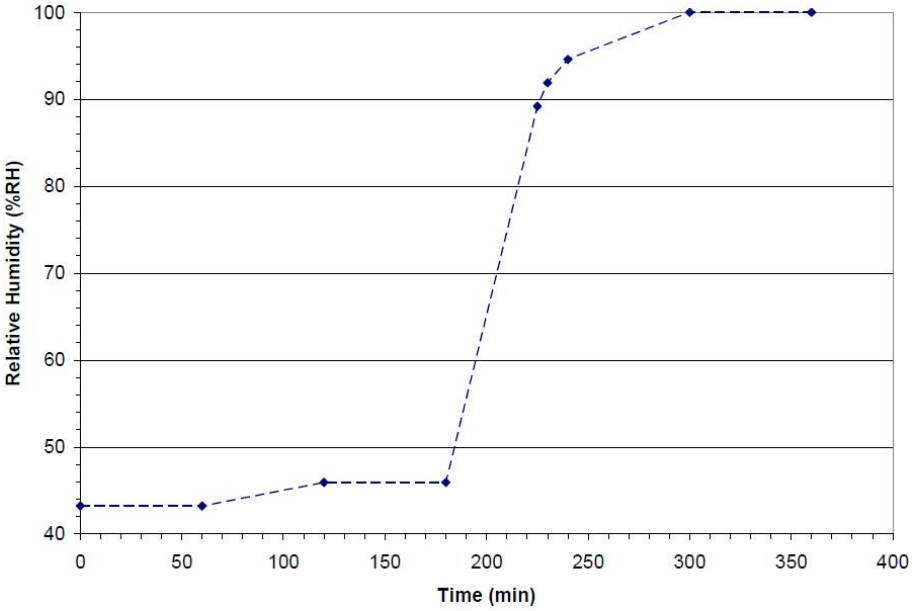

Fig. 8. Sample with w/c ratio of 0.6, oven dried at 80°C for 24 hours.

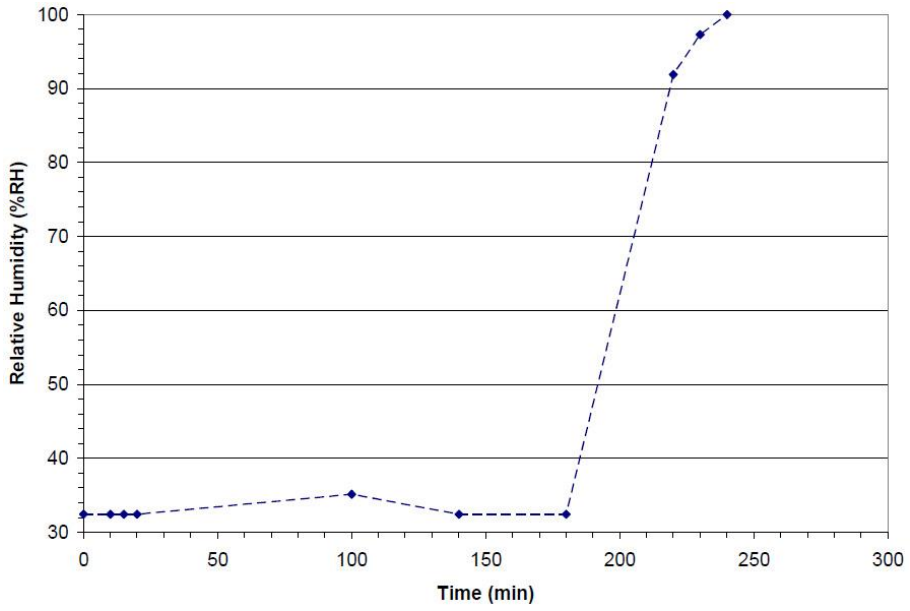

Fig. 9. Sample with w/c ratio of 0.7, oven dried at 80°C for 24 hours.

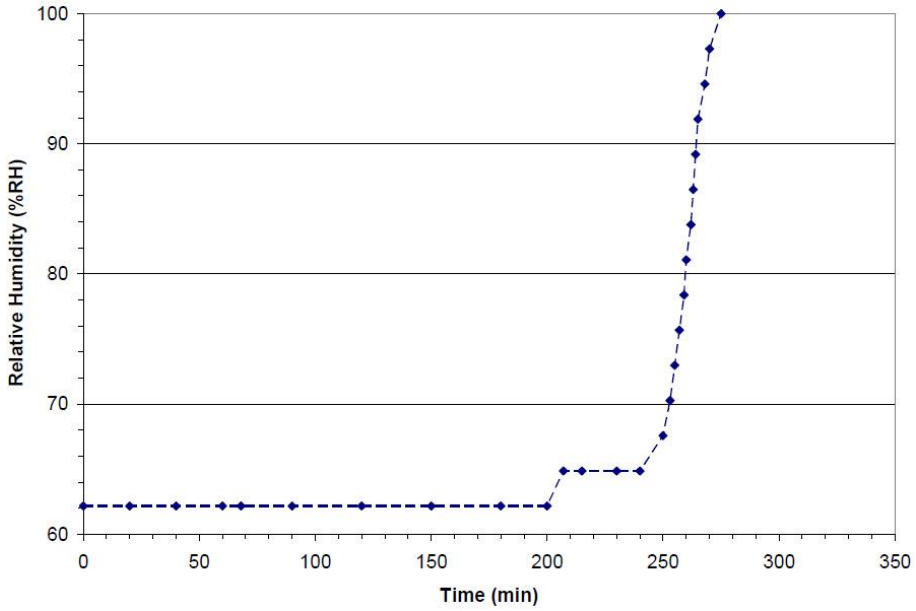

Fig. 10. Sample with w/c ratio of 0.5, oven dried at 95°C for 48 hours.

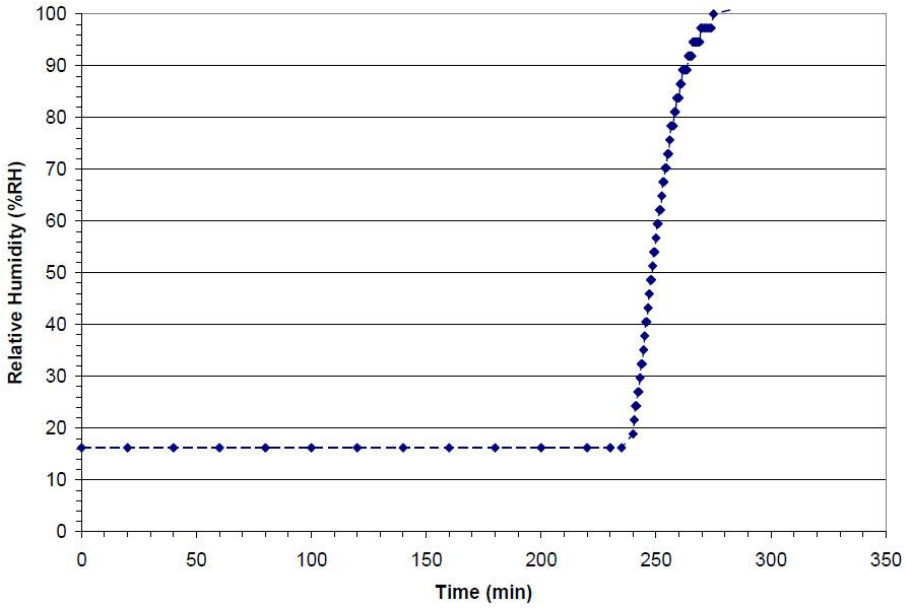

Fig. 11. Sample with w/c ratio of 0.7, oven dried at 95°C for 48 hours.

The deck is made of concrete, fixed with shear connectors to the top flanges of the steel box. The concrete deck is approximately 9.1 m wide and 0.3-0.4 meters thick, while the steel box varies in height from about 2.5 meters to about 4.2 meters (Fig. 14). The bottom plate, webs and flanges of the steel box all have various thicknesses (14-60 mm). The concrete deck is not visible inside the box-girder as it was cast on corrugated plate permanent formwork, supported on the steel flanges.

The construction of a model of Mjosundet with a section scale of one-fifth and length scale of one- twentieth has been completed, Fig. 15. For the purpose of the laboratory model, only the spans between sections 3 and 5 of Mjosundet were modeled. These are the central and one adjacent side spans, with the central span being the longest. This structure was successfully used to test and implement the hardware and software for the acquisition of data. The structure was tested under a series of static and cyclic load tests within the elastic range to strain levels equivalent to those expected from the field trial.

It was considered important to provide a comparison with existing strain measuring techniques with more recently developed of optical fibre monitoring techniques. Two systems were, therefore, assembled that would run as a single unit during the field trial tests. The first system was an electrical (ERSG) system used to monitor the strain gauges that were attached to the structure. The second system was the optical fibre based fibre Bragg grating (FBG) system, which had been specifically developed to be capable of monitoring up to 100 sensors. In order to provide further information for the strain measurements, a separate finite element study was conducted.

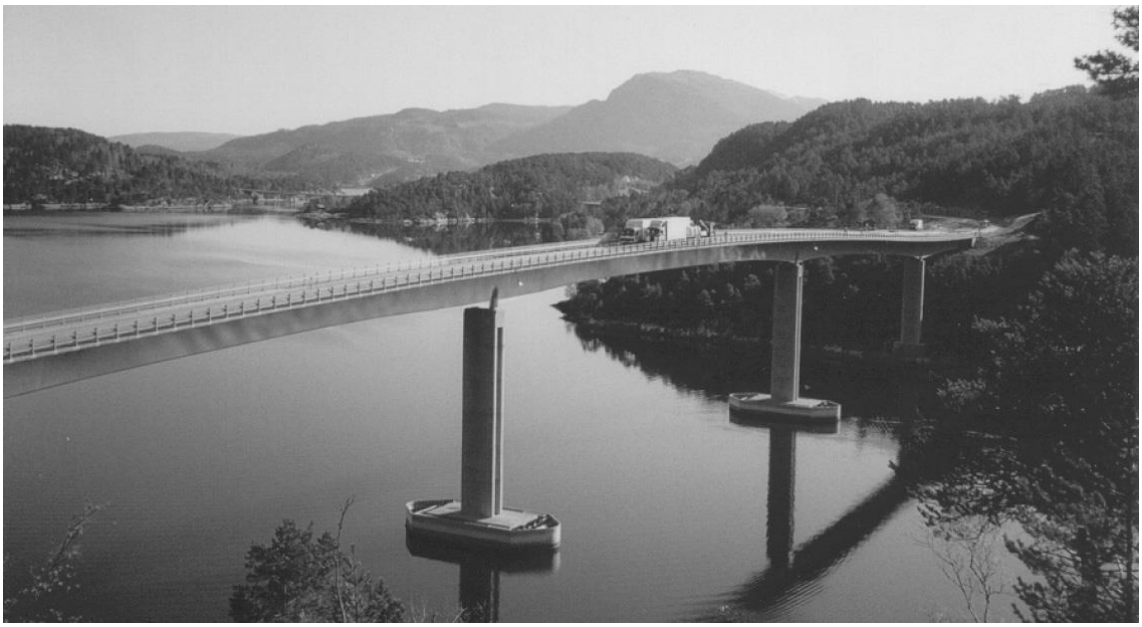

Fig. 12. Mjosundet Bridge used for the field trials.

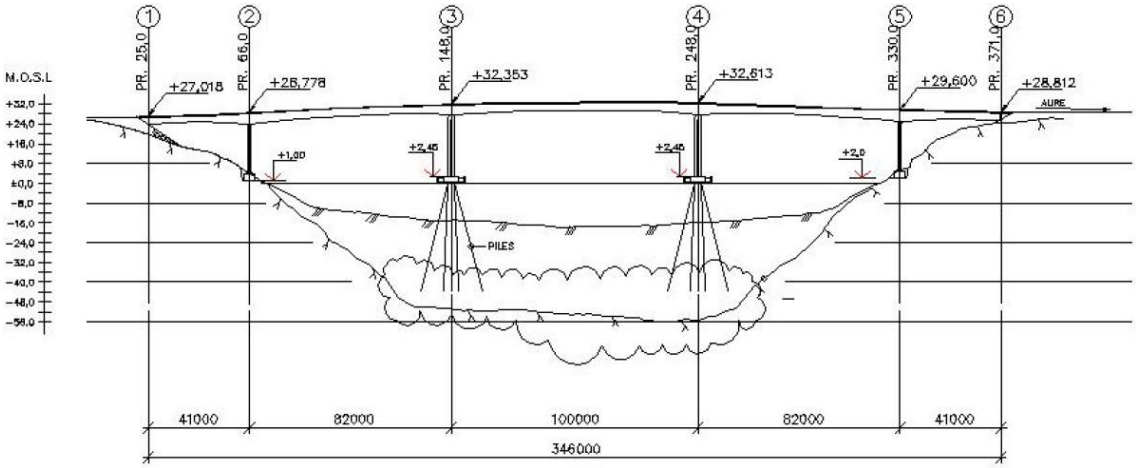

Fig. 13. Drawing of bridge with axis and profile numbering.

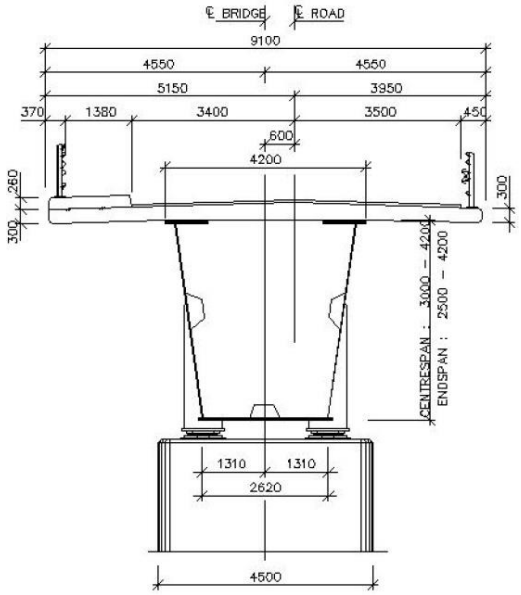

Fig. 14. Typical cross-section of bridge.

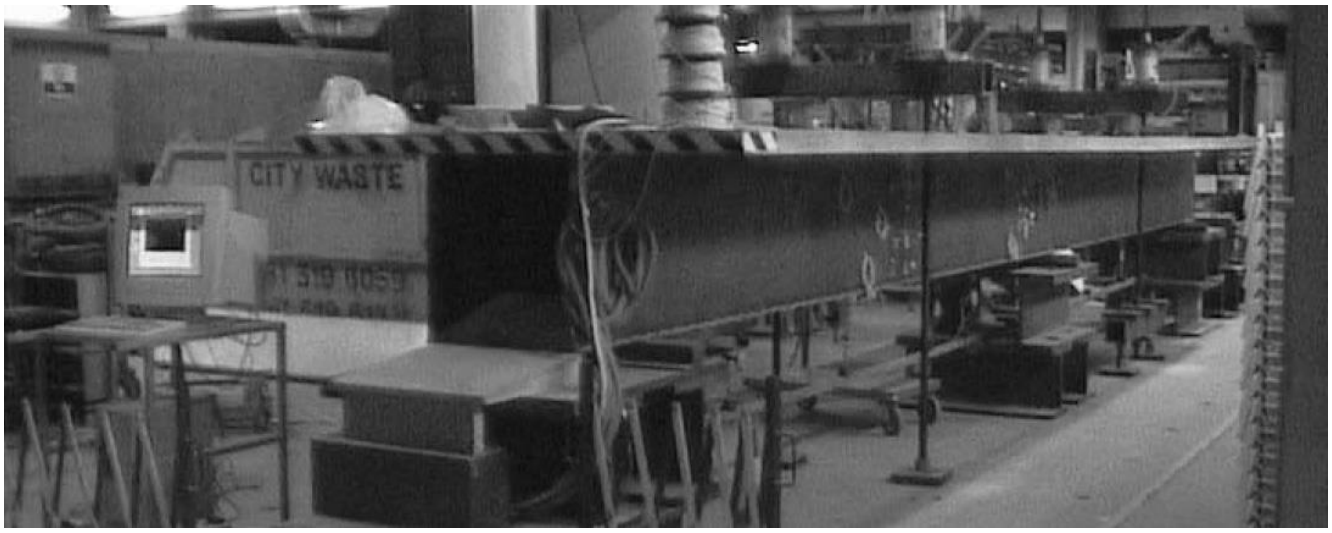

Fig. 15. Large-scale bridge model in laboratory at City University.

The bridge was instrumented on two cross sections with electrical resistance strain gauges (ERSG's) and fibre optic Bragg grating sensors (FBG's). The placement of the instrumentation was determined by a finite element analysis in order to provide guidance to the most effective positions. These positions were determined as having the highest strains within the steel structure, which would then be used within a fatigue analysis. This was a primary objective of the research, rather than aiming to describe the performance of the whole structure. Three locations at each section within the structure were monitored in order to assess the bending strains at the centre of the bridge and the shear strains close to one of the supports of the middle span of the bridge. The three monitored locations near the support were placed 0.5, 1.0 and 1.5 m measured up from the lower flange. The remaining three monitored locations were placed at centre of the bridge with two being on the bottom flange (0.4 m and 0.8 m from the web) of the bridge and the other placed at the lower edge of the web, 0.22 m up from the flange. The arrangement of the instrumentation was such that an ERSG could be used to verify the measurements of a corresponding FBG and to calibrate the finite element model. The remaining FBG's would then be assessed using the finite element model. The duplication of sensors at any position on the structure was conducted in order that the repeatability of any sensor measurements could be determined as well as providing redundancy within the data set.

Field trial testing was conducted on three individual occasions, together with continuous monitoring between each test. Each of the individual field trials consisted of a number of static and dynamic tests where the structure was subjected to loads from a number of parked or moving vehicles, respectively. The static tests consisted of three loading states where the structure was subjected to maximum sagging and hogging moments and maximum shear forces up to the design load levels. A series of discrete load and no-load events allowed data to be recorded continuously for the test and easily processed afterwards. During the dynamic tests, the vehicle was driven across the structure at a steady velocity. A number of these tests also involved the vehicle being driven over a plank in order to induce shock vibrations and, hence record data during natural frequency oscillations.

4. Comparison of Theoretical and Acquired Data

Fig. 16 shows a comparison of data acquired from both measurement systems with that obtained from the finite element analysis. A comparison is made for one load case and each figure represents the longitudinally aligned sensors from one of the monitored cross sections.

From Fig. 16, it is clear to see the bending of the structure with the neutral axis located approximately 2.5 m to 2.75 m above the lower flange of the structure. The data from the two measuring systems agree well with each other, which are slightly underestimated by the finite element analysis. However, since the gradients of these lines are equivalent it has been assumed that this difference is due to an axial force in the structure during the load test caused by fixture of the deck between the columns. The difference in the data is none the less very similar.

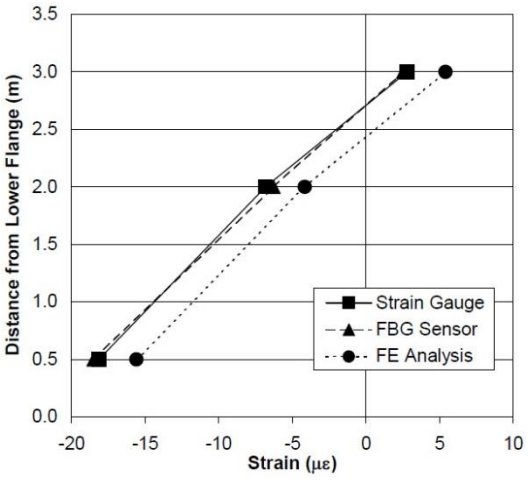

Fig. 16. Comparison of data at support location (high shear loads).

5. Conclusions

FBG and fluorescence-decay optical fibre based sensor systems have been developed and assessed for the monitoring the structural integrity of civil engineering structures. The development of suitable surface and embedment techniques and protection systems for using optical fibre sensors in the field has been developed and validated using concrete cylinder and reinforced concrete beam tests. The sensors have been subjected to static, fatigue and thermal loading within reinforced concrete test structures and have shown excellent results throughout. The sensors attached directly to structures have correctly measured strain and temperature to ±1 microstrain and ±2° centigrade, respectively and dynamic strains of approximately 3000 microstrain whilst monitoring fatigue loading of reinforced concrete beams. The sensors have also monitored the stress-strain response of concrete specimens subjected to various environmental conditions. The results achieved indicate that the optical fibre probes are robust and can withstand large and sudden changes in the load applied to the test structure.

A particular interesting development has been the application to the measurement of moisture ingress in to concrete. This is the mechanism of chloride attack and a probe has been developed to develop humidity change in concrete.

The successful application of FBG sensors for monitoring the short and long term loading of bridge structures has been conducted with continuous data being recorded for a period of 17 months in one application.

The amount of data acquired during the course of this programme has been enormous and it would be impossible to present all of it here. It is, however, possible to summarise the data. A comparison between the two types of sensor system (ERSG and OFS) was used to assess the performance of the optical fibre based monitoring techniques.

For sensed locations on the field trial structure where there were ERSG and OFS sensors at the same location (a total of 10 sensor points), a comparison between the two types of sensor was possible with the following results:

- 1.2με average difference between ERSG & OFS for 10 sensors over 4 tests.
- 11.9με standard deviation of difference for same sampling batch.

Similarly, a comparison of all of the sensors from two field trial tests conducted 13 months apart is possible after factoring the data to account for differences in the load levels, which shows:

- 7.2με average change for 28 OFS sensors over the 2 tests conducted 13 months apart.
- 18.8με standard deviation of the change for same sampling batch.
- -4.3με average change for 8 ERSG sensors over the 2 tests conducted 13 months apart.
- 7.6με standard deviation of the change for same sampling batch.

The use of optical fibre based technologies within civil engineering has been proven to be of use for further investigations. Sensors are currently being developed to measure the ingress of moisture and chlorides into concrete structures that can ultimately lead to an increased understanding of the behaviour of the materials involved and their resistance to chemical attack. Sensors are also being used to determine the effectiveness of repairs for concrete structures and members.

Acknowledgements

The funding for this activity has been through several European and national research programmes from the European Commission and EPSRC funding bodies. The research has been conducted in collaboration with the following institutions:

- City University - Electrical, Electronic and Information Engineering, EM Technology (UK).
- Cranfield University (UK), University of Kent (UK), Norwegian Public Roads Authority.
- Oceanographic Company of Norway (OCEANOR), ACREO AB (SE) and ETANE S.A. (GR).

References

Betz D, Staudigel L, Trutzel MN , Schmuecker M, Huelsmann E, Czernay U (2002). Test of a fibre Bragg grating sensor network for commercial aircraft structures. *Conference Proceedings Optical Fibre Sensors (OFS 15),* Portland USA, 55-58.

BR106 (1988). Building research establishment report. Design of normal concrete mixes. Revised Ed.

BS EN 197-1 (2000). Cement composition, specifications and conformity criteria for common cements.

Ferdinand P, Ferragu O, Lechien JL, Lescop B, Marty V, Rougeault VS, Pierre G, Renouf C, Jarret B, Kotrotsios G, Neuman V, Depeursings Y, Michel JB, Uffelen MV, Verbandt Y, Voet MRH, Toscano D (1994). Mine operating accurate stability control with optical fibre sensing and Bragg grating technology. *The Brite Euram Stabilis Project Proceedings, SPIE 2360,* 162-166.

Giaccari P, Limberger HG, Kronenberg P (2001). Influence of humidity and temperature on polyimide-coated fiber Bragg gratings. *Proceedings Tends in Optics and Photonics Series: Bragg gratings, photosensitivity, and poling in glass waveguides,* 61, BFB2.

Grattan KTV, Meggitt BT (2000). Optical Fibre Sensor Technology Fundamentals. Kluwer Academic Publishers, Dordrecht, Netherlands.

Grattan KTV, Meggitt BT (2000). Optical Fibre Sensor Technology *Advanced Applications-Bragg Gratings and Distributed Sensors.* Kluwer Academic Publishers, Dordrecht, Netherlands.

Laylor M, Calvert S, Taylor T, Schulz W, Lumsden R, Udd E (2002). Fiber optic grating moisture and humidity sensors. *Proceedings Smart Structures and Materials: Smart Sensor Technology and Measurement System,* 4694, 210-217.

Maurin L, Boussoir J, Rougeault S, Bugaud M, Ferdinand P (2002). FBG-based smart composite bogies for railway applications. *Conference proceedings optical fibre sensors (OFS 15),* Portland USA, 91-94.

Measures RM, Alavie AT, Maaskant R, Ohn M, Karr S, Huang S (1995). A structurally integrated Bragg grating laser sensing system for carbon fibre prestressed concrete highway bridge. *Smart Materials and Structure,* 4, 20-30.

Ning YN, Meldrum A, Shi WJ, Meggitt BT, Palmer AW, Grattan KTV, Li L (1998). Bragg grating sensing instrument using a tunable Fabry-Perot filter to detect wavelength variations. *Measurement Science Technology*, 9, 599-606.

Pal S, Sun T, Grattan KTV, Wade SA, Collins SF, Baxter GW, Dussardier B, Monnom G (2004). Strain-independent temperature measurement using a type-I and type-IIA optical fiber Bragg grating combination. *Review of Scientific Instruments,* 75, 1327-1331.

Yeo TL, Sun T, Grattan KTV, Parry D, Lade R, Powell BD (2005). Polymer-coated fiber Bragg grating for relative humidity sensing. *IEEE Sensors Journal*, 5, 1082-1089.

Challenge Journal of Structural Mechanics

Shear strain related non-linear stochastic dynamic analysis of rock-fill dams

Kemal Hacıefendioğlu [a], Mehmet Akköse [b,*], Alemdar Bayraktar [b], Ali Aydın Dumanoğlu [c]

[a] *Department of Civil Engineering, Ondokuz Mayıs University, 55139 Samsun, Turkey*
[b] *Department of Civil Engineering, Karadeniz Technical University, 61080 Trabzon, Turkey*
[c] *Department of Civil Engineering, Canik Başarı University, 55080 Samsun, Turkey*

ABSTRACT

The effect of the non-linear material behavior of a rock-fill dam subjected to random loads is investigated by the equivalent linear method that considers the non-linear variation of soil shear moduli and damping ratios as a function of shear strain. The Keban dam constructed in Elazığ, Turkey is chosen as a numerical example. The interaction of the rock-fill dam with the reservoir is neglected, but not the foundation rock. The properties of the dam materials were taken from the dam project and assumed to be isotropic in the analysis. A stationary and ergodicity assumption are made for stochastic dynamic analysis. The E-W component of the Erzincan earthquake recorded on March 13, 1992, Erzincan, Turkey is chosen as a ground motion since it occurred nearby the dam site. The component considered is applied to the dam in the horizontal direction. The non-linear stochastic responses of the Keban dam are compared to its linear stochastic and deterministic response.

ARTICLE INFO

Article history:
Received 12 May 2015
Accepted 7 June 2015

Keywords:
Rock-fill dam
Stochastic response
Non-linear analysis
Equivalent linear method

1. Introduction

Rock-fill dams are constructed for various purposes such as irrigation, energy production, flood control and recreation. A serious damage on these dams has been not recorded in the literature due to an earthquake ground motion. Accordingly, it can be said that rock-fill dams are highly resistant to seismic loads. The satisfactory seismic behaviour of these dams is due to the capacity of the rock-fill body.

Gazetas and Dakoulas (1992) have presented comprehensive reviews on theoretical methods for estimating the dynamic response and the performance of earth and rock-fill dams subjected to strong earthquake ground motions. Several factors such as liquefaction effects, non-linear material behaviour, and permanent deformations affect the dynamic response of earth and rock-fill dams during the earthquakes. Linear and non-linear earthquake responses of earth and rock-fill dams including these factors were carried out by many researchers (Seed, 1979; Sayed and Abdel-Ghaffar, 1992; Khoei et al., 2004).

The highly non-linear and hysteretic material behaviour may considerably affect the seismic response of rock-fill dams. Traditionally, an equivalent linear method is used to determine the non-linear response of rock-fill dams to earthquakes. Seed and Idriss (1969) used the equivalent linear method to incorporate the observed strain-dependent non-linear behaviour of soils. Vrymoed (1981) studied the dynamic analysis of a dam by using the equivalent linear method. Mejia et al. (1982) used the same method for the three-dimensional dynamic analysis of earth dams. These studies were performed by using the deterministic methods.

Because of the randomness of earthquake ground motions, the researchers have started to use the random vibration theory for estimating the dynamic response of embankment dams. Singh and Khatua (1978) reported probabilistic techniques in assessing the seismic stability of earth dams. Gazetas et al. (1982) developed a new random vibration procedure to estimate the statistics of the non-linear hysteretic response of earth dams modelled as inhomogeneous shear slices and excited by strong motions consisting of vertical shear waves.

* *Corresponding author*. Tel.: +90-462-3772628 ; Fax: +90-462-3772606 ; E-mail address: akkose@ktu.edu.tr (M. Akköse)
ISSN: 2149-8024 / DOI: http://dx.doi.org/10.20528/cjsmec.2015.06.013

In recent years, the stochastic seismic responses of earth dams have also been investigated by only a limited number of researchers (Mellah et al., 2000; Chen and Harichandran, 2001; Hacıefendioğlu, 2006). However, it can be seen from the literature review that a few works on stochastic response of rock-fill dams to earthquake ground motion have been studied. Therefore, the objective of this study is to determine the non-linear seismic response of the Keban dam, which is a rock-fill dam, to random ground motions using the finite element method.

2. Simple Method for Non-linear Response

In this study, equivalent linear method is used in an iterative way for stochastic analysis in which non-linear material behavior is considered. Strain properties of the materials in each finite element are defined by a shear modulus and an equivalent damping ratio which depends on the shear strain. By considering low-strain (10^{-4}%), initial values of the shear modulus and the damping ratio are taken into consideration for each element. With given values of the shear modulus and the damping ratio, a linear elastic analysis is performed to determine the stochastic dynamic response. An effective strain, which is usually considered as the maximum value for the stochastic analysis, is computed in each finite element. It is noted that, in establishing the effective strain, it is not necessary to resort to arbitrary scaling of the computed strain values as in the deterministic methods where a strain reduction factor on the computed value of strain is applied. That is, the effective strain is used as the mean value of the random process describing the maximum value of the strain. Then the moduli and the damping ratios are selected for the computed effective strain and used for the next iteration (Gazetas et al., 1982). This procedure is repeated until the differences of the moduli and the damping ratios between two iterations are very small. The response value obtained at the last iteration is considered as the true nonlinear response.

The maximum dynamic shear modulus of cohesionless materials, G_{max}, is computed by using the following expression (Seed and Idriss, 1970)

$$G_{max} = 1000(K_2)_{max}(\sigma_m)^{1/2}\,, \tag{1}$$

where σ_m is mean stress. Values of $(K_2)_{max}$ determined by laboratory tests have been found to vary from 150 to about 250 for compacted gravels and rock-fill. Experimental data from the literature on the shear strain dependent moduli and damping for rock-fill materials are depicted in Fig. 1(a) (Seed et al., 1986). The shear modulus values for saturated cohesive soils have been found to vary with the undrained shear strength level as

$$G = 2000 s_u\,, \tag{2}$$

where $s_u = c + \sigma_m \tan\phi$ is the undrained shear strength, c is the cohesion factor and ϕ is the angle of internal friction. The variations of the shear modulus and the damping ratios with shear strain for clay material is presented in Fig. 1(b) (Sun et al., 1988; Idriss, 1990). Finally, the variations of the shear modulus and the damping ratios with shear strain for rock material is shown in Fig. 1(c) (Schnabel et al., 1972).

3. Formulation of Stochastic Analysis

An acceleration-time history of ground motion recorded at one point is used as seismic input in the deterministic method. In the stochastic method, however, recorded ground motions appropriate to the site are characterized by statistically. Since the ground motion caused by seismic disturbance is random, the best way to characterize the random excitation statistically is to employ a power density function and autocorrelation function. So, the stochastic parameters describing the seismic output can be determined from the power spectral density function of the seismic input.

In this study, a stationary assumption where the statistical parameters are independent of time is made for stochastic analysis. Besides, the ergodicity assumption is made to use only one earthquake record.

If a single ground acceleration record is used for the input, the cross power spectral density function, $S_{ij}(\omega)$, can be determined by using the equation of motion of the system by the following equation (Dumanoğlu and Severn, 1990).

$$S_{ij}(\omega) = S_{in}(\omega)\sum_{r=1}^{N}\sum_{s=1}^{N}\psi_{ir}\psi_{js}\,H_{ir}(\omega)H_{js}^{*}(\omega)\,, \tag{3}$$

where ω is the frequency; $H(\omega)$ is the frequency response function; $S_{in}(\omega)$ is the power spectral density function of the ground motion; $N$is the number of modes which are considered to contribute to the response; ψ_{ir} is the contribution of the rth mode to $U_j(t)$ displacement and * denotes the complex conjugate. The expected maximum value (μ) is the mean value of all maximum values and can be expressed as

$$\mu = p\sqrt{\lambda_0}\,, \tag{4}$$

where p is the peak factor and λ_0 is the initial spectral moment (Der Kiureghian, 1980).

4. Numerical Example

In this study, the Keban dam constructed in Elazığ, Turkey is chosen as a numerical example to investigate the non-linear stochastic response of rock-fill dams by the finite element method. The finite element mesh of the dam is shown in Fig. 2.

The Keban dam is 163 m high from riverbed. The crest has a length of 1097 m. The main purpose of the dam is to regulate river flow and supply energy. In the finite element mesh of the dam, there are 326 nodes and 286 quadrilateral elements. The dam is treated as a plane strain problem. The interaction of the rock-fill dams with the reservoir has generally neglected (Priscu et al., 1985). Therefore, the interaction with the reservoir is accordingly ignored, but not the foundation rock.

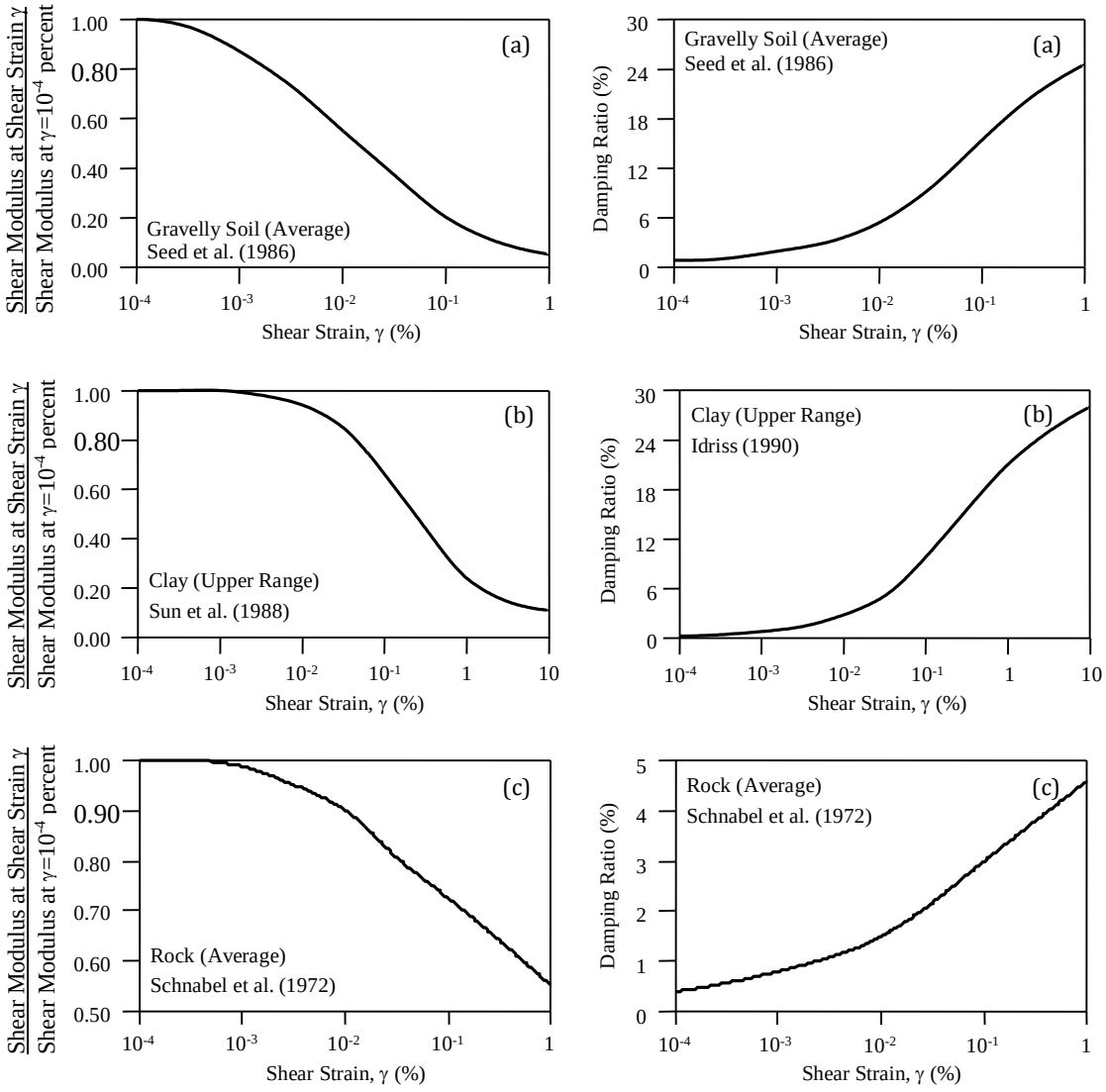

Fig. 1. The variation of shear modulus and damping ratios for (a) gravelly soil, (b) clay material and (c) rock material, respectively.

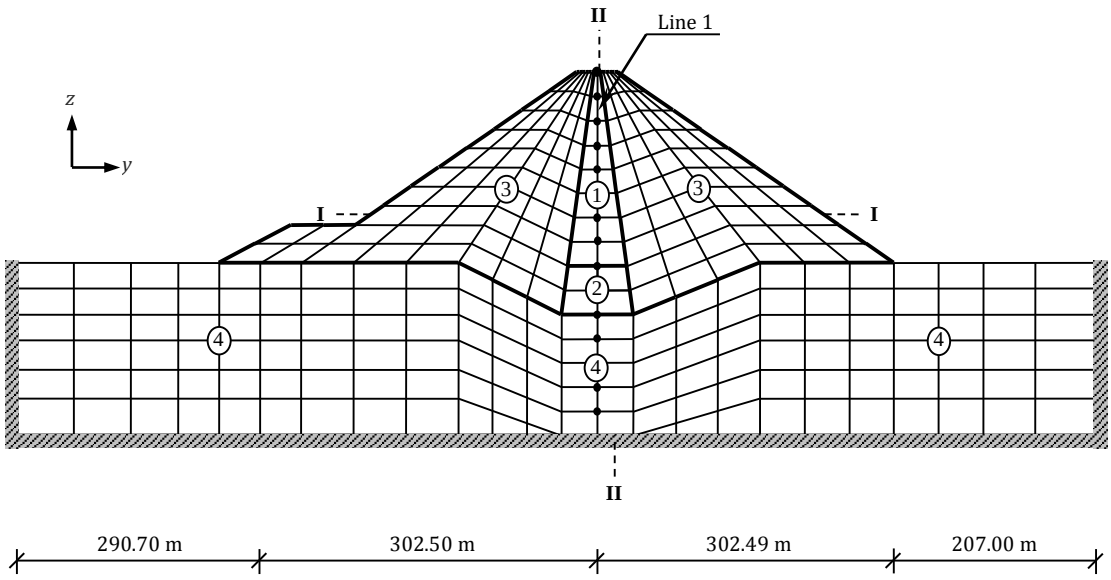

Fig. 2. Finite element mesh of the Keban dam.

Materials in the dam section can be grouped in three main categories: the impervious clay core (material number 1) flanked by transition filters, a concrete core (material number 2) at the bottom of the dam and the compacted rock-fill (material number 3) placed at various lifts. The properties of these materials taken from the dam project are as follows: For the impervious clay core, mass density ρ=2089.70 kg/m^3, and Poisson's ratio ν=0.45; for the concrete core, mass density ρ=2446.48 kg/m^3, and Poisson's ratio ν=0.15. The elasticity modulus, mass density and Poisson's ratio of the foundation rock are taken as 1.379×10^{10} N/m^2, 2689.09 kg/m^3, and 0.24, respectively. The cohesion constant is 15 kN/m^2 and the angle of friction is equal to 20^o for the saturated clay core. $(K_2)_{max}$ factor is given as 170 at small-strains for the dynamic modulus coefficient of the gravel material. Maximum shear modulus for the central core is calculated depending on the G/s_u ratio. To evaluate the small-strain shear modulus of the core material, the average ratio G_{max}/s_u is taken as 2000. The initial damping value is selected as 5% for the non-linear stochastic response analysis of the rock-fill dam.

The E-W component of the Erzincan earthquake recorded on March 13, 1992, Erzincan, Turkey is chosen as ground motion since it occurred nearby the dam site. The component is applied to the dam in the upstream-downstream direction. The power spectral density (PSD) function of the Erzincan earthquake is determined with the Fourier transforms of the autocorrelation function. Fig. 3 shows the E-W component of the Erzincan Earthquake and its power spectral density function. The calculated intensity parameter value is S_0=0.00593 m^2/s^3. Filter parameter values proposed by Der Kiureghian and Neuenhofer (1991) are utilized as ω_g=10.0 rad/s, ξ_g=0.4, ω_f=1.0 rad/s, and ξ_f=0.4.

In this paper, the dynamic response of the Keban dam subjected to the Erzincan earthquake is also obtained by the deterministic method. The linear and non-linear results obtained from the stochastic analysis and the linear results obtained from the deterministic analysis are compared to each other. The dynamic responses of the Keban dam are calculated for a time interval of 0.00225 sec.

In clay core, the initial shear moduli and shear moduli obtained from the non-linear analysis are shown in Fig. 4. As shown in Fig. 4, the shear moduli obtained from the non-linear analysis are smaller than the initial shear modulus. Fig. 4 shows also the variation of shear strain with the height of the dam. It is seen from Fig. 4 that the shear strain values obtained from the non-linear analysis inrease with the height of the dam as well as the initial shear strain used for the linear analysis (value (%)=10^{-4}).

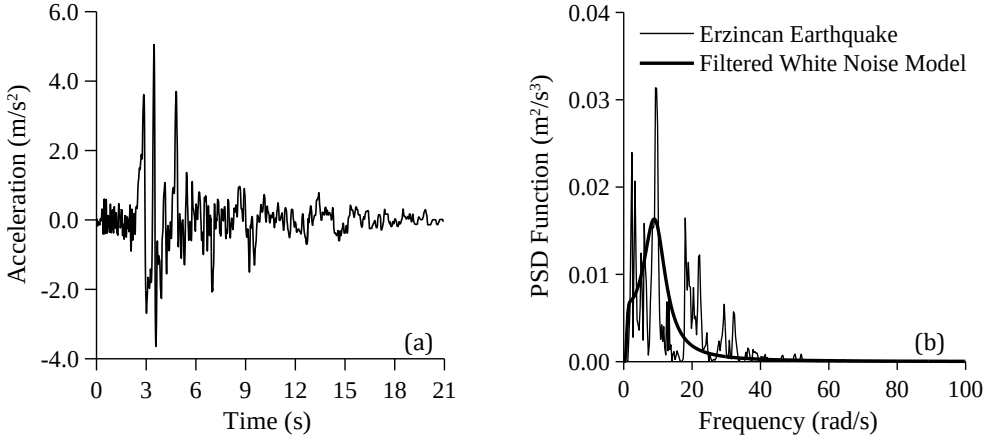

Fig. 3. a) The E-W component of the Erzincan earthquake recorded on March 13, 1992, Erzincan, Turkey and b) its power spectral density (PSD) function.

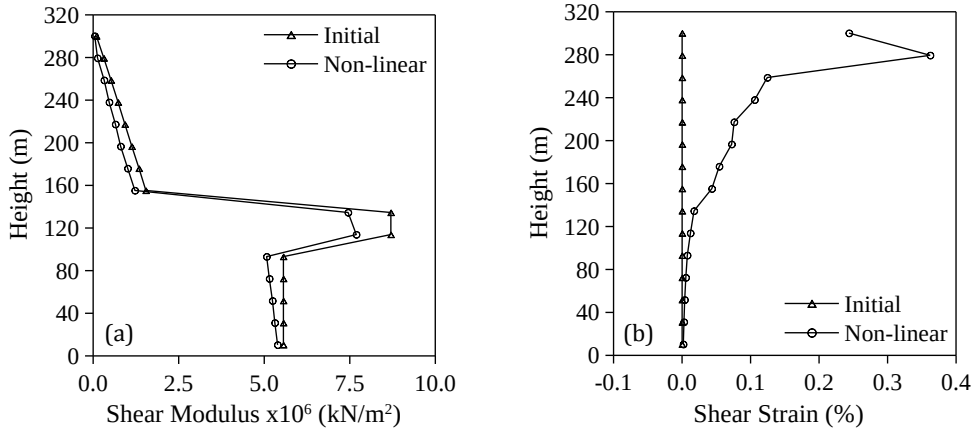

Fig. 4. a) Initial shear moduli versus shear moduli and b) initial shear strains versus shear strains obtained from the non-linear analysis.

4.1. Displacements

Mean of maximum values of displacements are calculated from the stochastic dynamic analyses while the absolute maximum values of displacements are obtained from deterministic dynamic analysis. Horizontal displacements at the marked nodes on line 1 (nodes along the core of the dam in Fig. 2) obtained from the deterministic analysis (for linear material behavior) and the stochastic analyses (for linear and non-linear material behaviors) of the Keban dam are plotted in Fig. 5. It is seen from Fig. 5 that the expected maximum values of horizontal displacements obtained from the stochastic analyses are smaller than the absolute maximum horizontal displacements obtained from the deterministic analysis. In addition, the non-linear displacements are smaller than linear displacements for stochastic analysis.

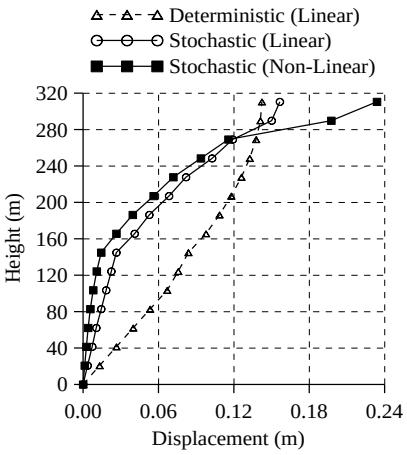

Fig. 5. Horizontal displacements at the marked nodes on line 1.

4.2. Stresses

The stress components, which are obtained from the stochastic and deterministic dynamic analyses, are also compared with each other. The stress values are calculated at the middle points of the elements. Horizontal, vertical and shear stress components on sections I-I are compared in Figs. 6-8 while those on section II-II are compared in Fig. 9. It can be seen from Figs. 6-9 that the expected maximum values of all stress components for stochastic analyses (for linear and non-linear material behaviors) are smaller than the absolute maximum stresses for the deterministic analysis (for linear material behavior).

5. Conclusions

Non-linear material behavior of the Keban dam, which is a rock-fill dam, subjected to random loads is investigated by the equivalent linear method which considers the non-linear variation of soil shear moduli and damping ratios as a function of shear strain.

It is observed that for the non-linear displacement and stress responses obtained from the stochastic analysis are smaller than the linear responses obtained from the stochastic and deterministic analyses. In addition, all displacement and stress results obtained from deterministic analysis are greater than the mean of maximum values obtained from stochastic analyses.

Because the mean of maximum values obtained from stochastic analyses is calculated by averaging all the maximum response values, it should be expected that the absolute maximum values obtained from deterministic analysis would be greater than the mean of maximum values.

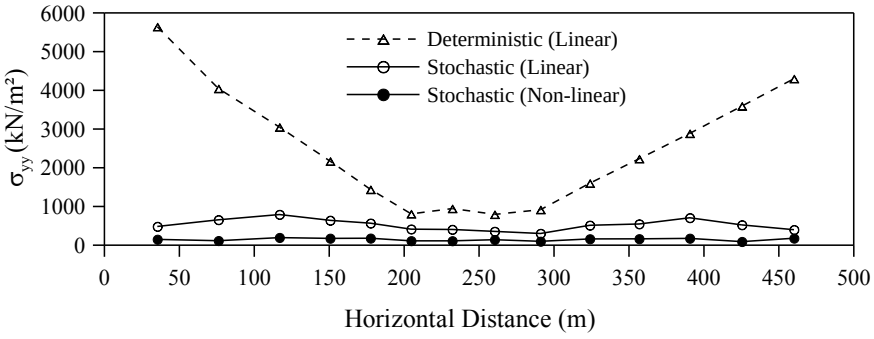

Fig. 6. Horizontal stresses (σ_{yy}) on section I-I of the Keban dam.

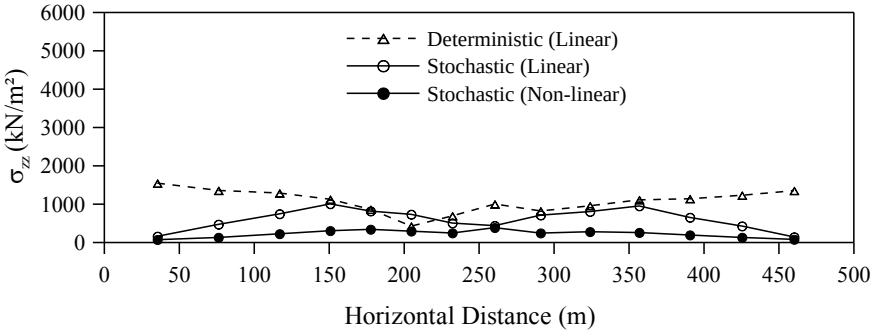

Fig. 7. Vertical stresses (σ_{zz}) on section I-I of the Keban dam.

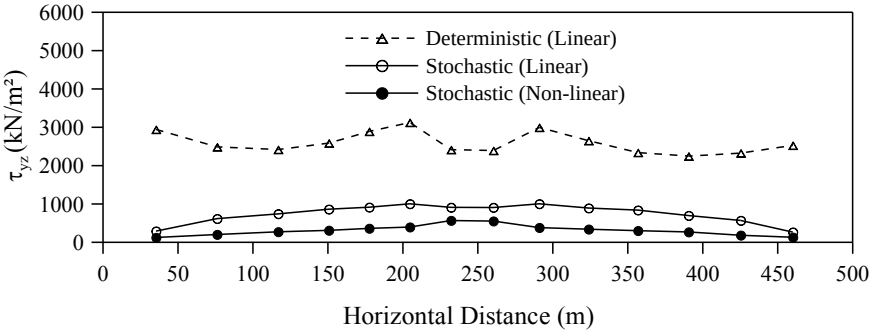

Fig. 8. Shear stresses (τ_{yz}) on section I-I of the Keban dam.

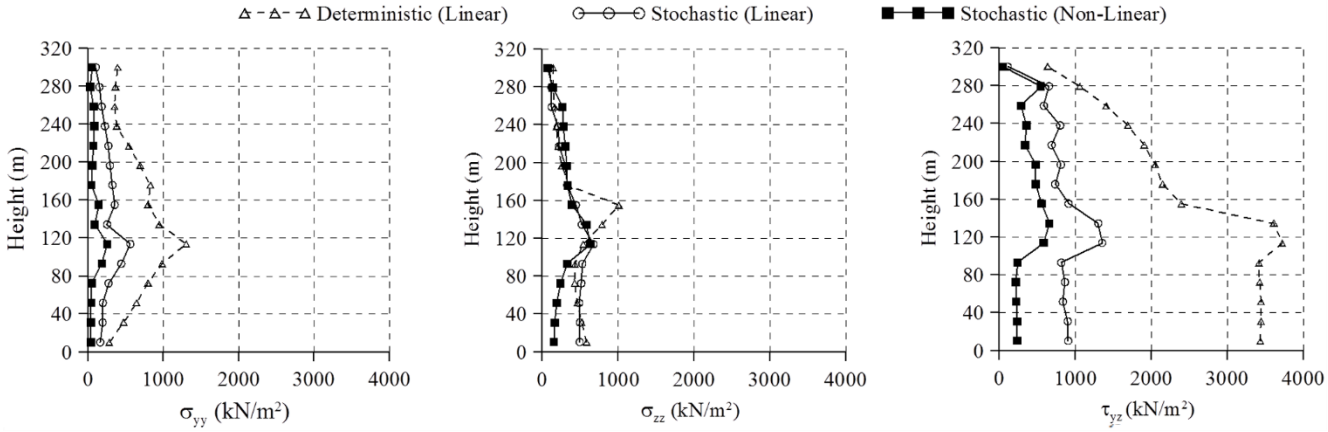

Fig. 9. Horizontal (σ_{yy}), vertical (σ_{zz}) and shear stresses (τ_{yz}) on section II-II of the Keban dam.

REFERENCES

Chen MT, Harichandran RS (2001). Response of an earth dam to spatially varying earthquake ground motion. *Journal of Engineering Mechanics*, 127(9), 932-939.

Der Kiureghian A (1980). Probabilistic modal combination for earthquake loading. *Proceeding of 7th World Conference on Earthquake Engineering*, Istanbul, 729–736.

Der Kiureghian A, Neuenhofer A (1991). A response spectrum method for multiple-support seismic excitations. Report No. UCB/EERC-91/08. *Earthquake Engineering Research Center*, College of Engineering, University of California, Berkeley, CA.

Dumanoğlu AA, Severn RT (1990). Stochastic response of suspension bridges to earthquake forces. *Earthquake Engineering and Structural Dynamics*, 19, 133–152.

Gazetas G, Dakoulas P (1992). Seismic analysis and design of rockfill dams: state-of-the-art. *Soil Dynamics and Earthquake Engineering*, 11, 27-61.

Gazetas G, DepChaudhury A, Gasparini D (1982) Stochastic estimation of the nonlinear response of earth dams to strong earthquakes. *International Journal of Soil Dynamics and Earthquake Engineering*, 1(1), 39-46.

Hacıefendioğlu K (2006). Transient stochastic analysis of nonlinear response of earth and rock-fill dams to spatially varying ground motion. *Structural Engineering and Mechanics*, 22(6), 647-664.

Idriss IM (1990). Response of soft soil sites during earthquakes. *Proceedings Memorial Symposium to Honor Professor Harry Bolton Seed*, Berkeley, California, Vol. II.

Khoei AR, Azami AR, Haeri SM (2004). Implementation of plasticity based models in dynamic analysis of earth and rockfill dams: A comparison of Poster-Zienkiewicz and cap models. *Computers and Geotechnics*, 31, 385-410.

Mejia LH, Seed HB, Lysmer J (1982). Dynamic analysis of earth dams in three dimensions. *ASCE Journal of the Geotechnical Engineering Division*, 108(GT12), 1586-1604.

Mellah R, Auvinet G, Masrouri F (2000). Stochastic finite element method applied to non-linear analysis of embankments. *Probabilistic Engineering Mechanics*, 15, 251-259.

Priscu R, Popovici A, Stematiu D, Stere C (1985). Earthquake Engineering for Large Dams, 2nd edition, Editura Academiei, Bucharest.

Sayed HS, Abdel-Ghaffar AM (1992). System identification of nonlinear seismic response of earth dams. *Tenth World Conference on Earthquake Engineering*, Rotterdam, 4733-4739.

Schnabel PB, Lysmer J, Seed HB (1972). SHAKE: A computer program for earthquake response analysis of horizontally layered sites, Report UCB/EERC-72/12, *Earthquake Engineering Research Center*, University of California, Berkeley.

Seed HB (1979). Considerations in the earthquake design of earth and rockfill dams. *Geotechnique*, 29(3), 215-263.

Seed HB, Idriss IM (1969). Influence of soil conditions on ground motion during earthquakes. *ASCE Journal of Soil Mechanics and Foundations Division*, 95(SM1), 99-137.

Seed HB, Idriss IM (1970). Soil moduli and damping factors for dynamic response analysis. Report No. EERC/70-10, *Earthquake Engineering Research Center*, University of California, Berkeley.

Seed HB, Wong RT, Idriss IM, Tokimatsu K (1986). Moduli and damping factors for dynamic analyses of cohesionless soils. *Journal of Geotechnical Engineering*, 112(11), 1016-1032.

Singh MP, Khatua TP (1978). Stochastic seismic stability prediction of earth dams. *Earthquake Engineering and Soil Dynamics-Proceedings of theASCE Geotechnical Engineering Division Speciality Conference*, Pasedena, California, 875-889.

Sun JI, Golesorkhi R, Seed HB (1988). Dynamic moduli and damping ratios for cohesive soils. Report No. UCB/EERC-88/15. *Earthquake Engineering Research Center*, University of California, Berkeley.

Vrymoed J (1981). Dynamic FEM model of Oroville Dam. *ASCE Journal of Geotechnical Engineering Division*, 107(GT8), 1057-1077.

Challenge Journal of Structural Mechanics

A method for determination of the dimensions of seismic shear walls in buildings

Turgut Öztürk *, Zübeyde Öztürk, Onur Öztürk

Department of Civil Engineering, İstanbul Technical University, 34469 İstanbul, Turkey

ABSTRACT

A lateral load carrying system consisting of only shear walls is used generally for structures having 14 storeys or more. It can be seen that the effect of earthquakes in the systems consisting of the shear walls or shear walls-core are very small. For resisting earthquake effects it is proposed to construct shear walls which are perpendicular to each other in plan and having the cross sectional area 1.5% of the building. Unfortunately in this proposal, the effect of number of storeys and the division of shear wall area to the necessary parts is not taken into consideration. In this paper, these factors are considered as, number of storeys, plan area of a storey, earthquake risk zone, material properties and shear wall thickness. The criteria for determination of the dimensions of earthquake shear walls which are suitable for architectural considerations of the building are given. For various storey areas and 10 storeys, the lengths of shear walls which ensure the suggested criteria, having the same length are given in diagrams. It is also shown how to find the length of shear walls under the same conditions if there are more than 10 storeys.

ARTICLE INFO

Article history:
Received 28 January 15
Accepted 20 March 15

Keywords:
Earthquake
Seismic analysis
Seismic zone
Shear wall
Building codes

1. Introduction

In our country, it is preferred to build structures both under horizontal and vertical loadings by the use of frame systems, till 6 storeys in the first earthquake risk zone and 7 storeys in the second earthquake risk zone. In frame systems, because of the reasons of more storeys, greater cross-section areas for beams and columns especially at the lower storeys or large relative displacements between the storeys lead to build the frame structure with shear walls. The obligation of using lifts in buildings having 6 storeys or more leads a lift-house in the means of core. A lateral load carrying system consisting of only shear walls is used generally for structures having 14 storeys or more (ATC22, 1989; Tarenath, 1988; Wakabayashi, 1988; Paulay and Priestley, 1992; Özden and Kumbasar, 1993; Celep and Kumbasar, 2004). However, in these systems, for limiting the thickness of the slabs, some of the vertical loads can be transferred to foundations by the use of columns which do not carry horizontal loads if needed. From the observations made in the earthquake regions after an earthquake event, large damages can be seen in frame system structures having 4-8 storeys, frame-shear wall (+core) system structures having 7-13 storeys (Fintel, 1991).

The main reasons of the earthquake damages are not applying the codes in the design and construction of the structures such as; a) not obeying the constructive rules for reinforcement lay-out in beam-column or beam-shear wall joints (such as development length, stirrups, etc.), and less shear capacity than bending capacity in these zones, b) the occurrence of plastic hinges on columns before beams, c) neglecting of the torsional effects in calculations, d) unassured ductile system, e) structural irregularities, f) less concrete strength usage than design strength, g) not taking into account of foundation soil properties while calculating the earthquake forces, h) unsuitable foundation system.

It can be seen that the effects of earthquakes in the systems consisting of the shear walls or shear walls-core are very small. This is confirmed in a detailed manner by Fintel (1991) and although the behaviour of systems

* *Corresponding author*. Tel.: +90-212-2853842 ; Fax: +90-212-2853842 ; E-mail address: ozturkturg@itu.edu.tr (T. Öztürk)
ISSN: 2149-8024 / DOI: http://dx.doi.org/10.20528/cjsmec.2015.03.006

consisting of shear walls having diagonal cracks after an earthquake have some points which are necessary to investigate, these systems are the best solutions for earthquake resistance (Altın, 1989; Fintel, 1991). This property of shear walls is also seen by Ersoy (1993) and proposed to construct shear walls which are perpendicular to each other in plan and having the cross sectional area 1.5% with respect to building area for earthquake effects (Ersoy, 1993). Unfortunately, in this proposal, the effect of number of storeys and the division of shear wall area to the necessary parts is not taken into consideration.

In this paper, these factors are considered as; a) number of storeys, b) plan area of a storey, c) earthquake risk zone, d) material properties, e) selected shear wall thickness, f) the criteria for determination of the dimensions of earthquake shear walls. Constructed buildings having different storey areas and storey weights are considered and by the use of TS498 (2000) and TNC (2000), the average weight for percent area is determined for single storey. Then, the total shear force, the overturning moment, the minimum and maximum values of axial forces of the shear walls at the basement and the top force V_t are calculated for the buildings having number of storeys from 2 to 10 and A_p storey areas from 100 m^2 to 800 m^2. The criteria for determination of the dimensions of earthquake shear walls which are suitable for architectural configurations of the building are given. For storey areas A_p, from 800 m^2 to 100 m^2 and number of storeys n=10, the lengths of shear walls are given which ensure the criteria, having the number of shear walls n_b=3-10 with the same length in part 4. It is also shown how to find the length of shear walls under the same conditions if there are more than 10 storeys. Numerical examples are given and the results are listed in conclusion part.

2. Average Vertical and Horizontal Loads

Observations made on the constructed buildings having various storey heights, storey areas and usage (such as houses, offices) show that the average uniform vertical load of a storey can be accepted as m=12 kN/m^2. In the present paper, the behaviour of the slabs of structures made of shear walls is taken as flat-slabs with the thickness of 200 mm. The total weight of the building over the foundation can be evaluated as

$$W = NmA_p \,, \tag{1}$$

where N is the number of storeys and A_p is the storey area. The total vertical force summation of the shear walls W_p above the foundations is about 50, 75 and 100% of the total building weight W. Different values of percentage is taken into account for shear wall system and for shear wall-frame system, separately, like;

$$W_p = 0.75W = 0.90NA_p \;,\; W_p = 1.00W = 1.20NA_p \,, \tag{2}$$

$$W_p = 0.50W = 0.60NA_p \;,\; W_p = 0.75W = 0.90NA_p \,. \tag{3}$$

The calculation of the horizontal loads is made according to TNC, 2007. Total shear force just above the foundation V_t can be written together with Eq. (2).

$$V_t = WA(T_1)/R_a(T_1) \geq 0.10A_0IW \,,$$
$$A(T_1) = A_0IS(T) \;,\; T_1 \cong T_{1A} = C_tH_N^{3/4} \,. \tag{4}$$

In this calculations, A_0 effective ground acceleration coefficient, importance factor I=1.00, C_t=0.03∼0.04 (shear wall system), C_t =0.05 (shear wall-frame system), T_{1A}= 0.09 $H_N/\sqrt{L}$ (for H_N>25 m, L is the building length in seismic direction) are taken into account. Seismic load reduction factor $R_a(T_1)$ and structural behaviour factor R are taken as 6.00 for shear wall system and as 7 for shear wall-frame system.

Accepting a triangularly variation for V_t along the height of the building H_N; w_n can be written as w_n=2V_t/H=2V_t/(Nh) at the top. Here, h is the storey height. In this study, storey height is assumed as 3.00 m.

The overturning moment M_T and the shear force V_t at the base of the building are

$$M_T = (2/3)H_NV_t \,. \tag{5}$$

3. The Criteria for Shear Wall Determination

The suggested criteria for determination of the dimensions of earthquake shear walls are listed in the following (TS500, 2000; TNC, 2007):

1) The compression depth of the shear walls at the base with high ductility should be

$$k_x = \frac{x}{d} = \varepsilon_{cu}/(\varepsilon_{cu} + \varepsilon_s) \leq 0.423 \,. \tag{6}$$

Under this condition ε_s is

$$\varepsilon_s \geq 0.0041 \,, \tag{7}$$

which is 2.05 multiple of ε_{ys} for f_{yk} =420 N/mm^2 (NBC, 1985; TS500, 2000; Celep and Kumbasar, 2005). The structure behaviour coefficient should be estimated according to the situation if the ductility is not increased.

2) The ratio of the total area of vertical reinforcement at each wall end zone to the gross wall cross section area should not be less than 0.001. However this ratio shall be increased to 0.002 along the critical wall height. The reason for this criteria is to assure a suitable concreting and is existing of the fifth criteria.

$$\rho \leq 0.002 \text{ (along the critical wall height).} \tag{8}$$

3) The relative storey displacement Δ_i is

$$\Delta_i = d_i - d_{i-1} \leq 0.003h_i \,, \tag{9}$$

where d_i is the displacement of i-th floor and h_i is the storey height. According to this, the ratio of shear wall top horizontal displacement f to the building height H is θ which is

$$\delta_i = R\Delta_i \ , \ \delta_{i(max)}/h_i \leq 0.02 \, . \tag{10}$$

This criteria supplies the second order effects to be negligible.

4) It is necessary to ensure a sufficient shear force capacity of the shear walls so that there should not be any diagonal cracks in shear walls at the ultimate state. This criteria assures, if the smaller principal concrete stress is negative on the center of gravity of the shear wall above the basement, then the absolute value of this should be smaller than a proper value (TS9967, 1992). With the axial stress σ_c caused by vertical loads and the shear stress τ_c caused by shear forces in the center of gravity of the shear wall, the small principal stress σ_1 is known to be

$$\sigma_1 = \left(\frac{\sigma_c}{2}\right) - \sqrt{(\sigma_c/2)^2 + \tau_c^2} \, . \tag{11}$$

If σ_1 is negative, then the criter can be expressed as $|\sigma_1|<\sigma_1^*$, where $\sigma_1^*=0.043f_{ck}$ and f_{ck} is the characteristic compressive strength of the concrete.

An i-th shear wall's shear force V_{Ti} above the foundation and the axial force N_{Ti} caused by vertical loads with the shear wall width b_i and length l_{Ti} then with the stresses $\sigma_{ci}=N_{Ti}/b_i l_{Ti}$ and $\tau_{ci}=V_{Ti}/b_i l_{Ti}$. Eq. (11), for σ_1 being negative, the absolute value can be written as,

$$|\sigma_1| = \left|\left(\frac{1}{2b_i l_{Ti}}\right)\left(N_{Ti} - \sqrt{N_{Ti}^2 + 4V_{Ti}^2}\right)\right| \leq \sigma_1^* \, . \tag{12}$$

By using these equations, the shear wall lengths which satisfy the criteria can be obtained. For $C=A(T_1)/R_a(T_1)$,

$$l_{Ti} = \frac{\left[2.85NA_p\left(1-\sqrt{1+16C^2}\right)\right]}{b\sigma_1^*} \quad \text{for} \quad N_T = 0.50W \, ,$$

$$l_{Ti} = \frac{\left[4.28NA_p\left(1-\sqrt{1+7.11C^2}\right)\right]}{b\sigma_1^*} \quad \text{for} \quad N_T = 0.75W \, ,$$

$$l_{Ti} = \frac{\left[5.7NA_p\left(1-\sqrt{1+4C^2}\right)\right]}{b\sigma_1^*} \quad \text{for} \quad N_T = 1.00W \, . \tag{13}$$

From Eqs. (13), it is obvious that l_{Ti} inversely proportional to f_{ck} and b and right proportional to N. Eq. (14) can be obtained with the condition A_p and C to be the same for two different values of n, b and f_{ck} which leads a relation with different shear wall lengths l_{Ti}.

$$l_{T2} = l_{T1}\left(\frac{N_2}{N_1}\right)\left[\frac{f_{ck}^{(2)}}{f_{ck}^{(1)}}\right]\left(\frac{b_1}{b_2}\right) \, . \tag{14}$$

Shear wall lengths l_{Ti} are given in diagrams which are calculated from Eq. (13) for n=10 storeys, f_{ck}=20 N/mm^2, b=200 mm and for various values of A_p, A_0 and N_T. For shear wall lengths in the plan l_{bi} which are suitable to the building plan, being larger than l_{Ti},

$$l_{Ti} < l_{bi} \, , \tag{15}$$

the diagonal crack criteria is clearly ensured. If the shear wall has a cross-section like [, L , I ; then this criteria should be controlled. This criteria also takes place in the Romanian Code for Precast Structures 1972 and TS 9967. Horizontal load capacity of shear walls having diagonal-cracks contains some unclear points to be investigated.

5) The shear force capacity should be greater than the bending moment capacity in shear walls. This prevents the diagonal-cracks and can be obtained by the longitudinal reinforcement ratio less than 0.002 at the end cross-sections of the shear walls ($l_{bi}b$). It means that if the second and fourth criteria are ensured then the fifth criteria is also ensured. The shear force V_e shall be taken into account in calculating the transverse reinforcement in walls. Shear strength of wall cross sections V_r shall be calculated with Eq. (16). The shear force V_e shall satisfy the conditions defined below.

$$V_e \leq V_r \ , \ V_e \leq 0.22A_{ch}f_{cd} \, ,$$

$$V_r = A_{ch}(0.65f_{ctd} + \rho_{sh}f_{ywd}) \ , \ V_r \leq A_{wf}f_{yd}\mu \, . \tag{16}$$

6) Structural walls are the vertical elements of the structural system where the ratio of length to thickness in plan is equal to at least seven (l_w/b_w>7). In buildings where seismic loads are fully carried by structural walls along the full height of building, wall thickness shall not be less than 1/15 the highest storey height and 200mm, provided that both of the conditions given by Eq. (17) are satisfied.

$$\sum A_g / \sum A_p \geq 0.002 \ , \ V_t / \sum A_g \leq 0.5 \, f_{ctd} \, . \tag{17}$$

4. Evaluation of Shear Wall Lengths

The number of the shear walls having equal length on each side of the building can be n_b=3-10. Let us express the length of each shear wall by l_{bi} under the condition that A_0, A_p, n, n_b, f_{ck} and b are constant. The moment of inertia for a single shear wall I_{bi} and overturning moment M_{bi} and shear force V_{bi} at the foundation are

$$l_{bi} = b l_{bi}^3/12 \, ,$$

$$M_{bi} = M_T l_{bi} / \sum I_{bi} \ , \ V_{bi} = V_T l_{bi} / \sum I_{bi} \, . \tag{18}$$

The total moment of inertia for all shear walls can be expressed as a single shear wall with the moment of inertia. The elastic horizontal displacement f of the structure top edge can be calculated and its ratio to the structure height θ can be written. After the calculation of overturning moments, shear forces and axial forces of

the shear walls, reinforcement can be calculated by ensuring the first and the second criteria. The non-dimensional axial force n_i and the non- dimensional overturning moment m_i and the l_{bi} lengths can be calculated. For the determination of l_{bi}, it should be used the calculated l_{bi} lengths corresponding to the values of n_i or m_i due to the first and the second criteria. The lengths of shear walls, for n=10 storeys and equal shear wall lengths with the numbers n_b=3-10 are evaluated. Without giving the details of the calculations, for A_p from 100 m² to 800 m², b=0.20 m, A_0=0.10 and 0.40, f_{ck}=20 N/mm² and N_T=(0.50-1.00)W, the l_{bi} lengths are calculated and the values of θ, ρ, ε_c, ε_s and k_x are given in the diagrams. It should be noted that the calculated l_{bi} lengths for a specific number of storeys such as n=10, should be multiplied by

$$\eta = n^*/10\,. \tag{19}$$

As seen in Eqs., and under the same conditions but different number of storeys as n=n^*≠10, the lengths of shear walls will be obtained. On the other hand, the k_x, ρ and θ values obtained for n=n^* and for n=10 under the same conditions are equal to each other.

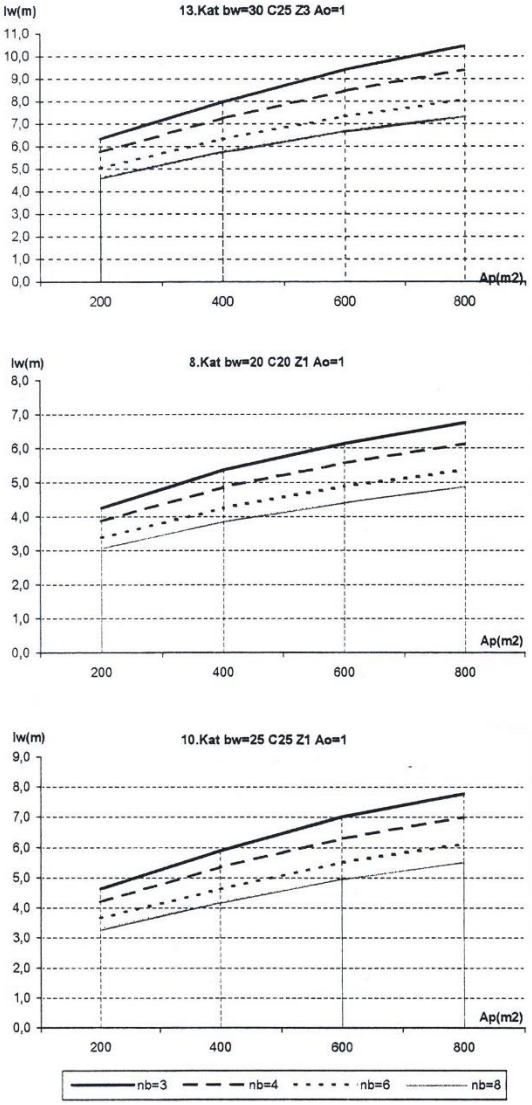

Fig. 1. Shear wall length diagrams.

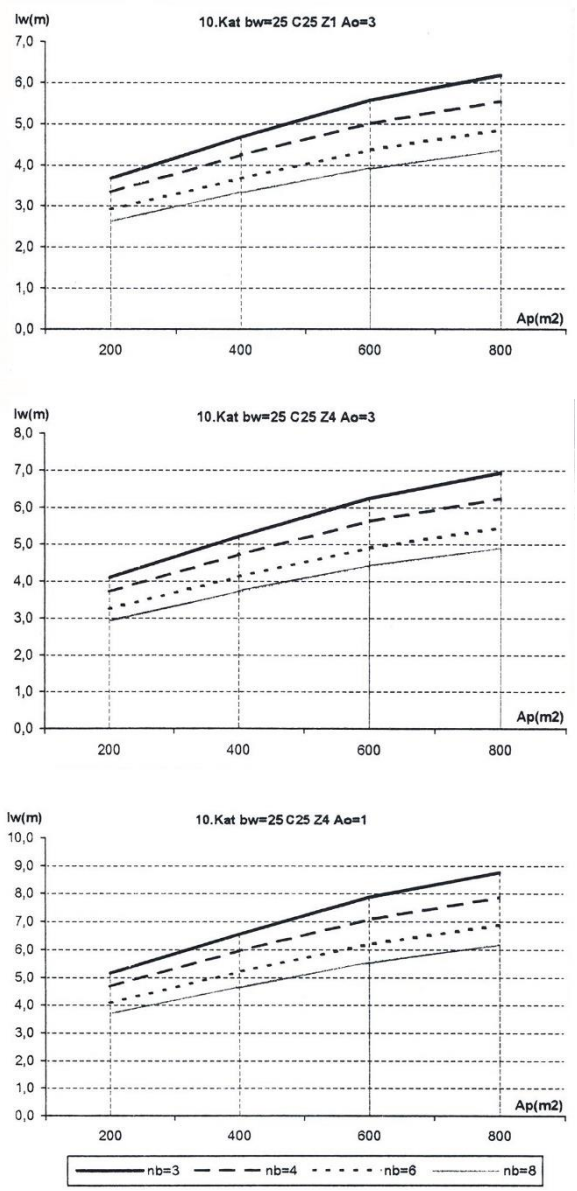

Fig. 2. Shear wall length diagrams.

Examination of the diagrams yields the following:

a) Generally it can be said that, for larger values of A_p while N_T=0.50W, k_x reaches 0.423 and ρ is very low with comparison to 0.001 but for decreasing A_p, instead of upper limit for k_x, the second criteria which makes ρ=0.001 should be taken into consideration. In the situation of decreasing axial force, instead of k_x, it can be seen that ρ can reach more easily to the upper limit.

b) When the axial force is large while there is small storey area, the l_{bi} length of one of the shear walls having the same length can be greater than the length $n_b l_{Ti}$.

c) Shear walls calculated according to the first and the second criteria, always ensure the fourth criteria.

d) Value for θ is also given. As it is seen, when the l_{bi} lengths are calculated according to the first and the second criteria, the third criteria is also ensured.

On the other hand, as the lengths of the shear walls are defined in the architectural plan, the shear walls in the same direction can have different lengths.

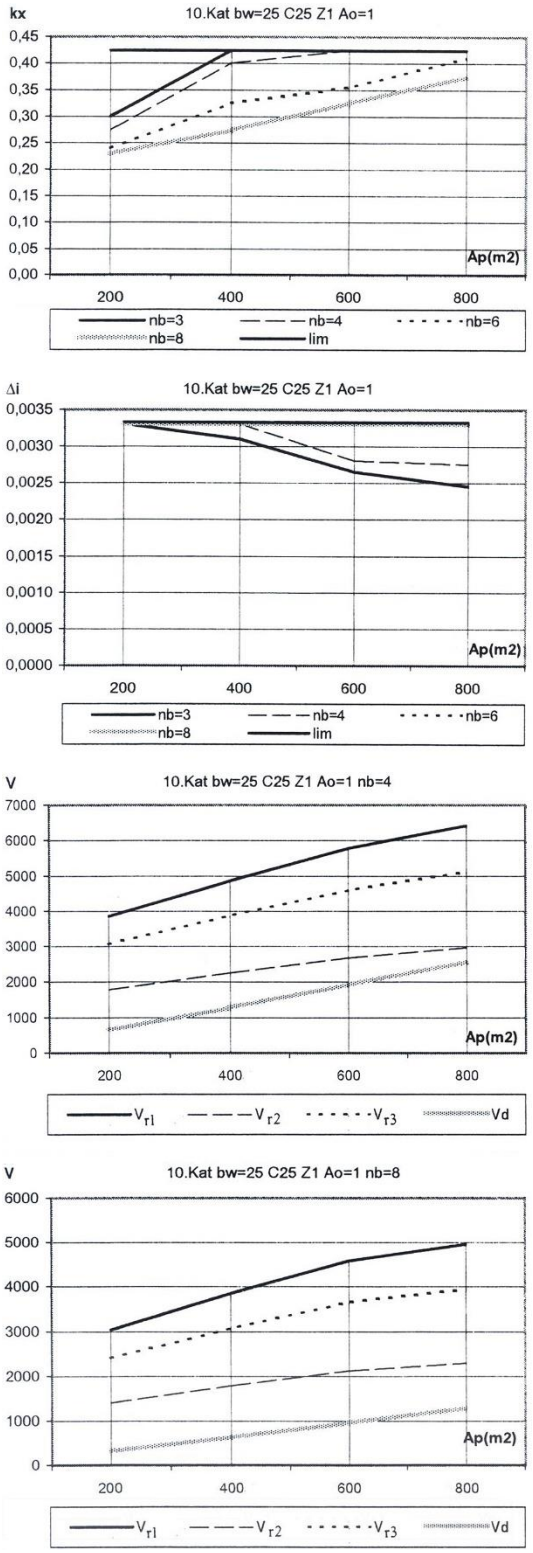

Fig. 3. k_x, storey displacement and shear force diagrams.

After dimensioning the shear walls by the minimum thickness given in earthquake codes, solutions of them under earthquake effects are made for structure behaviour coefficient for increased ductility and the overturning moment, shear force and axial force at the foundation is calculated. Then the necessary reinforcement can be calculated according to TS500, 2000 and the unit deformations ε_c and ε_s are established, which means that k_x and ρ are also established.

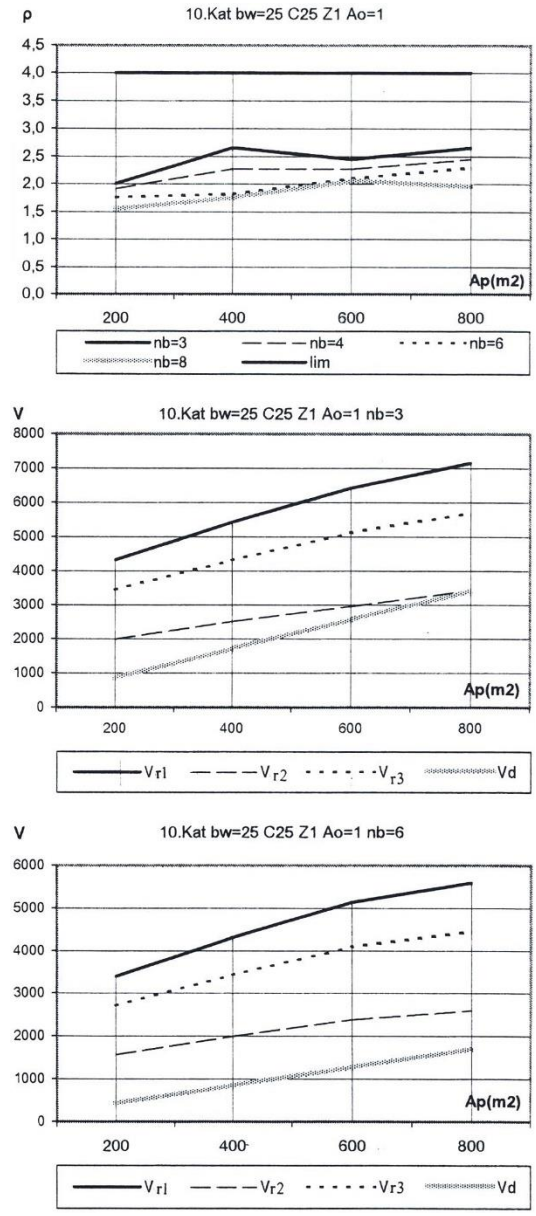

Fig. 4. ρ and shear force diagrams.

The first and the second criteria can be controlled with these, respectively. In case of exceedance of the limits for one of the criteria, one of the following steps can be made to ensure; a) changing the thickness of the shear wall, b) changing the length of the shear wall, c) adding another shear wall to the system. When the second criteria is ensured while the first criteria is not, which means the acceptance of non-increased shear wall ductility by the project- engineer, than the structure behaviour coefficient should be taken suitable to this situation and the earthquake forces should be recalculated.

5. Numerical Examples

5.1. Shear wall systems

The structural system consist of shear walls which will carry the horizontal loads in the earthquake risk zone. Storey area of the building is 600 m^2.

a) For seismic zone 1 (A_0=0.40), soil group Z3, N=13, material C25-S420a, n_b=6, b_w=30 cm, from Fig. 1, shear wall length is taken as l_w=740 cm.
With these values, W=96300 kN, T_1=0.784 s,
$S(T)$=2.018, V_t=12590 kN, M_t =336323 kNm.
P1 shear wall; n=0.130, m=0.204, k_x=0.300<0.423, ω=0.15, ρ=%3.4. P2; k_x=0.333, ρ=%3.3. P3; k_x=0.353, ρ=%3.1. P4; k_x=0.400, ρ=%2.9,
Shear forces;
V_d=2098 kN , $V_e<V_r$, $V_r=0.22A_{ch}f_{cd}$=8140 kN, ρ_{sh}=0.0025 , $V_r=A_{ch}(0.65f_{ctd}+\rho_{sh}f_{ywd})$=3758 kN, $V_r=A_{wf}f_{yd}\mu$=6260 kN , $(\delta_i)_{max}/h_i$=0.00333≤0.02 (H_w/l_w)=0.878<2 , (b_w/h)=1/10≥1/15.
b) For seismic zone 1 (A_0=0.40), soil group Z1, N=13, material C25-S420a, n_b=6, b_w=30 cm, l_w=620 cm.
c) For seismic zone 1 (A_0=0.40), soil group Z3, N=18, material C30-S420a, n_b=6, b_w=30 cm, l_w=940 cm.
d) For seismic zone 1 (A_0=0.40), soil group Z3, N=18, material C30-S420a, n_b=6, b_w=35 cm, l_w=890 cm.

5.2. Shear wall and frame systems

The structural system consist of shear walls and frames which will carry the horizontal loads in the earthquake risk zone. Storey area of the building is 400 m^2. W_p=0.75W.
a) For seismic zone 1 (A_0=0.40), soil group Z1, N=8, material C20-S420a, n_b=4, b_w=20 cm, l_w=480 cm.
b) For seismic zone 3 (A_0=0.20), soil group Z1, N=8, material C20-S420a, n_b=4, b_w=20 cm, l_w=390 cm.
c) For seismic zone 1 (A_0=0.40), soil group Z3, N=15, material C30-S420a, n_b=4, b_w=25 cm, l_w=870 cm.
d) For seismic zone 3 (A_0=0.20), soil group Z3, N=15, material C30-S420a, n_b=4, b_w=25 cm, l_w=690 cm.

The selected shear walls ensured the criteria given in part 3.

6. Conclusions

In this study, the calculation of systems consisting of shear walls which are perfectly resistant under earthquake effects and can be built quickly, is examined.

To determine the dimensions of earthquake shear walls in buildings, the following criteria are proposed. a) It is desired to have increased ductility in the structures which will be constructed in the first and the second degree earthquake risk zones. According to this, the k_x of the shear walls at the base with high ductility should be less than 0.423, b) The total reinforcement at the end cross-sections of the shear walls should be less than 0.002, c) The ratio of shear wall top horizontal displacement to the building height should be less than 0.02, d) There should not be any diagonal cracks in shear walls, d) The shear force capacity should be greater than the bending moment capacity in shear walls.

The average storey weight for percent area is determined by the use of TS498, 2000 and TNC, 2007 for constructed buildings having different storey areas in case of storey weights calculated for earthquake calculations. Total shear force, the overturning moment, the minimum and maximum values of axial forces of the shear walls at the basement and the top force are calculated for the buildings having number of storeys from 2 to 10 and storey areas from 100 m^2 to 800 m^2.

For N=10 and shear walls with the same size, the calculated l_{Ti}, l_{bi}, θ, ρ, ε_c, ε_s and k_x values for various n_b, A_0, A_p and W_p suitable to the first and the second criteria are given in diagrams.

With the same conditions but different number of storeys from N=10, such as N=N^*, the necessary lengths of shear walls $l_{bn}{}^*$ can be calculated as $l_{bn}{}^*=(N^*/10)l_{b10}$. On the other hand, the θ, ρ and k_x values obtained for $l_{bn}{}^*$ and for l_{b10} under the same conditions are equal to each other.

Lengths of shear walls can be pre-dimensioned before calculations by the use of these tables. Certainly, a definite calculation is necessary. It is explained how to design, if the lengths of the shear walls are given according to the architectural design, in part 4. The shear force which will be carried by the shear walls, should be less than defined maximum value.

Shear walls having cross-sections of [, L , I will be considered in another study.

REFERENCES

Altın S (1989). The behaviour of reinforced concrete shear-walls subjected to cyclic loading. *Earthquake Bulletin*, 67.

Andinç E (2004). Betonarme binalarda deprem perdelerinin boyutlandırılması. *M.Sc. thesis*, İstanbul Technical University, İstanbul, Turkey (in Turkish).

ATC 22 **(**1989). A Handbook for Seismic Evaluation of Existing Building: Supporting Documentation, Federal Emergency Management Agency, FEMA 178, California.

Atımtay E (2000). Açıklamalar ve Örneklerle Afet Bölgelerinde Yapılacak Yapılar Hakkındaki Yönetmelik (Betonarme Yapılar), (1-2). Bizim Büro, Ankara (in Turkish).

Aydoğan M, Öztürk T (2002). Betonarme yapılarda güçlendirme uygulamaları. *Prof. Dr. Kemal Özden'i Anma Semineri, Yapıların Onarım ve Güçlendirilmesi Alanında Gelişmeler*, İstanbul, Türkiye (in Turkish).

Celep Z, Kumbasar N (2004). Deprem Mühendisliğine Giriş ve Depreme Dayanıklı Yapı Tasarımı. Beta Dağıtım, İstanbul (in Turkish).

Celep Z, Kumbasar N (2005). Reinforced Concrete Structures. Beta Press, İstanbul.

Ersoy U (1993). Lessons to be learned from Erzincan 1992 earthquake. *Second Conference of National Earthquake Engineering*, 395-403, İstanbul.

Fintel M (1991). Shearwalls-An Answer for Seismic Resistance?. Concrete International, National Building Code of Canada, Ottawa.

Nilson AH, Winter G (1991). Design of Concrete Structures. McGraw-Hill, New York.

Özden K, Kumbasar N (1993). Reinforced Concrete Tall Buildings. ITU Faculty of Civil Engineering Press, Number 1510, İstanbul.

Paulay T, Priestley MJN (1992). Seismic Design of Reinforced Concrete and Masonary Buildings. John Wiley and Sons Inc., New York.

Tarenath S (1988). Structural Analysis and Design of Tall Buildings. McGraw-Hill, New York.

TS 498 (2000). Design Loads for Buildings. TSE-Standard Institute of Turkey.

TS 500 (2000). Turkish Building Code Requirements for Reinforced Concrete. TSE-Standard Institute of Turkey.

TS 9967 (1992). Design, Construction and Erection Methods for Precast Reinforced and Prestressed Concrete Elements, Structures and Buildings. TSE-Standard Institute of Turkey.

TNC (2007). Turkish National Code for Structures Built in Earthquake Risk Zones. Earthquake Research Institute.

Wakabayashi M (1986). Design of Earthquake-Resistant Buildings. McGraw-Hill, New York.

Challenge Journal of Structural Mechanics

Effect of severe corrosion upon natural frequencies of beam-like structures

Daniel Bobos, Zeno Iosif Praisach, Doina Frunzăverde, Gilbert Rainer Gillich *, Ionica Negru

Department of Mechanics and Material Engineering, Eftimie Murgu University of Resita, 320085 Resita, Romania

ABSTRACT

Corrosion, as the spontaneous process of material degradation produced by the environment, affects the reliability and safety of structures, both by reducing the section of the components, due to material loss and by diminution of the materials mechanical strength. The authors have found a mathematical relation between discontinuities in beams and changes of its natural frequencies and developed a method to identify these discontinuities. The present paper considers the more complex case of damage determined by corrosion, where beam thinning is accompanied by mass decrease. These impose considering natural frequency changes in both directions: decrease due damage and increase because of mass loss. FEM simulations and analytical investigations were carried out, in order to find the relation between mass change in different positions along the beam and the frequency increase. The results were correlated with the "classical" relation describing frequency decrease because of discontinuities. Finally, the authors developed a new relation, proper to be used for damage produced by severe corrosion, which was validated by laboratory experiments.

ARTICLE INFO

Article history:
Received 29 April 2015
Accepted 23 May 2015

Keywords:
Corrosion
Damage assessment
Beam
Natural frequency
Mode shape
Strain energy

1. Introduction

Corrosion is a consequence of the interaction between a material and its environment, which determines changes in the materials properties and often leads to impairment of the metals function, the environment or the technical system of which these form a part (ISO 8044-1986). The damage process is irreversible and leads to degradation of the material, accompanied by diminished performances of the technical system to which it belongs. The corrosion processes always trigger from the components surface, but sometimes penetrate deep inside the materials.

Several criteria are used to classify the different corrosion types. Regarding the corrosions mechanism, one can distinguish between: (a) chemical (dry) corrosion, as the heterogeneous corrosion process between a solid metallic phase and a gaseous phase (air, industrial gases); (b) electrochemical (wet) corrosion, which appears when metallic materials are in contact with an aggressive, liquid and conducting medium; when it occurs under the conditions of simultaneous mechanical load, result stress corrosion, fatigue corrosion or fretting corrosion and (c) biochemical corrosion, where the destruction of metal is caused by bacteria, fungi or other microbiological organisms under specific environmental conditions (DeGiorgi, 1992).

Another traditional classification (Landolfo et al., 2010) characterizes corrosion phenomena according to the appearance of the corroded area. Regarding this criterion, the basic forms of corrosion are: (i) continuous (generalized) corrosion, which can be both uniform, where the metal surface is affected at the same rate on large areas and nonuniform corrosion, characterized by different corrosion rates in different zones of the surface; (ii) localized corrosion, which is restricted to reduced areas and takes the form of pits, crevices or cavities.

From structural point of view, the loss of thickness of the cross section due to corrosion attack leads to a smaller bearing area, producing a decrease in the structural performance in terms of strength, stiffness and

* *Corresponding author*. Tel.: +40-355-405900 ; Fax: :+40-255-207501 ; E-mail address: gr.gillich@uem.ro (G. R. Gillich)
ISSN: 2149-8024 / DOI: http://dx.doi.org/10.20528/cjsmec.2015.05.010

ductility, thus shortening the designed life expectancy (Bazant, 1979; Apostolopoulos and Michalopoulos, 2007). In case of cyclic loads, the corrosion phenomenon can produce a significant reduction in the fatigue strength, mainly in zones with high stress concentration (Albrecht and Hall, 2003; Landolfo et al., 2005; Klinesmith, 2007). Especially in case of uniform corrosion the loss of material mass is significant, bringing up difficulties when dynamic methods are used for corrosion assessments. While corrosion is a major problem, it concerned the attention of researchers, but only recently they gave attention to the joined effects of stiffness and mass loss.

Our previous researches considered the influence of local, transversal damages without loss of mass upon dynamic behavior of beams and established a simple, reliable method to asses these damages. Recent investigations considering the influence of local corrosion on the dynamic behavior of beams were performed, with focus both on stiffness changes and loss of mass. This paper presents the results obtained and considerations how these can be used to improve damage detection methods.

2. Analytical Investigations

For this paper we have chosen to present the cantilever beam, which due to its asymmetry is more complex, but uniquely defines the damage/corrosion location. For demonstration we used a steel cantilever beam with rectangular cross section (Fig. 1) having the following geometry: length L = 600 mm; width B = 50 mm and height H = 5 mm. Consequently, for the undamaged state, the beam has the cross-section $A = 250\text{-}10^{6}$ m^2 and the moment of inertia $I = 520.833\text{-}10^{-12}$ m^4. The mechanical parameters of the specimens' material are: mass density $\rho = 7850$ kg/m^3; Young's modulus $E = 2.0\text{-}10^{11}$ N/m^2 and Poisson's ratio m = 0.3. The earth gravity is considered $g = 9.806$ m/s^2 and the mass of the beam is m = 1.1775 kg. On the cantilever beam acts only its own mass.

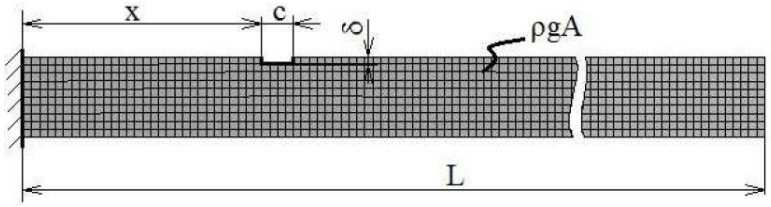

Fig. 1. Cantilever beam with damage.

The natural frequencies Eq. (1) for the cantilever beam is presented below:

$$f_n = \frac{a_n^2}{2\pi}\sqrt{\frac{EI}{mL^3}}, \tag{1}$$

where, the wave numbers a_n of Euler-Bernoulli model are the solution of Eq. (2) for n vibration modes:

$$cos\, a + cos\, h + 1 = 0\,. \tag{2}$$

At distance x from clamped end (Fig. 1) it is considered a damage/corrosion area of 2 mm wide during the whole width of the beam with a small depth of 8% from beam height, respectively 0.4 mm depth.

Taking in consideration that for the cantilever beam the deflection v at the free end is:

$$v = \frac{pgAL^4}{8EI} = \frac{mL^3}{8EI}, \tag{3}$$

for the damaged beam the deflection v_D can be written:

$$v_D = \frac{m(x,\delta)L^3}{8EI(x,\delta)}, \tag{4}$$

and consequently, the natural frequencies equation for the damaged beam f_{Dn} becomes:

$$f_{Dn} = \frac{a_n^2}{2\pi}\sqrt{\frac{EI(x,\delta)}{m(x,\delta)L^3}}. \tag{5}$$

According to relation (5), the natural frequencies for the damaged/corroded beam depends of moment of inertia $I(x,\delta)$ and mass $m(x,\delta)$. In the corroded area on the beam, when mass loss is significant compared to reducing the moment of inertia we can consider that $I(x,\delta) \sim I$. The natural frequencies for the corroded beam depends only the terms $m(x,\delta)$.

In this case, the relative frequency shift (Gillich and Praisach, 2012; Gillich et al., 2012a) can be written:

$$\Delta f = \frac{f - f_D}{f} = 1 - \frac{f_D}{f}, \tag{6}$$

but the relative frequency shift for the corroded beam Δf_C is,

$$\Delta f_C = 1 - \frac{f_D}{f} = 1 - \frac{\frac{a_n^2}{2\pi}\sqrt{\frac{EI}{m(x,\delta)L^3}}}{\frac{a_n^2}{2\pi}\sqrt{\frac{EI}{mL^3}}} = 1 - \frac{\sqrt{m}}{\sqrt{m(x,\delta)}} = \frac{\sqrt{m(x,\delta)} - \sqrt{m}}{\sqrt{m(x,\delta)}}, \tag{7}$$

and taking in consideration the relation of natural frequency for the damaged beam (Gillich and Praisach, 2012), the natural frequency for the corroded beam becomes:

$$f_{Cn} = f_n\left(1 - \frac{\sqrt{m(x,\delta)} - \sqrt{m}}{\sqrt{m(x,\delta)}}(\bar{\phi}(x))^2\right)$$

$$= f_n\left(1 + \frac{\sqrt{m} - \sqrt{m(x,\delta)}}{\sqrt{m(x,\delta)}}(\bar{\phi}(x))^2\right), \tag{8}$$

where $\bar{\phi}(x)$ is the normalized mode shape curvature of the cantilever beam.

In the damaged beam the reducing of moment of inertia and loss mass is significant. Taking in consideration only the reducing of moment of inertia $m(x,\delta)\sim m$ and relations (3) and (4) the relative frequency shift Δf_D is:

$$\Delta f_D = 1 - \frac{f_D}{f} = 1 - \frac{\frac{a_n^2}{2\pi}\sqrt{\frac{EI}{m(x,\delta)L^3}}}{\frac{a_n^2}{2\pi}\sqrt{\frac{EI}{mL^3}}} = 1 - \frac{\sqrt{\frac{1}{8v_D}}}{\sqrt{\frac{1}{8v_D}}}$$
$$= 1 - \frac{\sqrt{v}}{\sqrt{v_D}} = \frac{\sqrt{v_D}-\sqrt{v}}{\sqrt{v_D}}, \quad (9)$$

and the natural frequency for the damaged beam (Gillich et al., 2012b) without taking in consideration the mass loss:

$$f_{Dn} = f_n\left(1 - \frac{\sqrt{v_D}-\sqrt{v}}{\sqrt{v_D}}\right)\left(\frac{\partial^2\bar{\phi}(x)}{\partial x^2}\right)^2. \quad (10)$$

Taking in consideration the mass loss (8) and reducing the moment of inertia (10), the natural frequency for the damaged beam can be written:

$$f_{Dn} = f_n\left(\begin{array}{c}\left(1 - \frac{\sqrt{v_D}-\sqrt{v}}{\sqrt{v_D}}\right).\left(\frac{\partial^2\bar{\phi}(x)}{\partial x^2}\right)^2 \\ + \frac{\sqrt{m}-\sqrt{m(x,\delta)}}{\sqrt{m(x,\delta)}}(\bar{\phi}(x))^2\end{array}\right). \quad (11)$$

The damage location index (12) can be obtained from fracture mechanics by using the following formula:

$$\frac{\sqrt{v_D}-\sqrt{v}}{\sqrt{v_D}} = 5.346h\pi.P\left(\frac{\delta}{h}\right), \quad (12)$$

where (Ostachowicz and Krawczuk, 1991)

$$P\left(\frac{\delta}{h}\right) = 1.862\left(\frac{\delta}{h}\right)^2 - 3.95\left(\frac{\delta}{h}\right)^3 + 16.375\left(\frac{\delta}{h}\right)^4 - 37.226\left(\frac{\delta}{h}\right)^5 +$$
$$76.81\left(\frac{\delta}{h}\right)^6 - 126\left(\frac{\delta}{h}\right)^7 + 172\left(\frac{\delta}{h}\right)^8 - 172\left(\frac{\delta}{h}\right)^9 - 66.56\left(\frac{\delta}{h}\right)^{10}. \quad (13)$$

3. Numerical Investigations

Investigations using the finite element method were performed on a cantilever beam, first case for the undamaged beam, second case for a cantilever beam with damage and mass loss (Fig. 1) and third case a geometrical undamaged beam where in the presumed damaged area of wide c = 2 mm the original material was replaced with a new one (Fig. 2), having the mass density reduced in order to assure the same total beam mass like that of the damaged beam.

The 3D beam with the geometrical characteristics and material parameters presented in chapter 2, was meshed by 0.5 mm elements in all cases. In order to compare analytical investigations with numerical results, were considered 197 locations of the damage on the beam length, both for damaged beam with mass loss (case two) presented in Fig. 1 and theoretical undamaged beam (case three) presented in Fig. 2. For all the cases were determined the maximum deflection and the first ten natural frequencies of the weak-axes bending vibration modes, used to highlight the frequency changes in a graphical way.

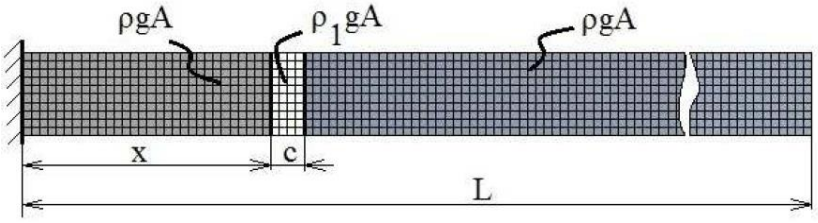

Fig. 2. Undamaged cantilever beam.

Fig. 3 presents the natural frequencies for the damaged beam with mass loss for the first, second, third and fourth vibration mode. The dashed line represents the natural frequencies obtained by numerical analysis and the continuous line represents the natural frequencies obtained analytic with relation (10).

Fig. 4 presents the natural frequencies for the geometrical undamaged beam but with loss of mass, for the first, second, third and fourth vibration mode. The dashed line represents the natural frequencies obtained by numerical analysis and the continuous line represents the natural frequencies obtained analytic with relation (8).

Fig. 5 presents the natural frequencies for the damaged beam without mass loss, for the first, second, third and fourth vibration mode. The dashed line represents the natural frequencies obtained by numerical analysis for damaged beam and undamaged beam with reduced mass and the continuous line represents the natural frequencies obtained analytic with relation (10).

For Figs. 3 to 5 the dash-dotted line represents the natural frequency of the undamaged beam.

The dashed lines presented in Fig. 5 are obtained as difference between numerical results of natural frequencies for the damaged beam with mass loss (Fig. 3) and numerical results of natural frequencies for the undamaged beam with reduced mass (Fig. 4). It can be observes the good concordance of the corrected results obtained by numerical analysis and that obtained by means of fracture mechanics.

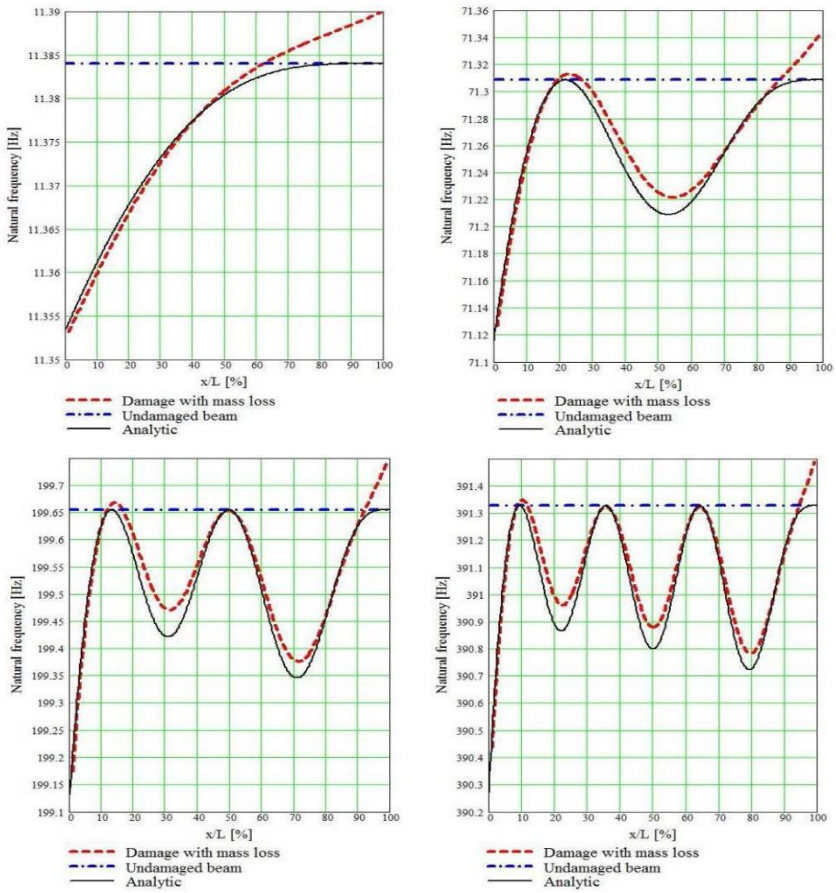

Fig. 3. Natural frequencies for the damaged beam with mass loss (first, second, third and fourth vibration modes).

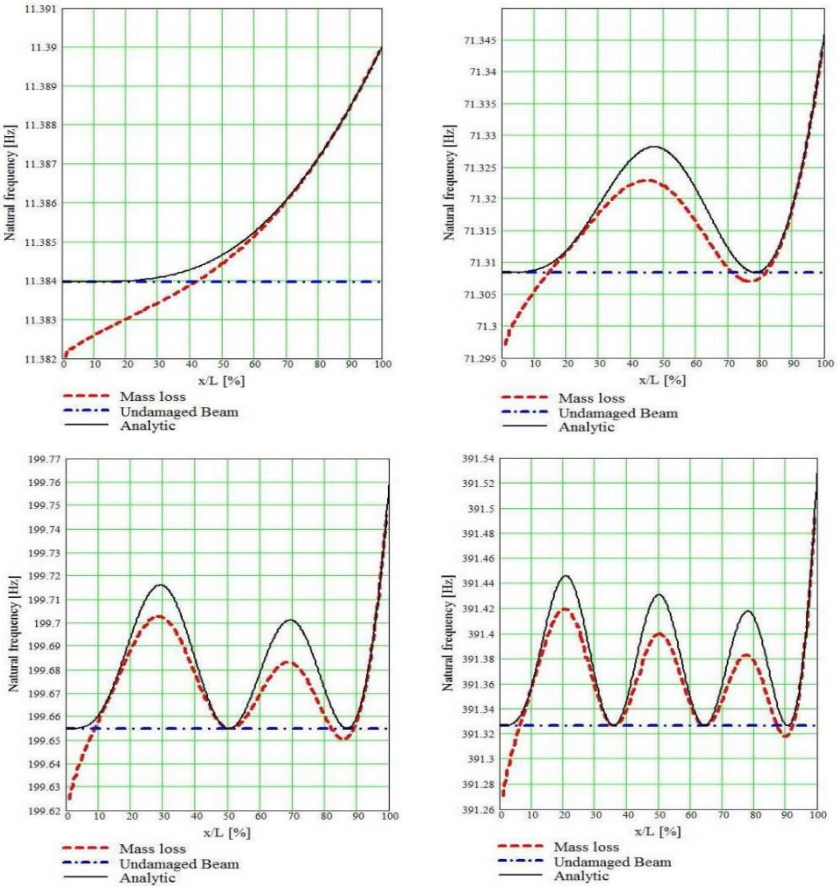

Fig. 4. Natural frequencies for the undamaged beam with reduced mass (first, second, third and fourth vibration modes).

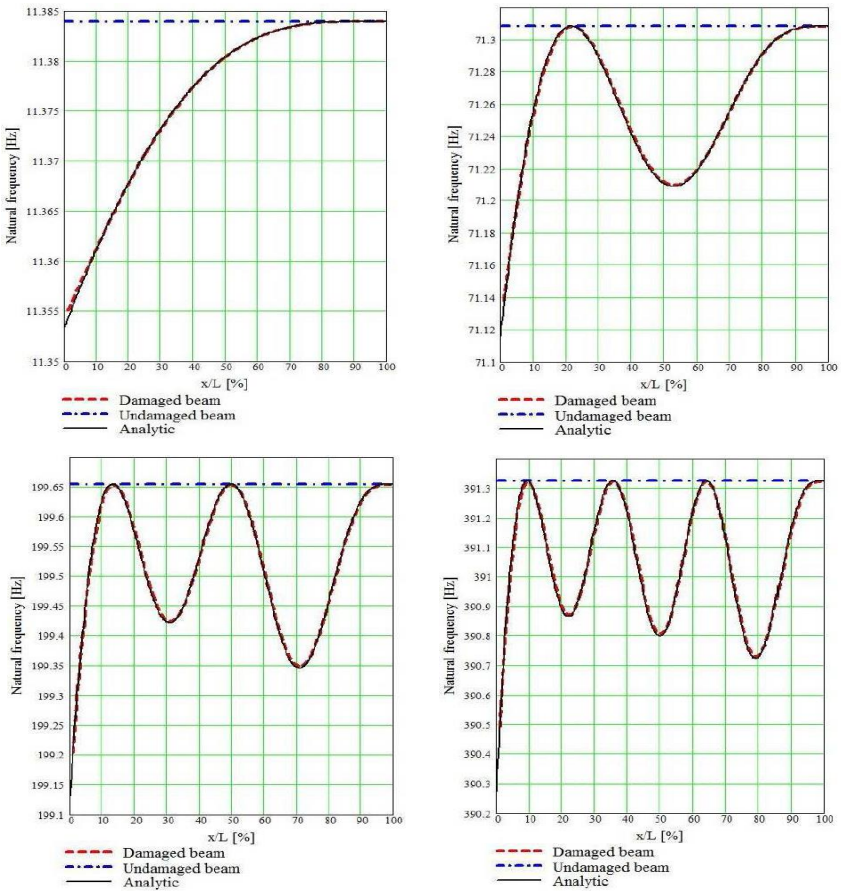

Fig. 5. Natural frequencies for the damaged beam (first, second, third and fourth vibration modes).

4. Laboratory Experiments

We conducted experiments on the cantilever beam to find the first ten natural frequencies of the undamaged and damaged beam. During the tests, the beams where fixed in a milling machine and the excitation of the structure was realized by hitting with a hammer. The measurement system was composed by a laptop, a NI cDAQ-9172 compact chassis with NI 9234 four-channel dynamic signal acquisition modules and a Kistler 8772 accelerometer mounted near the free end of the beam. Using virtual instruments created in LabVIEW we acquired the acceleration time history and identified the first ten weak-axis bending vibration modes. For the damaged case, the effect of corrosion was simulated by saw cuts, of around 2 mm wide and 0.5 mm depth. The damage is located at $x/L = 0.595$.

The natural frequencies for the first ten vibration mode, for the undamaged and damaged beam obtained analytically (10), numerically by finite element method and measured are presented in Table 1.

To compare the obtained results presented in Table 1 is useful to represents the normalized frequency shift versus vibration mode (Fig. 5). The normalized frequency shift (Table 2) is the relative frequency shift divided by maximum of the relative frequency shift (highlighted with bold characters in Table 1) of the ten vibration modes.

Table 1. Natural frequencies for the undamaged (f_U) and damaged (f_D) beam with damage located at $x/L = 0.595$.

Vibration mode	Natural frequencies					
	Analytic Euler-Bernoulli		Numerical		Measured	
n	f_{U_A} [Hz]	f_{D_A} [Hz]	f_{U_FEM} [Hz]	f_{D_FEM} [Hz]	f_{U_M} [Hz]	f_{D_M} [Hz]
1	11.3247	11.3237	11.3840	11.3834	11.3564	11.3552
2	70.9709	70.8803	71.3084	71.2263	71.0215	70.9302
3	198.7205	198.5839	199.6549	199.5339	199.0212	198.8811
4	389.4129	389.2844	391.3266	391.2133	389.5088	389.3814
5	643.7275	642.9087	647.1184	646.4253	648.027	647.1995
6	961.6174	961.611	967.0326	967.0125	966.0025	965.9832
7	1343.0854	1341.5112	1350.994	1349.6439	1345.3657	1343.7714
8	1788.1315	1787.2082	1798.7638	1797.9662	1792.2048	1791.1582
9	2296.7556	2295.7555	2309.9327	2309.0230	2306.3294	2305.4299
10	2868.9577	2865.4446	2883.9323	2880.9621	2878.4419	2874.9624

Table 2. Relative frequency shift (Δf) and normalized frequency shift ($N\Delta f$) for damaged beam with damage at x/L = 0.595.

Vibration mode	Relative frequency shift & Normalized frequency shift					
	Analytic Euler-Bernoulli		Numerical		Measured	
n	Δf_A [%]	$N\Delta f_A$	Δf_{FEM} [%]	$N\Delta f_{FEM}$	Δf_M [%]	$N\Delta f_M$
1	0.0088	0.068912	0.0053	0.042535	0.0102	0.079377
2	0.1277	1.000000	0.1152	1.000000	0.1285	1.000000
3	0.0688	0.538763	0.0606	0.526042	0.0704	0.547860
4	0.0330	0.258418	0.0290	0.251736	0.0327	0.254475
5	0.1272	0.996085	0.1071	0.929688	0.1277	0.993774
6	0.0007	0.005482	0.0021	0.018229	0.0020	0.015564
7	0.1172	0.917776	0.1000	0.868056	0.1185	0.922179
8	0.0516	0.404072	0.0443	0.384549	0.0584	0.454475
9	0.0435	0.340642	0.0394	0.342014	0.0390	0.303502
10	0.1224	0.958496	0.1030	0.894097	0.1209	0.940700

It can be observed a very good correlation between analytic method, numerical analysis and measured results for a damaged beam. The normalized frequency shift in respect to the vibration mode presented in Fig. 6 uniquely characterizes the frequency changes for an asymmetrical beam. Thus, the damage location indexes can be used to precisely identify the location of a crack, without caring about its depth.

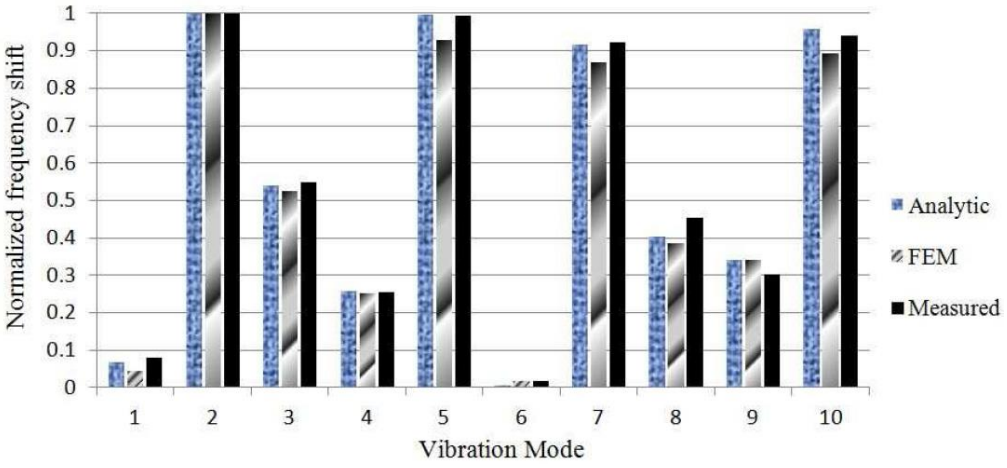

Fig. 6. Normalized frequency shift versus vibration mode.

5. Conclusions

Corrosion, as degeneration of materials, affects the reliability and safety of structures by producing loss of material together with thinning of components and consequently reduction of mechanical strength and stiffness. These two aspects are rarely considered together, since the phenomenon is complex and solutions in this case require intensive time and resources consumption.

This paper consider the case of damage due corrosion, where beam thinning is accompanied by mass loss. The relation prior contrived between deflection and frequency changes is used, completed with one found between mass loss in a given location and the resulting frequency increase. This fact reveals that for damages with mass loss, the natural frequency of the undamaged structure as a reference value is inadequate, being necessary to adjust it with a term dependent on the loss of mass and the value of the mode shape at the damage location.

Acknowledgements

The work has been co-funded by the Sectoral Operational Programme Human Resources Development 2007-2013 of the Romanian Ministry of Labour, Family and Social Protection through the Financial Agreement POSDRU/89/1.5/S/62557.

References

Albrecht P, Hall TT (2003). Atmospheric corrosion resistance of structural steels. *Journal of Materials in Civil Engineering*, 15, 2-24.

Apostolopoulos CA, Michalopoulos D (2007). Impact of corrosion on mass loss, fatigue and hardness of BSt500 Steel. *Journal of Materials Engineering and Performance*, 16(1), 63-67.

Bazant ZP (1979). Physical model for steel corrosion in concrete sea structures-Theory. *Journal of Structural Division*, 105(6), 1137-1153.

DeGiorgi VG (1992). Corrosion Basics and Computer Modelling in Industrial Application of the BEM. Computational Mechanics Publication, Southampton.

Gillich GR, Praisach (2012). Robust method to identify damages in beams based on frequency shift analysis. *Conference on Health Monitoring of Structural and Biological Systems*, San Diego (CA), USA, 84381D1-12.

Gillich GR, Praisach ZI, Iavornic CM (2012a). Reliable method to detect and assess damages in beams based on frequency changes. *Proceedings of the ASME 2012 International Design Engineering Technical Conference*, Chicago (IL), USA, DETC2012-70094.

Gillich GR, Minda PF, Praisach ZI, Minda AA (2012b). Natural frequencies of damaged beams - a new approach. *Romanian Journal of Acoustics and Vibration*, 9(2), 101-108.

ISO 8044 (1986). Corrosion of metals and alloys - Terms and definitions.

Klinesmith DE, McCuen R, Albrecht P (2007). Effect of environmental condition on corrosion rate. *Journal of Materials in Civil Engineering*, 19, 121-129.

Landolfo R, Cascini L, Portioli P (2010). Modeling of metal structure corrosion damage: A State of the art report, sustainability, 2, 2163-2175.

Landolfo R, Di Lorenzo G, Guerrieri MR (2005). Modeling of the damage induced in atmospheric corrosion of 19th century iron structures. *Proceedings of the Italian National Conference on Corrosion and Protection*, Senigallia (Ancona), Italy.

Ostachowicz WM, Krawczuk C (1991). Analysis of the effect of cracks on the natural frequencies of a cantilever beam. *Journal of Sound and Vibration*, 150(2), 191-201.

Challenge Journal of Structural Mechanics

Free vibration analysis of thick plates resting on Winkler elastic foundation

Korhan Özgan, Ayşe T. Daloğlu *

Department of Civil Engineering, Karadeniz Technical University, 61080 Trabzon, Turkey

ABSTRACT

The purpose of this study is to determine the effects of various parameters such as the aspect ratio, subgrade reaction modulus and thickness/span ratio on the frequency parameters of thick plates resting on Winkler-type elastic foundations. For this purpose, 4-noded (PBQ4) and 8-noded (PBQ8) Mindlin plate elements are adopted for the analysis using Winkler foundation model. Two different integration rules, namely the full integration (FI) and the selective reduced integration (SRI) techniques, are used to obtain stiffness matrix of plates. The results obtained in this study are compared with the results that are obtained by SAP2000 structural analysis software.

ARTICLE INFO

Article history:
Received 13 May 2015
Accepted 16 June 2015

Keywords:
Finite element method
Thick plate theory
Elastic foundation
Winkler model
Free vibration

1. Introduction

The dynamic response of plates resting on elastic foundation is an important tool in understanding the dynamic behaviour of many engineering problems. In general, the analysis of this problem is based on the incorporation of the foundation reaction into the corresponding differential equation of plates. Different models for the foundation plates have been proposed to provide more efficient and practical solutions. The simplest model is the Winkler model which is also called as one parameter model. This model can be considered as an idealization of the soil medium by a number of mutually independent springs and the vertical displacements of the plate are assumed to be proportional at every point to the contact pressure. Although it has some difficulties, Winkler model is widely used because of its simplicity.

In the classical plate theory which is known as Kirchhoff plate theory, the effect of the shear deformation through the plate thickness is ignored. However the effect of the shear deformation becomes important as the thickness of the plate increases. For this reason, it is obvious that shear deformation has to be taken into account especially for the thick plates. Mindlin plate elements are fundamentally simple to adopt for modelling the shear deformation behaviour of the thick plates. But Mindlin plate element has shear locking problem when a thin plate is considered. Reduced integration and selective reduced integration techniques have been proposed in many studies to avoid this problem.

Some of the studies on this topic is as follows. Shen et al. (2001) investigated effects of the parameters such as foundation stiffness, transverse shear deformation and plate aspect ratio on dynamic response of Reissner-Mindlin plates resting on Pasternak type elastic foundation. Malekzadeh (2009) presented an accurate solution procedure based on the three-dimensional elasticity theory for the free vibration analysis of thick functionally graded plates on two-parameter elastic foundation. Leung and Zhu (2005) presented an analytical trapezoidal hierarchical element for the transverse vibration of Mindlin plates resting on two parameter foundation using Legendre orthogonal polynomials to avoid shear locking problem. Omurtag et al. (1997) studied the free vibration analysis of Kirchhoff plates resting on elastic foundation using Gateaux differential. Zhou et al. (2006) investigated the effects of various thickness-radius ratios, foundation stiffness parameters and boundary conditions on the dynamic behavior of the thick circular plates on elastic foundation. Jedrysiak (2003) calculated

* *Corresponding author*. Tel.: +90-462-3772662 ; Fax: +90-462-3772606 ; E-mail address: aysed@ktu.edu.tr (A. T. Daloğlu)
ISSN: 2149-8024 / DOI: http://dx.doi.org/10.20528/cjsmec.2015.06.015

frequencies of thin plates interacting with an elastic periodic foundation. Zhong and Yin (2008) investigated the free vibration behavior of plate on elastic foundation by finite integral transform method using Winkler foundation method. Tovstik (2009) studied vibration and stability of a prestressed plate on elastic foundation. Hsu (2010) numerically modelled the vibration behaviour of orthotropic plates on nonlinear elastic foundations.

In this study, 4-noded (PBQ4) and 8-noded (PBQ8) Mindlin plate elements that includes the effects of shear deformation are adopted for the free vibration analysis of the thick plates resting on Winkler foundation. A computer program using finite element method is coded in FORTRAN to calculate stiffness and mass matrices of the system and then MATLAB for Windows 5.3 is used to obtain the solution of the generalized eigenvalue problem.

2. Mathematical Model

The equation of motion for a plate-soil system subjected to free vibration without damping is

$$[M]\{\ddot{w}\} + [K]\{w\} = 0\,, \tag{1}$$

where $[K]$ is the stiffness matrix of the plate-soil system, $[M]$ is the mass matrix of the plate-soil system, w and $\ddot{w}$ are the displacement and acceleration of the plate, respectively.

The subsoil has a finite depth on a rigid base at the bottom. The total potential energy of plate-soil system without load can be expanded as

$$\Pi = \frac{1}{2}\int [B]^T [D][B] dA + \frac{1}{2}\int [w(x,y)]^T\, k[w(x,y)] dA\,, \tag{2}$$

where $[B]$ is strain displacement matrix, $[D]$ is the material matrix and k is the subgrade reaction modulus of the Winkler-type foundation. In this study 4-noded (PBQ4) and 8-noded (PBQ8) quadrilateral rectangular finite elements based on Reissner-Mindlin theory are used to develop the element stiffness matrix. In these elements, nodal displacements at each node are

$$w, \varphi_x, \varphi_y\,, \tag{3}$$

where w is the transverse displacement, φ_x and φ_y are the rotations. The rotations φ_x and φ_y are independent, and are not related to w by differentiation. Displacement shape functions are given as

$$[N_i] = [N_1 \;\; 0 \;\; 0 \;\; N_2 \;\; 0 \;\; 0 \;\; \ldots \;\; N_n \;\; 0 \;\; 0]\,, \tag{4}$$

in which n is equal to 4 for PBQ4 and 8 for PBQ8. Shape functions can be found in explicit forms Weaver and Johnston (1984). After the standard procedures of finite element method are applied, the stiffness matrices of the plate-soil system can be evaluated as

$$U = \frac{1}{2}\{w_e\}^t\left([k_p] + [k_w]\right)\{w_e\}\,, \tag{5}$$

where $[k_p]$ and $[k_w]$ are stiffness matrix of the plate and stiffness matrix of the Winkler foundation, $\{w_e\}$ is the nodal displacement vector. More explanation is given in Özgan and Daloğlu (2007, 2009).

The Winkler foundation element stiffness matrices for PBQ4 and PBQ8 are given in explicit forms in Özgan and Daloğlu (2007).

The dynamics of elastic structures include the kinetic energy of the plate in addition to the strain energy. Evaluation of the mass matrix of plate-subsoil system is based on Hamilton's variational principle with the kinetic energy of

$$\pi_k = \frac{1}{2}\int_\Omega \{\dot{w}\}^T [\mu]\{\dot{w}\} d\,, \tag{6}$$

where $\{\dot{w}\}$ represents the partial derivative of the vector of generalized displacement with respect to time variable and $[\mu]$ is the mass density matrix. See reference Özgan and Daloğlu (2009) for the evaluation of mass matrices.

After substituting $w = W \sin \omega t$ into the governing equation for a plate subjected to free vibration with no damping given Eq. (1), one can obtain

$$([K] - \omega^2[M])\{W\} = 0 \pi_k = \frac{1}{2}\int_\Omega \{\dot{w}\}^T [\mu]\{\dot{w}\} d\,, \tag{6}$$

where $\{W\}$is a vector of mode shape of vibration and λ (λ=ω^2, ω is the circular frequency) is the frequency parameter. The eigenvalue solution of this equation yields frequency parameters and the corresponding mode shapes (Kolar and Nemec, 1989).

3. Numerical Examples

The plate considered for the numerical analysis in this study has 10 m length in the x and y direction and 0.5 m thickness in the z direction. The modulus of elasticity and Poisson ratio of the plate are 27.10^9 N/m^2 and 0.20 respectively. The subgrade reaction modulus of the Winkler-type foundation is $5{\cdot}10^6$ N/m^3. For the dynamic analysis, the mass density of the plate is taken as 2500 kg/m^3. 5 finite elements in the each direction for PBQ8 elements are enough for desired accuracy while 10 finite elements are required for PBQ4 elements. The example is analyzed by MZC element and SAP2000 structural analysis software in addition to the elements presented in this study and comparisons are made. MZC element based on Kirchhoff plate theory is commonly used for the thin plates due to it ignores shear deformation effects through the thickness of the plate. In the solution of SAP2000, the option of thick plate element is selected. Results are presented in Table 1 and Fig. 1.

As can be seen form figure, curves for PBQ4(FI) and PBQ4(SRI) become different from that of other solutions after 5th and 4th frequency parameter respectively. While PBQ4(FI) produces higher frequency values, PBQ4(SRI) produces lower frequency values than expected. It is seen that selective reduced integration in the PBQ4 element cannot be satisfactory for the free vibration analysis of the thick plate on Winkler-type foundation. PBQ8

elements are in good agreement with the solution of SAP2000 commercial software. But it is observed that PBQ8(SRI) element is getting closer to SAP2000 results compare to the solution by PBQ8(FI) element for the higher frequency parameters. Therefore, further analysis will be done by PBQ8(SRI) element.

The same example is analyzed for the various thickness/span ratio, aspect ratio and subgrade reaction modulus to demonstrate the effects of these parameters on the frequency parameters of the plate. Subgrade reaction modulus is taken as $5{\cdot}10^5$, $5{\cdot}10^6$ and $5{\cdot}10^7$ N/m^3. Aspect ratios are taken as 1.0, 1.5 and 2.0 for each subgrade reaction modulus as the length of the plate in the *x* direction is fixed. Thickness/span ratios are used as 0.05, 0.10 and 0.20 for each aspect ratio. Results obtained are presented in Table 2.

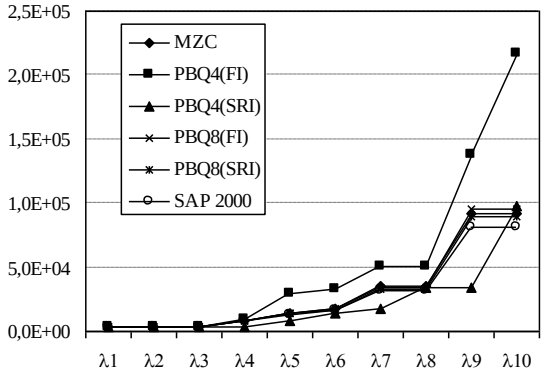

Fig. 1. The variation of the first ten frequency parameters of the plate.

Table 1. The first six frequency parameters of the plate.

l_y/l_x	h/l_x	Finite Element	Frequency Parameters					
			l_1	l_2	l_3	l_4	l_5	l_6
1.0	0.05	MZC	3997.50	3997.50	4000.00	8804.58	13951.08	17177.13
		PBQ4(FI)	3990.02	3990.02	4000.00	8893.01	29689.66	32970.03
		PBQ4(SRI)	3990.02	3990.02	4000.00	4000.00	8612.76	14022.42
		PBQ8(FI)	3990.42	3990.42	4000.40	8676.00	13957.64	17252.34
		PBQ8(SRI)	3990.02	3990.02	4000.00	8578.23	13794.58	16961.24
		SAP2000	4000.00	4000.00	4000.00	8619.60	13292.31	16380.24

Table 2. The first six frequency parameters of plates for various values of subgrade reaction modulus, aspect ratio and thickness/span ratio.

k (kN/m^3)	l_y/l_x	h/l_x	Frequency Parameters					
			l_1	l_2	l_3	l_4	l_5	l_6
500	1.0	0.05	399.00	399.00	400.00	4949.59	10231.94	13396.65
		0.10	198.02	198.02	200.00	17437.39	37666.67	49498.74
		0.20	96.15	96.15	100.00	58636.52	136957.06	164973.65
	1.5	0.05	399.00	399.56	400.00	2436.71	2613.35	10882.97
		0.10	198.02	199.11	200.00	7942.38	8851.53	39138.63
		0.20	96.15	98.25	100.00	27278.64	31856.42	127158.72
	2.0	0.05	399.00	399.75	400.00	1103.32	1531.07	5747.27
		0.10	198.02	199.50	200.00	2977.62	4521.19	20362.94
		0.20	96.15	99.00	100.00	10663.40	15473.41	68531.00
5000	1.0	0.05	3990.02	3990.02	4000.00	8578.23	13794.58	16961.24
		0.10	1980.20	1980.20	2000.00	19205.93	39396.66	51233.02
		0.20	961.53	961.53	1000.00	59482.04	127744.03	165770.71
	1.5	0.05	3990.02	3995.56	4000.00	6024.68	6196.79	14460.22
		0.10	1980.19	1991.15	2000.00	9718.92	10619.45	40895.87
		0.20	961.53	982.53	1000.00	28136.04	32699.08	127989.70
	2.0	0.05	3990.02	3997.50	4000.00	4694.02	5120.43	9326.86
		0.10	1980.20	1995.01	2000.00	4759.35	6300.29	22131.76
		0.20	961.53	990.10	1000.00	11529.30	16334.51	69377.88
50000	1.0	0.05	39900.05	39900.05	40000.00	44414.56	49420.66	52606.77
		0.10	19801.71	19801.71	20000.00	36891.06	56695.87	68575.33
		0.20	9614.85	9614.85	10000.00	67936.66	135612.65	173740.39
	1.5	0.05	39900.05	39995.42	40000.00	41904.25	42030.80	50232.52
		0.10	19801.71	19911.28	20000.00	27484.05	28298.20	58467.89
		0.20	9614.85	9824.98	10000.00	36709.57	41127.01	136298.93
	2.0	0.05	39900.05	39974.83	40000.00	40600.62	41013.90	45122.41
		0.10	19801.71	19949.92	20000.00	22576.27	24091.16	39819.77
		0.20	9614.85	9900.71	10000.00	20187.69	24945.02	77846.19

Fig. 2 shows the variation of first six frequency parameters with the aspect ratio for k=5·10^6 N/m^3. As seen from figures, aspect ratio don't affect the frequency parameters of the plate for the first three frequency parameter but the frequency parameters of the plate decrease as the aspect ratio increase after 3rd frequency parameters. This decrease is greater for the larger thickness/span ratio. While the curves are concave for 4th and 5th frequency parameters, the curves become convex for 6th frequency parameters. Namely; while the decrease in the 4th and 5th frequency parameters of the plate with increasing aspect ratio decrease for larger values of aspect ratio, the opposite situation arises in the 6th frequency parameters of the plate

Fig. 3 shows the variation of first six frequency parameters with subgrade reaction modulus for l_y/l_x=1.0. Frequency parameters of the plate increase as the subgrade reaction modulus of the subsoil increases. The increase in the frequency parameters of the plate with the increasing subgrade reaction modulus becomes greater for larger value of subgrade reaction modulus of subsoil. First three frequency parameters of the plate are similar to each other but after 3rd frequency parameters, the increase in the frequency parameters with increasing subgrade reaction modulus of the subsoil decrease.

The frequency parameters of the plate decrease with increasing thickness/plate ratio for first three frequency parameters, but the frequency parameters increase with increasing thickness/span ratio after 3rd frequency parameters. It is noted that some exceptional circumstances arise for k=5·10^7 N/m^3.

In this study, mode shapes of the plate are also obtained for all parameters considered but only mode shapes corresponding to six lowest frequency parameters for k=5·10^6 N/m^3, h/l_x=0.05 and l_y/l_x=2.0 are presented since the presentation of all mode shapes would take up excessive space. These mode shapes are given in Fig. 4.

4. Conclusions

A 4-noded (PBQ4) and an 8-noded (PBQ8) Mindlin plate elements are adopted for the analysis of plates on elastic foundation using Winkler model, and the effects of subgrade reaction modulus of the subsoil, aspect ratio and thickness/span ratio on the frequency parameter of the plate are investigated. This analysis is carried out by using Matlab for Windows 5.3 for the solution of the generalized eigenvalue problem including stiffness and mass matrices that are evaluated by a computer program coded for the purpose using finite element method. Following conclusions can be drawn from the results obtained in the study.

- Results show that PBQ8 element can be used effectively for the free vibration analysis of the plate on Winkler-type elastic foundation.
- Aspect ratio don't affect the frequency parameters of the plate for the first three frequency parameter but the frequency parameters of the plate decrease with increasing the aspect ratio after 3rd frequency parameters.
- The frequency parameters of the plate increase with increasing subgrade reaction modulus of the subsoil.
- The frequency parameters of the plate decrease with increasing thickness/plate ratio for first three frequency parameters but in general, the frequency parameters increase with increasing thickness/span ratio after 3rd frequency parameters.

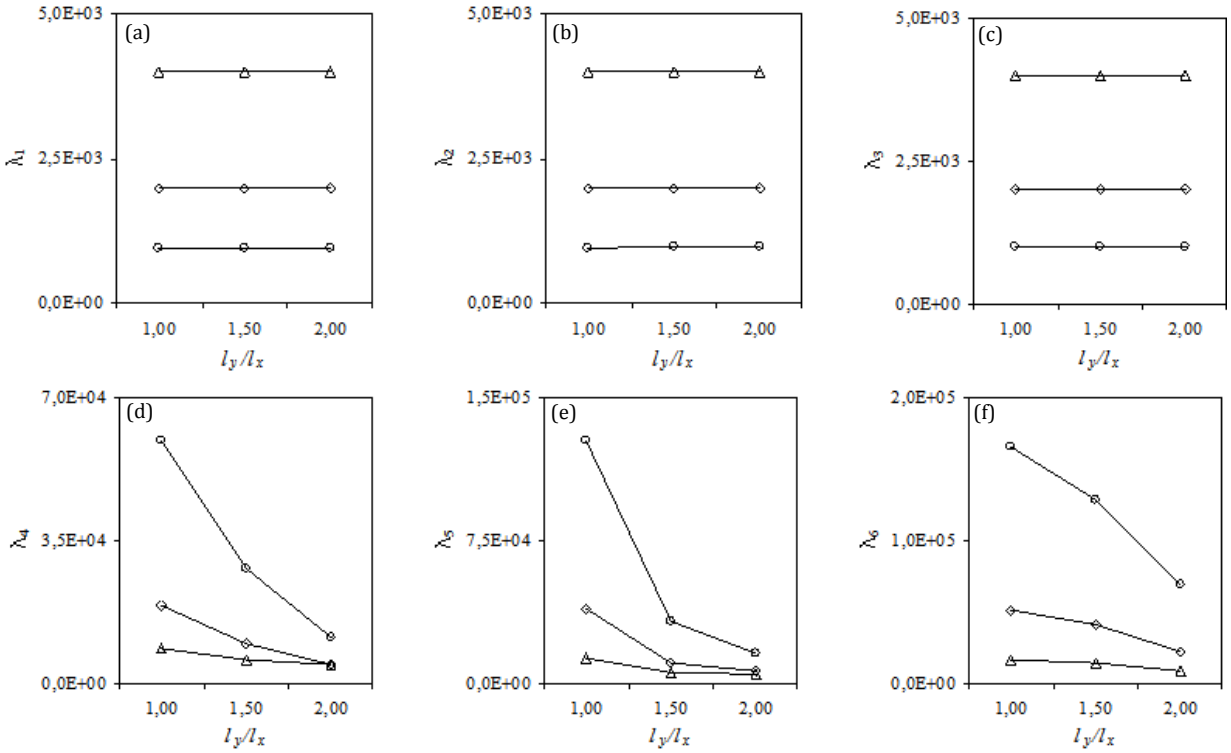

Fig. 2. The variation of the first six frequency parameters of the plate with various values of aspect ratio for k=5000 kN/m^3 (–Δ–, h/l_x =0.05; –◊–, h/l_x =0.10; –o–, h/l_x =0.20).

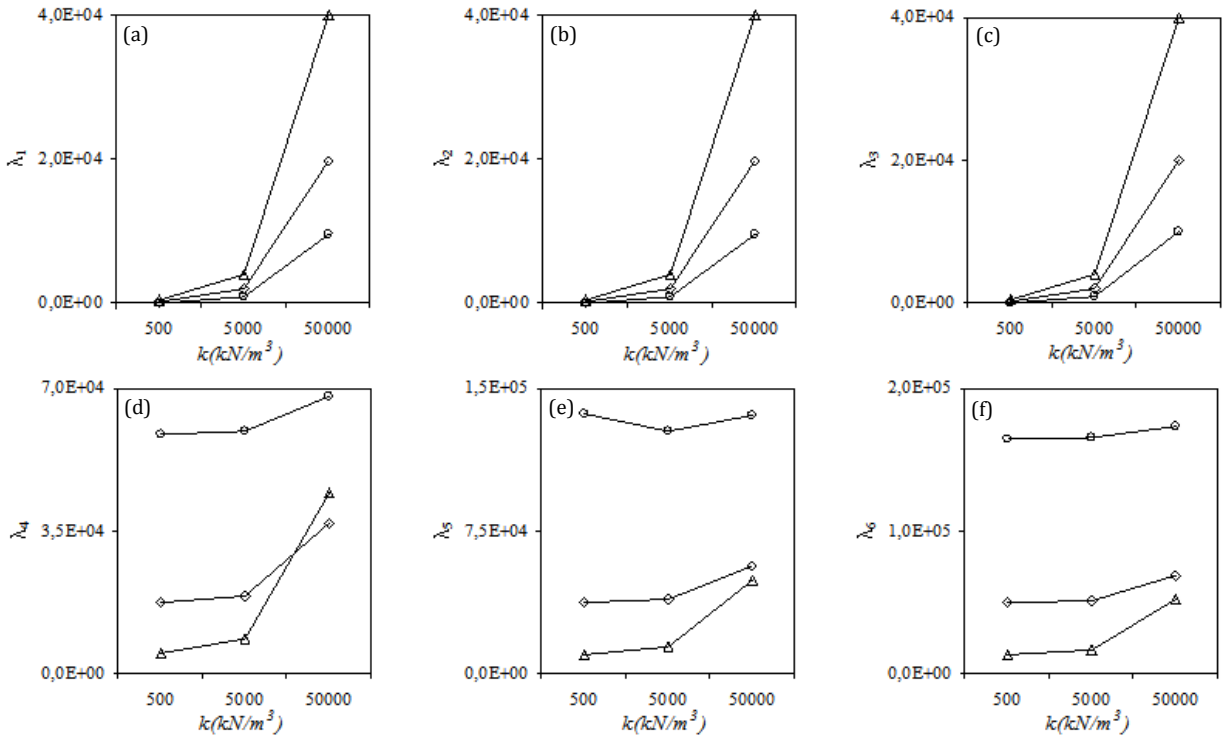

Fig. 3. The variation of the first six frequency parameters of the plate with various values of subgrade reaction modulus for aspect ratio=1.0 (–Δ–, h/l_x =0.05; –◊–, h/l_x =0.10; –o–, h/l_x =0.20).

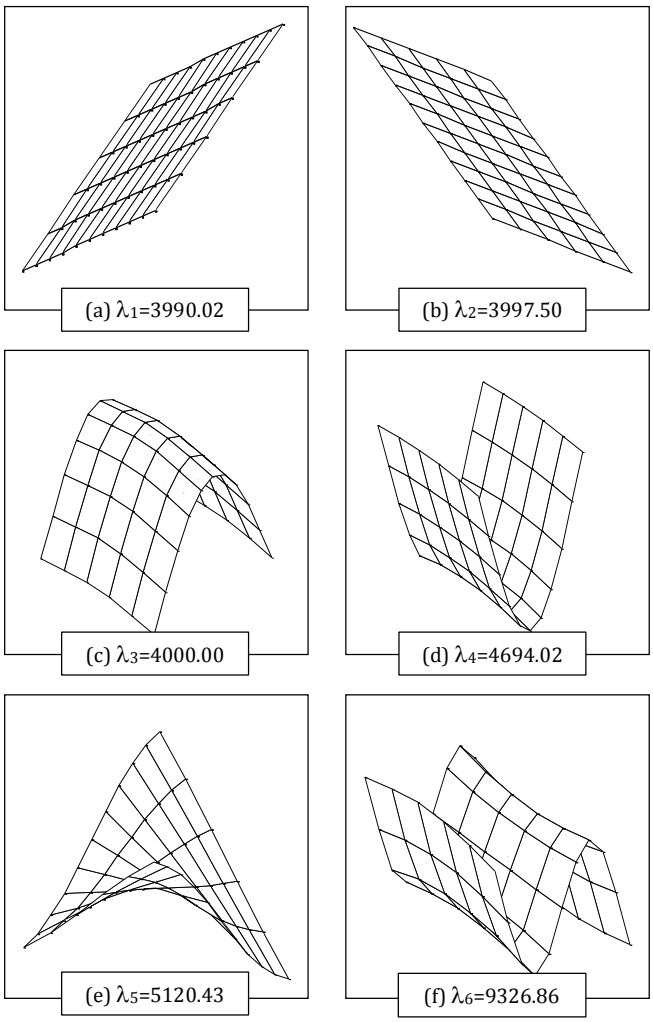

Fig. 4. First six mode shape for k=5000 kN/m^3, l_y/l_x=2.0 and h/l_x=0.05.

REFERENCES

Hsu MH (2010). Vibration analysis of orthotropic rectangular plates on elastic foundations. *Composite Structures*, 92, 844-852.

Jedrysiak J (2003). Free vibration of thin periodic plates interacting with an elastic periodic foundation. *International Journal of Mechanical Sciences*, 45, 1411-1428.

Kolar V, Nemec I (1989). Modelling of Soil Structures Interaction. Elsevier, Amsterdam.

Leung AYT, Zhu B (2005). Transverse vibration of Mindlin plates on two parameter foundations by analytical trapezoidal p-elements. *Journal of Engineering Mechanics*, 131(11), 1140-1145.

Malekzadeh P (2009). Three-dimensional free vibration analysis of thick functionally graded plates on elastic foundations. *Composite Structures*, 89, 367-373.

Omurtag MH, Özütok A, Aköz AY, Özçelikörs Y (1997). Free vibration analysis of Kirchhoff plates resting on elastic foundation by mixed finite element formulation based on Gateaux differential. *International Journal for Numerical Methods in Engineering*, 40, 295-317.

Özgan K, Daloğlu AT (2007). Alternative plate finite elements for the analysis of thick plates on elastic foundations. *Structural Engineering Mechanics*, 1, 69-86.

Özgan K, Daloğlu AT (2009). Application of the modified Vlasov model to the free vibration analysis of thick plates resting on elastic foundations. *Shock and Vibration*, 16, 439-454.

Shen HS, Yang J, Zhang L (2001). Free and forced vibration of Reissner-Mindlin plates with free edges resting on elastic foundations. *Journal of Sound and Vibrations*, 244(2), 299-320.

Tovstik PYe (2009). The vibration and stability of a prestressed plate on elastic foundation. *Journal of Applied Mathematics and Mechanics*, 73, 77-87.

Weaver W, Johnston PR (1984). Finite Elements for Structural Analysis. Prentice-Hall Inc., Englewood Cliffs. NJ.

Zhong Y, Yin JH (2008). Free vibration analysis of a plate on foundation with completely free boundary by finite integral transform method. *Mechanics Research Communications*, 35, 268-275.

Zhou D, Lo SH, Au FTK (2006). Three-dimensional free vibration of thick circular plates on Pasternak foundation. *Journal of Sound and Vibration*, 292, 726-741.

Challenge Journal of Structural Mechanics

Vertical displacement of collapsed bridge in Palau

Sıddık Şener [a,*], Yasin Çağlar [b], Mehmet Akif Benzer [c], Kadir Can Şener [d]

[a] *Department of Civil Engineering, İstanbul Bilgi University, 34060 İstanbul, Turkey*
[b] *Department of Civil Engineering, Kırıkkale University, 71451 Kırıkkale, Turkey*
[c] *3DM Engineering & Consulting Co., 03200 Afyonkarahisar, Turkey*
[d] *Department of Civil Engineering, Purdue University, Indiana 47907-2045, USA*

ABSTRACT

Vertical displacement of the Korror-Babeldaop (KB) Bridge in Palau is presented. This bridge was built in 1977 by the cantilever method and collapsed 3 months after remedial prestressing in 1996. KB Bridge was a segmental prestressed concrete girder having the world record of 241 m and maximum girder depth of 14.17 m. The final mid-span deflection was in design expected to be 0.53 to 0.65 m but after 18 years it reached 1.39 m and was still increasing. With a very limited amount of official information of the bridge was available and bridge was analyzed by ANSYS finite element program. Presented is an accurate analysis using 5392 hexahedral three-dimensional (3D) finite elements with 9614 nodes by ANSYS. Hognestad concrete model and Solid 65 element type were considered. The actual vertical displacements of free end of the cantilever bridge under truck loading were compared with the 3D finite element analyses results in order to come up with a benchmark model. The collapse reasons of KB Bridge were discussed.

ARTICLE INFO

Article history:
Received 14 May 2015
Accepted 17 June 2015

Keywords:
Bridge
Collapse
Post-tension
Concrete
Palau

1. Introduction

The collapse of a record 240.8m long clear-span prestressed-concrete bridge after being in service for 18 years, in the Pacific island nation of Palau, occurred without any failure indications in 1996. Koror-Babeldaob Bridge was connecting Koror, Babeldaob Islands. The failure of the KB Bridge in Fig.1, occurred on 26 September 1996, at around 5.45 afternoons (Burgoyne and Scantlebury, 2006). The collapse of record span bridge (Yee, 1979) was catastrophic, killing two people and injuring four more, and occurred under virtually no traffic load during benign weather conditions. Services passing through the bridge between the country's two most populated islands were severed; this caused the government to declare a state of national emergency and request international aid for the thousands of people left without fresh water or electricity.

The main span was flanked by 72.2 m long end spans in which the box girder was partially filled with rock ballast to balance the moment at the main pier. The total length of the bridge was 386 m (Fig. 1). The thickness of the bottom slab varied from 1.15 m at the main piers to 0.18 m at the span. The web thickness of bridge was 0.36m in the main span. The cross section and hinge are shown in Fig. 2.

The two symmetric concrete box cantilevers that formed the main center span were each constructed simultaneously by 25 cast-in-place segmental section (Şener, 2006) 3.66 m depth at the mid-span hinges and 14.17 m deep over the main piers. The whole bridge was completed within in 2 years. There are so many researches on the reason of collapse of Palau Bridge going on (Bazant et al., 2009; McDonald et al., 2004; Pilz, 1997; Şener et al., 2009; Benzer, 2011).

The present study was undertaken to ascertain whether there is something fundamentally wrong with the way prestressed concrete is understood and in particular whether it should be thought differently in the light of what happened.

* *Corresponding author*. Tel.: +90-212-3117376 ; Fax: +90-212-4278270 ; E-mail address: siddik.sener@bilgi.edu.tr (S. Şener)
ISSN: 2149-8024 / DOI: http://dx.doi.org/10.20528/cjsmec.2015.06.016

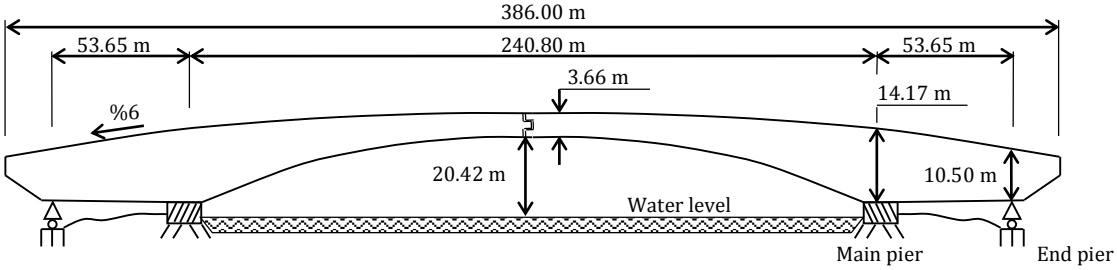

Fig. 1. Elevation of bridge geometry.

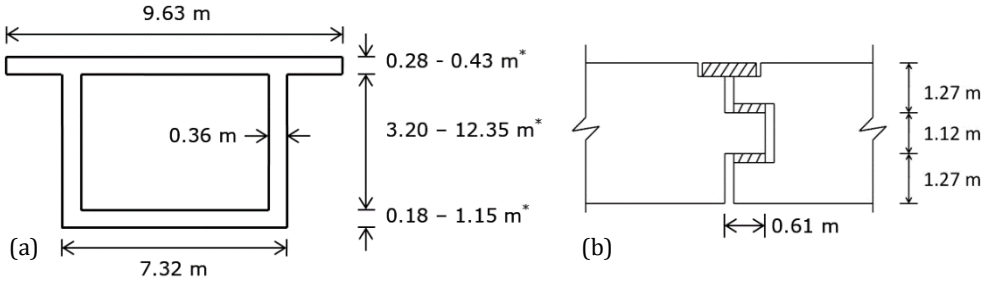

Fig. 2. a) Cross section of box girder at main pier, and b) hinge at the center of mid span.

2. Research Significance

Clarification of the causes of major disaster has been, and will always be, the main route to progress in structural engineering. Understanding of the excessive deflections of the bridge in Palau has the potential of greatly improving the predictions of creep and shrinkage effects in bridges as well as other structures.

3. Bridge Descriptions

According to design, the initial total longitudinal prestressing force above the main pier was 182.4 MN (≈0.70×316×812×1050 N), and was provided by 316 parallel high-strength threaded bars of diameter 32 mm and strength 1050 MPa (Fig. 3). Effective prestress was assumed as a f_{ef}=0.7f_y. The mass density of concrete was ρ=23.25 kN/m^3. Top slab covered by concrete pavement of average thickness 75mm. The aggregate was crushed basalt rock of maximum aggregate size about 19 mm, supplied from a quarry on the island of Malakal. The bars (the ducts of diameter 47.6 mm, later injected by grout) were placed in up to four layers within the top slab. Extended by couplers and anchored near the abutment, the prestressing bars had the diameter 32 mm and run continuously up to the segment of the main span at which the threaded ends were anchored by nuts. Threaded bars lengths in longitudinal direction were changing from 1.6 m to 18.3 m (7 different length).

From the fact that the erection took about 6 month, it is inferred that each fresh front segment was about 7 days old when prestressed. Generally tendons lengths less than 80 m were stressed from one end, longer than 80m were stressed from both. Threaded bars, of diameter 32 mm, and length 9.14 m were used to provide vertical prestress of the webs (spacing from 0.3 m to 3 m) and horizontal transverse prestress of the top slab (typical spacing is 0.56 m). The Young`s modulus of prestressing steel was assumed as 210 GPa and Poisson`s ratio as 0.3. In post-collapse examination, neither the prestressed nor the unprestressed steel showed and signs of corrosion, despite the tropical marine environment.

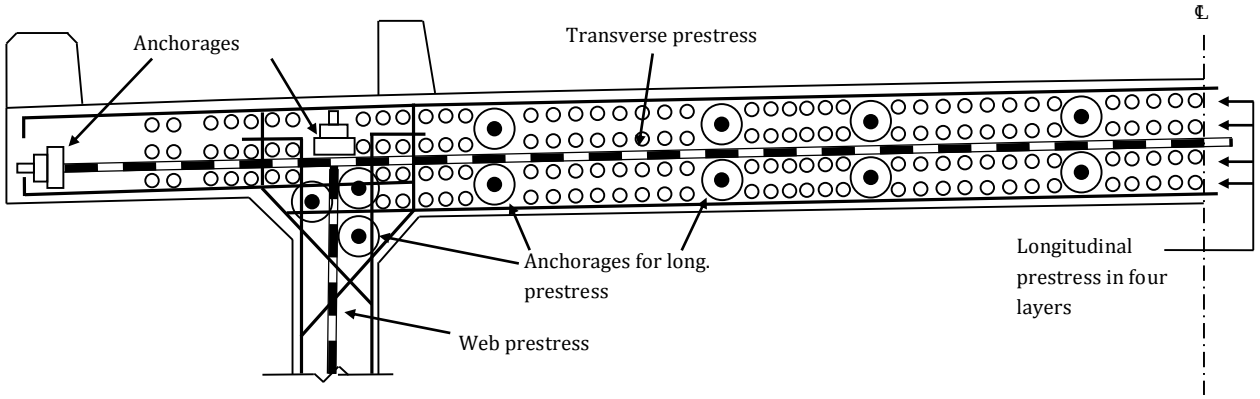

Fig. 3. Detail of top flange reinforcement.

The bridge was completed in April 1977, after which it remained unchanged for the next 18 years. On the period the cantilevers deflected due to creep, shrinkage and prestress loss. By 1990 the sag of the centre line, is shown in Fig. 4, had reached 1.2 m (Klein, 2007) affecting the appearance of the bridge causing discomfort to road users, and damage to the wearing surface.

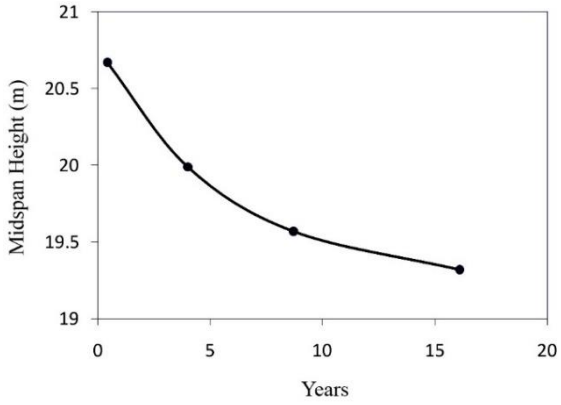

Fig. 4. Measured long-term deflection at midspan.

The detailed geometry of one half of the structure is shown in Fig. 5. The *x*-coordinate used here is measured from the extreme back of bridge, with rear support at *x*=18.6 m, and the main support at 72.25 m. This leaves a cantilever of 120.4 m. Variation of centroid location is also shown as dashed curve.

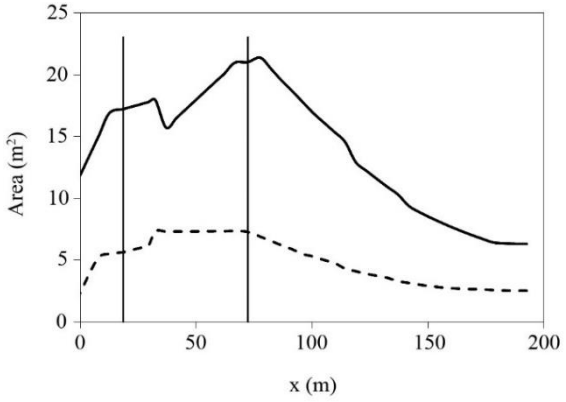

Fig. 5. Cross-sections along the bridge.

Variation of moment of inertia of the bridge was given in Fig. 6. In this figure average moment of inertia *I*=160 m⁴ was given as dashed line.

4. Cantilever Bridge

Fig. 7 shows that the as-built bending moment and shear force diagram due to the bridge's self-weight for one cantilever as a solid line. The plotted values included the effect of the ballast in the back span and weight of pavement since these are permanent load. The peak moment at the main support is 1893 MNm while at *x*=84.8 m the moment is 1418 MNm (Fig. 7(a)) and the shear force 32.0 MN (Fig. 7(b)).

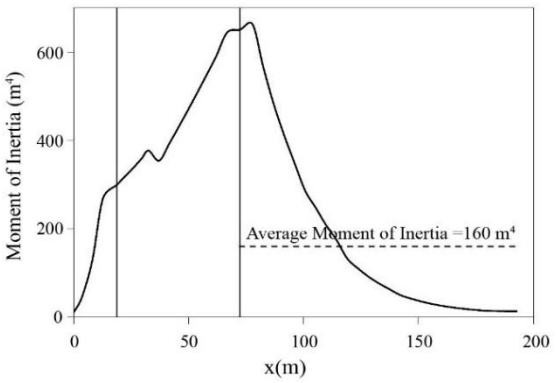

Fig. 6. Moment of inertia of the bridge.

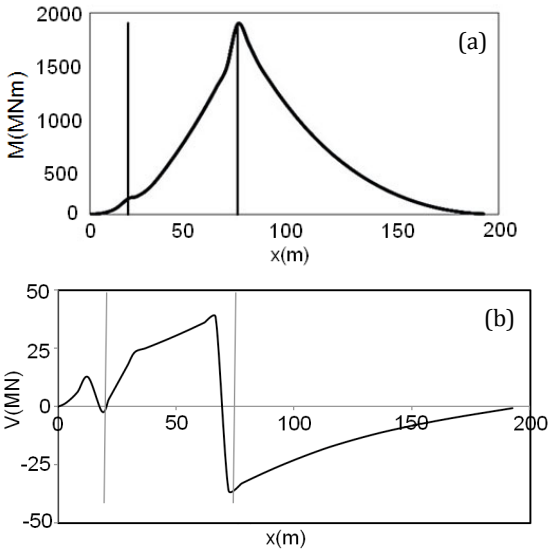

Fig. 7. Under the dead weight including ballast and pavement, a) bending moment, b) shear force diagram.

Box girders have been analyzed according to the classical engineering theory of bending in which the cross sections are assumed to remain plane. In Fig. 8, ANSYS finite element modeling is shown. In this simulation of bridge with ANSYS using 5392 hexahedral three-dimensional (3D) finite element with 9614 nodes were used. For threaded bars, 1014 line element by using node numbers in each 45 segments were used. In this section regular reinforcement ratio of the reinforced concrete was chosen as ρ=0.003.

As part of the assessment of the bridge a loaded truck weighting 125 kN was driven on the tip of each cantilever to determine its stiffness. Displacement at the tip of cantilever under the self-weight, pavement weight including ballast and prestress was give 127.83 mm, own weight, pavement, ballast, prestress under truck loading give 157.43 mm. Difference between these two displacements 29.6 mm is close enough to 30.5 mm, which is given in McDonald et al. (2004). In this case concrete model is close enough to real concrete used at Palau Bridge in vertical deflection.

KB bridge was collapsed under shear force at *x*=7.08 m far from the main pier face. For this reason stress distribution at *x*=7.08 m was important for this analysis. In Fig. 9 the distribution of shear stress in a cross section

located at 7.08 m away from main pier face, is shown when only self-weight or only prestress is considered. It can be seen that a significant shear stress exists in the top and bottom slabs near main pier.

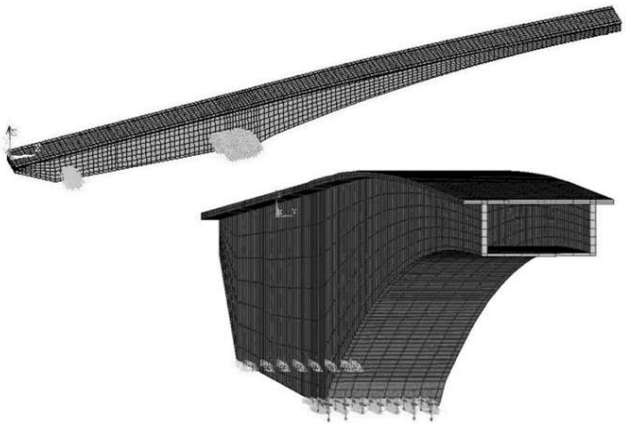

Fig. 8. Finite element mesh generation and boundary conditions of the model.

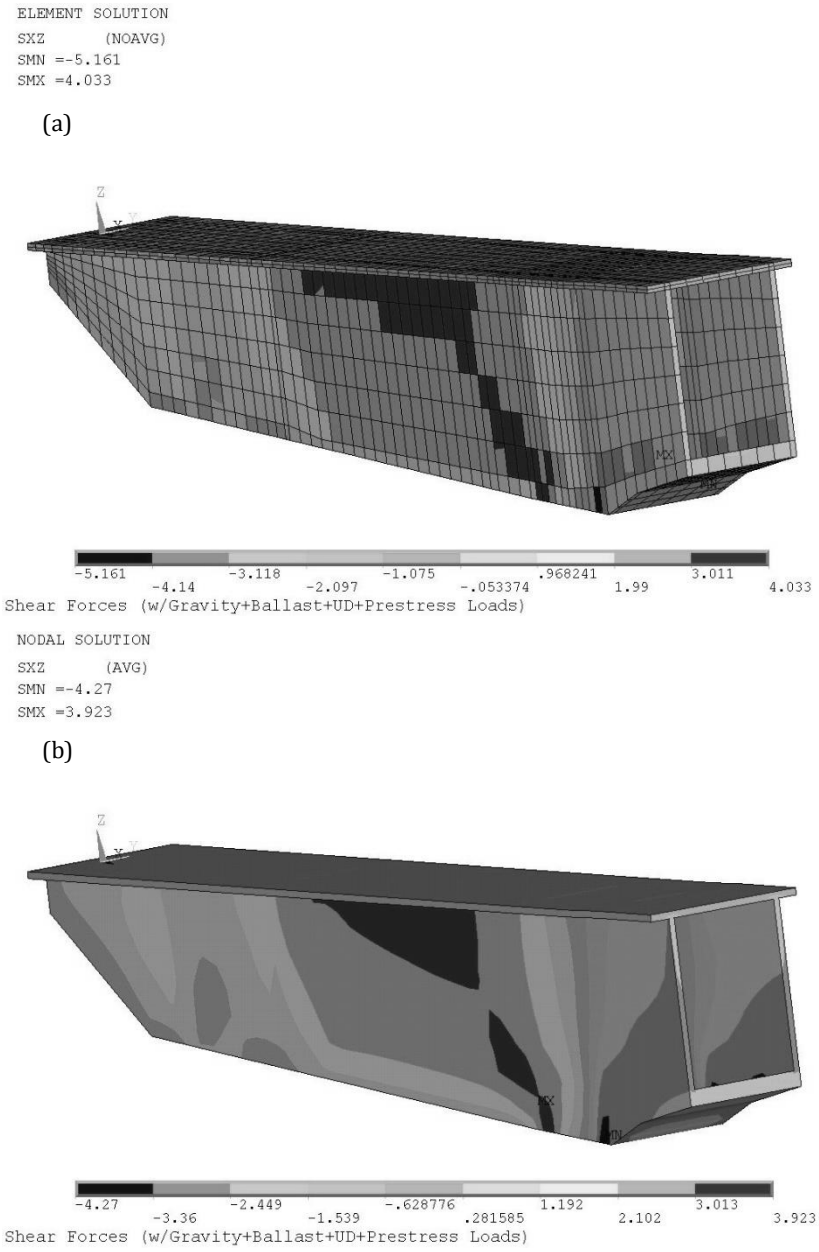

Fig. 9. Shear stress distribution at *x*=7.08 m under self-weight and prestress, a) element solution, b) nodal solution.

The total deflection is sensitive because it represents a small difference of two large numbers corresponding to self-weight and to prestress. The shear force plays a more important role in downward deflection by self-weight than upward deflection by prestress. Therefore the neglect of shear may lead to a considerable underestimation of the long-term deflection.

5. Repairing

At the results of unexpected deflection at midspan, the government of Palau is decided to take bridge repairing program. The continuity cables pass along the full length of the structure, which had been made continuous. They make contact with the concrete only at the anchorages and at the deflector beams. U.S. company made truck tests at midspan to measure the stiffness of the bridge. Under the 250kN truck loading, they measured the vertical displacement as a δ=30.5 mm. Vertical displacement at the bridge midspan, under the truck loading at the cantilever end, could be obtained from Eq. (1) as well.

$$\delta = PL^3/3EI \tag{1}$$

where, δ=vertical displacement, P=concentrated truck loading, L=length of cantilever, EI=stiffness of box section bridge. By using the measured displacement δ=0.0305 m under the truck loading (P=250 kN), in Eq. (1), EI=250×120.4^3/(3×0.0305)=4.76×10^3 Nm^2 will be obtained. By the help of stiffness and I value from the Fig. 6, elasticity modulus of concrete was found as, E=4.76×10^3/160=29.8 GPa.

During the repairing process, for lifting of bridge at center, help of additional prestressing bars applied 36 MN force. Assume the lever arm of prestressing bars as a 3 m, taking M=36×3=108 MNm, and using Eq. (2),

$$\delta = ML^2/2EI\,, \tag{2}$$

displacement at the cantilever end under the M, δ=108×10^6×120.4^2/(2×4.76×10^{12})=0.16 m was obtained. The vertical and horizontal component of forces exerted by the cable, which is shown with dashed line on the bridge, is given in Fig. 10. Required M for the total displacement δ=1.61 m, was found by using Eq. (1) as M=1.61×2×29.8×10^3×160/120.4^2=1059 MNm. To prevent the prestress loss in bars which already build in the cross section, 20% is enough for displacement, and taking the lever arm 2 m, cantilever end moment M=0.2×182.4×2=73 MNm was obtained. By this way, δ=73×1.61/1059=0.11 m vertical displacement, will be eliminated.

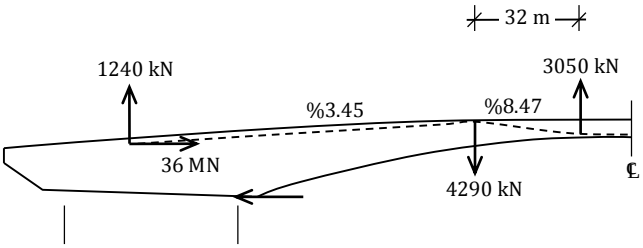

Fig. 10. Forces induced by continuity cables.

Second work, to get the deformation of bridge at center back, horizontally embedded 8 flat jacks were installed between the two cantilevers which were jacked apart with a force of 31 MN applied at the center of the top flange at shown in Fig. 11. For the jacking force, by using slope of road 6%, and center of gravity at x=86 m was 5.9 m, lever arm will be 0.06×70+5.9=10.10 m. Under the M=3×10.10=313 MNm, vertical displacement, δ=313×10^6×120.4^2/(2×4.76×10^{12})=0.48 m, totally δ=0.64 m will be compensated during the repairing of the bridge.

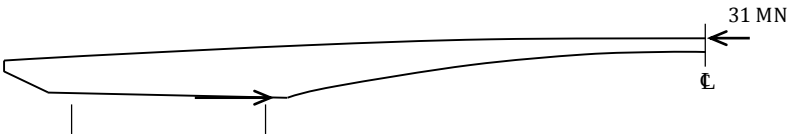

Fig. 11. Forces due to flat jacks at center.

Note that there is no force applied to the bridge at the centerline since the tendon does not touch the concrete here. Each side of the main span was prestressed, with a total of 182.4MN of force anchored in the back span between the piers. The other ends of the bars were anchored throughout the main span, at the ends of the 25 segments that made up each cantilever (Fig. 12). In this way a smaller force was applied at the center than at the piers, where a larger moment was experienced. This will be referred to as the original prestress to distinguish it from subsequent additions.

Due to the change in cable profile a prestressing tendon exerts forces on the concrete all along. Its length so the moments in a function of the eccentricity at any position, but the force applied by a jack directly on the concrete retains its line of action throughout the structure. The difference in height between the center of the top flange at the tip, and the centroid at x=84.8 m is 10.23 m.

6. Discussion

A downward deflection of 30.5 mm was recorded at a midspan when two 125 kN trucks were parked on each side of the midspan hinge. The main goal in this study to compare the results of finite element code based on model Hognestat which give the same deflection as 29.6 mm under the load of 250 kN. The displacement at the midspan of bridge was found close enough to the ANSYS finite element results.

Continuous bridge like as Turkish record holder Beylerderesi and Gülburnu Bridge by symmetric cantilever length is 82.5 m (Çelebi and Harputoğlu, 2006, Harputoğlu et al., 2007), better than the cantilever bridge for the time dependent midspan deflection.

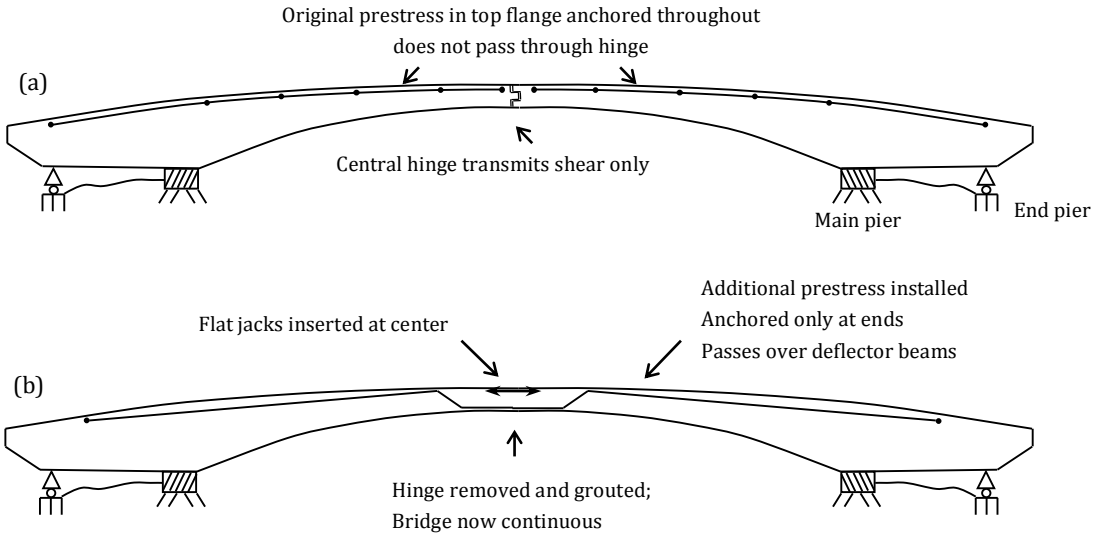

Fig. 12. a) Original bridge in April 1977, b) alterations made in July 1996.

7. Conclusions

As a result of this study following points were predicted.

- Cross section was always remaining constant during the repairing work, using additional continuity cables and flat jacks increase the amount of reinforcement may cause overreinforced concrete beams.
- Temperature effect is also important in tropical environment. Top face of bridge is always under the sun light with crack around 50°C, but water face is always in compression, no sunlight and temperature around 20°C without crack. This difference increases the drying effect. According to one study (Bazant et al., 1987), weight loss was in the C beam with about 70mm crack length, 2.2 times more than the without cracked C beam.
- The additional complications, caused by changing the structure of bridge from statically determinate cantilevers to a statically indeterminate beam may cause problem. Because cantilever beams are originally cantilevers when the transfer to the continuous beam does not have any continuity bar except additional continuous cables inserted during the retrofit.
- Creep (Bazant, 1972) lead to dangerous deflection and prestress loss should be investigated.

REFERENCES

Bazant ZP (1972). Prediction of concrete creep effects using age-adjusted effective modulus method. *ACI Journal,* 69, 212-217.

Bazant ZP, Li GH, Yu Q, Klein G, Kristek V (2009). Explanation of excessive long-time deflections of collapsed record-span box girder bridge in Palau. *Preliminary Structural Engineering Report*, 08-09/A222e, Northwestern University, Evanston, Illinois, USA.

Bazant ZP, Şener S, Kim JK (1987). Effect of cracking on drying permeability and diffusivity of concrete. *ACI Materials Journal*, 84, 351-357.

Benzer MA (2011). A Study of the Collapse Mechanism of Korror-Babelthuap Bridge with Finite Element Model. *M.Sc. thesis*, Gazi University, Ankara, Turkey.

Burgoyne C, Scantlebury R (2006). Why did Palau Bridge collapse?. *Structural Engineer*, 84(11), 30-37.

Çelebi N, Harputoğlu Z (2006). Gülburnu Bridge. *Bulletin of Yuksel Proje*, 7(10), 8-9 (in Turkish).

Harputoğlu Z, Çelebi N, Tulumtaş F (2007). Gülburnu Bridge. *IMO Symposium of Bridge and Viaducts*, 67-79, Antalya, Turkey (in Turkish).

Klein G (2007). Collapse of the Korror-Babeldaob Bridge. *ACBM Report*, Northwestern University, Evanston, Illinois, USA.

McDonald B, Saraf V, Ross B (2004). A spectacular collapse: The Korror-Babeldaob (Palau) balanced cantilever prestressed post-tensioned bridge. *Indian Concrete Journal*, 77(3), 955-962.

Pilz M (1997). The collapse of the K-B Bridge in 1996. *A M.Sc. Dissertation at the Imperial College London*, Lacer, 2, 43-52.

Şener S (2006). Prestressed Concrete, *Alp,* Ankara, Turkey (in Turkish).

Şener S, Çağlar Y, Şener KC (2009). Collapse reasons of the Palau Bridge. *Seminar of RC Structures*, BYS2009, October 21, 63-72, Istanbul, Turkey.

Yee AA (1979). Record span box girder bridge Connects Pacific Islands. *Concrete International*, 22-25.

Challenge Journal of Structural Mechanics

The research of the behavior of the rigidity connections between columns in industrial buildings under the influence of temperature variation, earthquake and wind

Cemal Eyyubov *, Şükran Genç, Canan Yılmaz

Department of Civil Engineering, Erciyes University, 38039 Kayseri, Turkey

ABSTRACT

In this study, there are the research results of the stress conditions under the influence of temperature variations in rigidity shear members between columns having different constructive formations. Here, the connections are conveyed that characterize the variation of internal forces resulting from temperature variations in rigidity shear members related to the length and height of the structural system. Principles are investigated in order to be able to calculate the earthquake and wind loads of rigidity shear by taking the combinations with the loads resulting from the temperature variation into consideration.

ARTICLE INFO

Article history:
Received 15 May 2015
Accepted 13 June 2015

Keywords:
Rigidity connections
Rigidity shear
Temperature variation
Temperature deformations
Internal forces

1. Introduction

Engineering investigations of Buhara (1976), Erzincan (1992), Adana (1998), Marmara (1999), Düzce (1999) and other destructive earthquakes have suggested that great deformations and ruptures are observed during the earthquake in the rigidity connection members between columns. Engineering investigations into the effect of destructive earthquakes on buildings and engineering structures also point out that buildings which are designed and constructed without considering the rigidity connections between columns widely collapse during the earthquake. In these buildings, because of excessive horizontal and vertical deformations, it is often observed that damages, which may cause the stoppage of using the buildings such as leaving of filling walls, bending of ray beams under crane, breaking and spoiling on rays-joist joints, blister and big detachments on the roof coating (Eyyubov, 1978; Eyyubov, 1988; Eyyubov, 2004).

Rigidity connections between beams must be able to provide the necessary rigidity towards the longitudinally use conditions of buildings. Rigidity connections must receive the force forming from the working of bridged cranes in industrial buildings, from the effect of wind, earthquake, from the failure of basic grounds which is not uniform, from the climate changes and from the temperature variations due to hot technical applications and must have the capacity for transferring them to the base of the building.

Exhausting of rigidity connections between columns because of the long lasting temperature variations, investigation of the endurance from the dynamic effect of the loads forming from the working of cranes and wind and preparation of calculation methods which can be applied in the building planning practice related to its conclusions are the current problems. Furthermore, the behavior of the carrying system of the building depends on the characteristic of the settlement of rigidity connections on its length.

Formation of rigidity struts between columns, constructive formation of columns, their joints and sections determine to a great deal the behaviour of rigidity shear walls as a whole. It is enough to design for tension of the sections of both two diagonal struts in the model which provides the other diagonal cover with elastic buckling, a diagonal towing of rigidity shear bars (Belenya, 1985; Melnikov, 1980). There are rigidity shear wall construction practices that use bars, which are described as

* *Corresponding author*. Tel.: +90-352-2076666 ; Fax: +90-352-4375784 ; E-mail address: ceyyubov@erciyes.edu.tr (C. Eyyubov)
ISSN: 2149-8024 / DOI: http://dx.doi.org/10.20528/cjsmec.2015.06.014

"buckling prevented" (Karataş and Çelik, 2009; Melnikov, 1980; Wakabayashi et al., 1973; Xie, 2005). In this paper, characteristics of inner force determination, which is formed by the effects of seasonal heat changes in these bars will be given regardless of the formational characteristics of the joint and sections.

Research results on the calculation of the internal forces occurring in the rigidity shear members depending on the length and the height of the building, and also optimal formations' arrangement of the settlement of the rigidity shears between columns in industrial structural system have been stated here.

2. Selection of the Research Method

Researches have been carried out suitably to two-type formations of the rigidity shears in structural system. In the first type formation, rigidity shear was placed in the middle of the building in structural system (Figs. 1, 3, 5), as for second type formation, it was placed at two sides of it (Figs. 2, 4 and 6) (Arda and Uzgider, 1978; Belenya, 1985). Stress condition of the building rigidity shear was also analyzed independently of the structural system. On each type of arrangement, structural system which was 66 m, 78 m, 90 m, 102 m, 114 m, and 126 m in length was analyzed. On these lengths, conditions in which the structural system was 6 m, 12 m and 18 m in height were taken as an analysis object. In cases where these structural system models (t_2-t_1) taken into consideration for analysis were 30°C, 40°C, 50°C and 60°C, rates of internal forces were calculated in rigidity shear members and columns placed in edge-side sections related to the length of the building.

Here, t_1 is the average seasonal temperature when the building was constructed; t_2 is maximum temperature affecting the structural system during the usage of it. Calculations were made by using the SAP2000 program. By this way, variation character of internal forces depending on the length, height and t_2-t_1 rates of the building in its side columns and rigidity shear members was investigated.

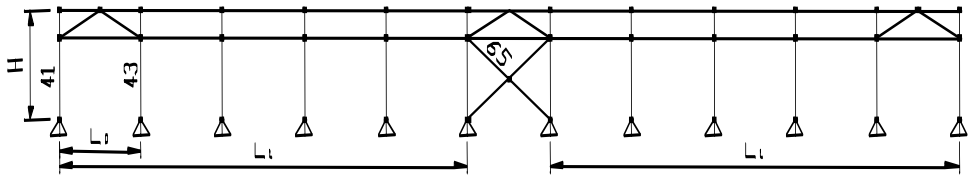

Fig. 1. Type-1 (H = 6 m).

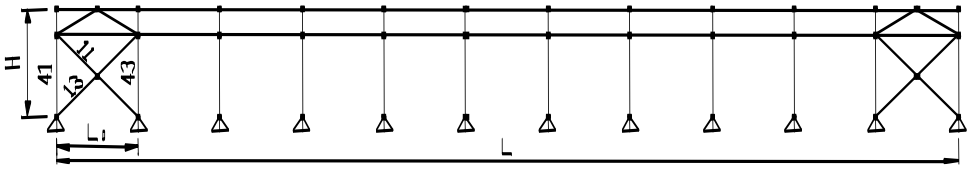

Fig. 2. Type-2 (H = 6 m).

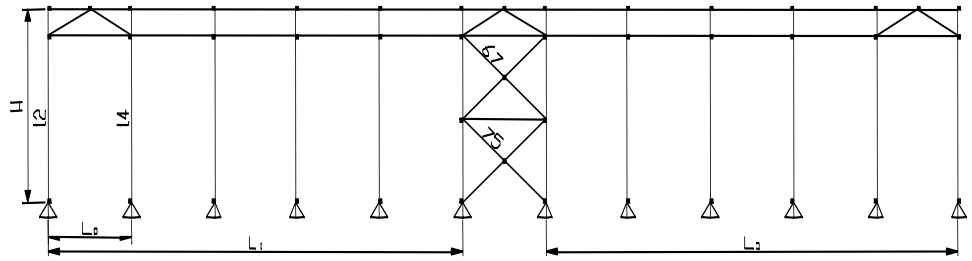

Fig. 3. Type-1 (H = 12 m).

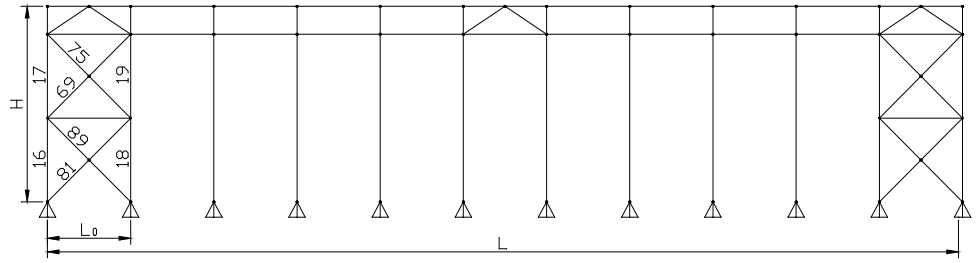

Fig. 4. Type-2 (H = 12 m).

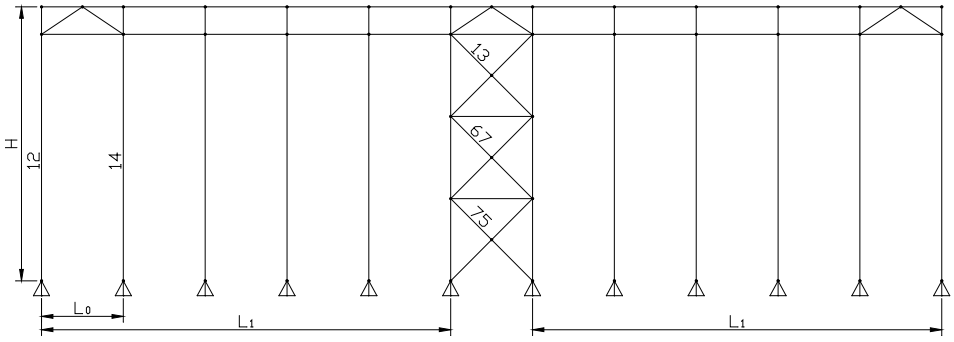

Fig. 5. Type-1 (H = 18 m).

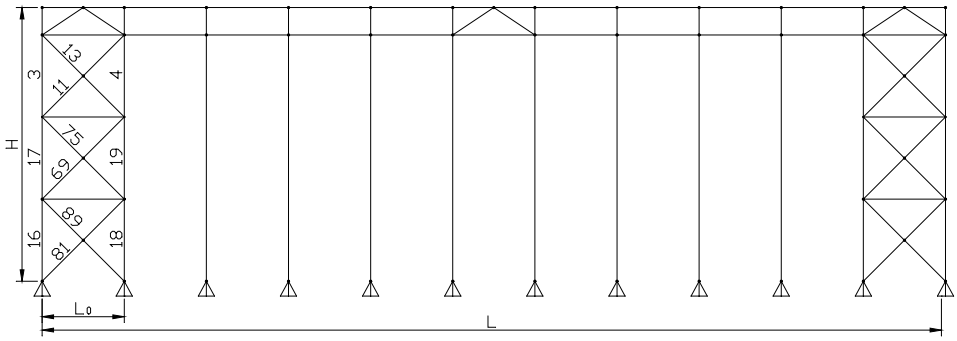

Fig. 6. Type-2 (H = 18 m).

3. Determination of Displacement and Forces Resulting from the Effect of the Temperature Variation in Rigidity Shear between Columns

Strain of the structural system due to the effect of temperature variation and the rate of the effective loads depend on the arrangement of the structural system. In the first type arrangement of structural system, horizontal strain rate suitable to high level of the structural system's side columns can be calculated with

$$\Delta_t = \alpha L_1 (t_2 - t_1)\,. \tag{1}$$

Here, α is the linear expansion modulus of structural system material. It can be taken as 12x10^{-6} for steel. L_1 is the width from rigidity shear side column in structural system to building side column.

As for the second type arrangement of structural system, due to the length of structural system, when rigidity shear of both sides is taken into consideration as it is shown in Fig. 2, a strain limitation close to $\Delta_t \rightarrow 0$ is at issue. In this case, effective load rate in the high level of the column to the each of the side shears can be calculated with the

$$F_{tkp} = \frac{3EJ\alpha L_0}{H^3 c}(t_2 - t_1)\,. \tag{2}$$

Here, E column material elasticity modulus- can be taken as E = 2,06·10^4 kN/cm^2 for steel. H is the height of column and L_0 is the distance between the internal columns of shear in Fig. 2 in the length of structural system. c will be calculated with

$$c = 1 + (\alpha_1)^3 \mu\,, \tag{3}$$

in variable sectional columns in terms of height. $\alpha_1 = H_y/H$ and $\mu = J/J_y$ can be calculated with equations. H_y is the height of higher part of J_y column cross-section from the changed point and the inertia moment of sections appropriate to the same height. J is the column cross-sectional inertia moment in stable cross-sectional columns. As for variable sectional columns, the lower part of the column is cross-sectional inertia moment. When structural systems arranged with stable cross-sectional columns due to its height are applied, it will be taken as c = 1 in Eq. (2) (Belenya, 1985). Moreover, from the effect of the temperature variation of vertical rigidity shear itself, the load occurring towards the horizontal bar in the top part of its columns can be calculated with

$$F_{tp} = \frac{0.5AA_1E\alpha(t_2 - t_1)b}{H[A_1 + A(K_1 + 2.83)]}\,. \tag{4}$$

Here, it can be found with $K_1 = b/H$ equation. b is the distance between columns in rigidity shear. A is the column cross-sectional area, A_1 is the rigidity shear cross-sectional area of other columns.

In accordance with this research, in the first type structural system arrangement, effective load rate from the general temperature variation occurring in the height of the building to rigidity shear can be as $F_t \rightarrow 0$. But, in this case, load rate resulting from the effect of temperature in rigidity shear itself will be calculated with Eq. (4). As for the second type structural system arrangement, formation of rigidity shear to the two edge side of the building widely limits the horizontal strain under the

influence of temperature. In other words, $\Delta_t \rightarrow 0$ and horizontal load rate effective in rigidity shear can come closer to F_t maximum in this case (Timoshenko, 1955; Belenya, 1985). Also in this case; the total effect of power occurring due to the temperature variation in whole of the building height in rigidity shear and the power occurring due to the temperature variation in rigidity itself will take place. In this case again, effective load to building shear will be calculated with

$$F_t = F_{tkp} + F_{tp} . \quad (5)$$

When Eqs. (2) and (4) are taken into consideration in Eq. (5), it will be as

$$F_t = \frac{0.5E\alpha(t_2-t_1)}{H}\left[\frac{6Jl_0}{H^2c} + \frac{AA_1b}{A_1+A(K_1+2.83)}\right] . \quad (6)$$

4. The Calculation of Internal Forces under the Influence of Temperature Variation in Rigidity Shear Members between Columns

In structural system, rigidity shear members between columns having different geometrical characteristics, SAP2000 program was used during the determination of internal forces suitable to different temperature variations. According to this, when rigidity shear in a structural system which is at a height of 6 m and 66 m in length is arranged as type 1 and temperature variation is 30°C, normal force in side column (member no 41) is 0.055 kN; normal force in rigidity shear diagonals (member no 65) is -51.719; 0.184kN and 0 when shearing force is suitable; 1.102 kNm and 0 when bending moment is suitable. When the effect of temperature is 60°C in the same structural system, internal forces double. When the length of the structural system is taken as 78 m and 30°C temperature variation takes place in member no 41, normal force is 0.209 kN and it is -51.744 kN in member no 65. It is also taken as 0.216 kN and 0 when shearing force is suitable and bending moment as -1.297kN and 0. When the same building length is 90 m and temperature variation is 40°C, normal force is -0.629 kN in member no 41, 69.080 kN in member no 65; shearing force is taken as 0,332 kN ; 0, and bending moment as -1.989 kNm. When the building is at the height of 6 m, 12 m, 18 m and 66 m, 90 m and 126 m in length, calculation results of internal forces suitable to 40°C temperature variation are given in Table 1.

According to the rates given in this table, when the length of the building steps up to 126 m from 66 m, normal force rate suitable to 40°C temperature variation is 24 in member no 41, bending moment is 1.88, shearing force is 1.88. Normal force has increased 1.009 times in member no 65.

When the building is at a height of 6 m and 66 m in length (Fig. 2) and the rigidity shear is placed in two sides of the building (Type-2), internal force in 30°C temperature variation is -91.715 kN, +193.627 kN in internal column, 85.010 kN in tensile diagonal (member no 11) and -229.112 kN in stress diagonal. As for shearing force and bending moment rate, it is taken as little as to be disregarded. Under the influence of 60°C temperature variation in the same structural system , normal force is -183.429 kN in the side column of rigidity shear, 387.253 kN in internal column, 170.021 kN in tensile diagonal (member no 11), -458.225 kN in stress diagonal (member no 13). In this case also, shearing force and bending moment can be ignored. As for the temperature variation marked negatively, rates of internal forces in side and internal columns of rigidity shears are stable, but their markers will be reverse. According to the rates given in Table 1, when the length of the building increases from 66 m to 126 m, normal force rate suitable to 40°C temperature variation increases to 12.52 kN in side column, 11.32 kN in internal side column, 12.6 kN in tensile diagonal, 11.1 kN in stress diagonal.

When the length of the building is 126 m and temperature variation is 40°C, proportion of the normal forces of the members in a structural system formed according to Type-2 to normal forces of system members formed according to Type-1 is 87 in external side column and 4.88 in stress diagonal (member no 13).

Depending on the rates given in Table 1, when the length of the building is 66m and internal forces of rigidity shear members of the Type-1 and Type-2 formations are compared in 40°C temperature variation; rates of the formations according to Type-1 in proportion to the formations according to Type-2, normal force was seen to decrease 1675 times in left side column, 3536 times in internal side column and 4.43 times in stress diagonal.

Furthermore, when the length of the building was 66 m and temperature variation was 40°C, in Type-1 structural system model, normal force decreased 3.38 times in external side columns. This happened when the height was increased from 12 m to 18 m. As for Type-2, normal force increased 1.06 times in external side columns with the increase of height. A simplified method to determination of the inner force of stiffness brace in industrial buildings due to variation of temperature is proposed (Eyyubov, 2011).

Rates given in Table 1 of internal forces resulting from the temperature variation in the columns of building and rigidity shear members $\Delta_t = t_2 - t_1 = 40°C$ were calculated considering the seasonal temperature variation. This is because seasonal temperature variation widely seen in Turkey is close to 40°C. For the determination of internal forces forming in the building rigidity shear and columns due to desired temperature variation, that is enough to multiply the rates given in Table 1 with the K_t modulus (Eyyubov, 2010).

$$K_t = \Delta t_i / \Delta t_0 . \quad (7)$$

Here, Δt_i rate is the seasonal temperature variation rate in the region where the desired building is settled. It is determined with the statistical methods by depending on the meteorology service data and it is stated in the agreements prepared by Turkish Standards Institute (TSE). Δt_0 is the temperature variation reference value by which appropriate construction member is calculated. Here, Δt_0 will be taken as 40°C.

Variation diagram of internal force rate in building side columns depending on the length of the building and the height of Type-1 shear structural system is given in

Fig. 7. According to this, internal force rate forming in the members and columns of shear structural system changes linearly in accordance with the length of the building. Suitable rate of the internal force to the desired length of the building in the members and the columns of the shear can be found by multiplication of the rates given in Table 1 with the K_l modulus (Eyyubov, 2010).

$$K_l = l_i / l_0 \,. \tag{8}$$

Here, l_0 was calculated beforehand or is the distance from the shear side column of the building whose reference value have been given in Table 1 to the side column of the building, l_i is the same distance in the building whose design we have undertaken.

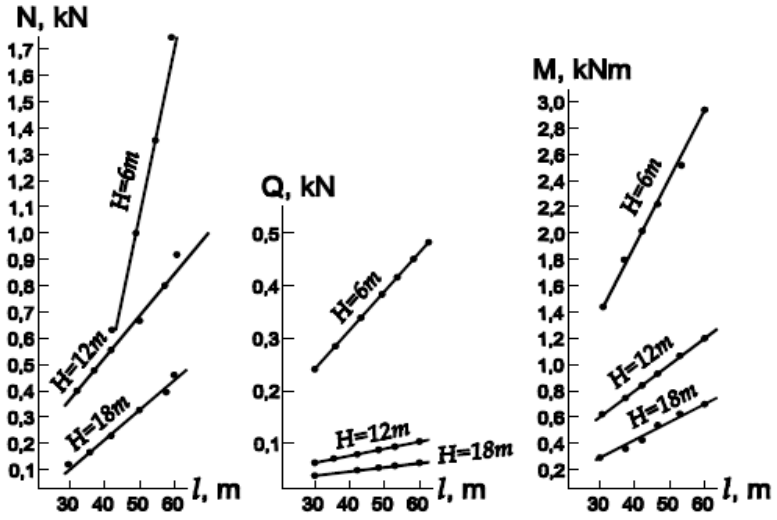

Fig. 7. Type-1: Variation diagram of internal force rates depending on building length and height in rigidity shear members.

Table 1. Internal forces in columns and rigidity shear members in the arrangement of structural system related to Type-1 and Type-2.

L (m)	INTERNAL FORCES	H	6 m				12 m							
		Element	41		65		12		14		67		75	
		Number	41	43	11	13	16	17	18	19	75	69	89	81
126	Axial Force (t)	Type 1	-0.1752		-6.9557		-0.0920		0.0920		1.3850		-7.0140	
		Type 2	-15.3066	29.2320	14,2587	-33.9493	-40.3658	-17.3049	45.5826	18.2136	18.5917	-19.8806	12.7286	-25.7599
	Shear Force (t)	Type 1	0.0461				0.0099		0.0089					
		Type 2	-0.0034	-0.0110			0.0096	-0.0176	-0.0183	0.0155				
	Bending Moment (tm)	Type 1	-0.2764				-0.1193		-0.1073					
		Type 2	0.0203	0.0660			-0.0576	0.0479	0.1095	0.0166				

L (m)	INTERNAL FORCES	H	18 m											
		Element	12			14			13		67		75	
		Number	16	17	3	18	19	4	13	11	75	69	89	81
126	Axial Force (t)	Type 1	-0.0473			0.0473			-0.2985.		1.4738		-7.0377	
		Type 2	-4S.6916	-34.6986	-11.8546	58,7577	32.1771	14.4663	12.4965.	-16.1918	16.1127	-12.5497	7.2365	-21.4698
	Shear Force (t)	Type 1	0.0039			0.0035								
		Type 2	0.0030	-0.0068	-0.0004	-0.0180	0.0191	-0.0048						
	Bending Moment (tm)	Type 1	-0.0704			-0.0634								
		Type 2	-0.0178	0.0227	0.0250	0.1081	-0.0064	0.0225						

The stiffness members which located between columns inner force values due to variation of temperature and building length are written as (Eyyubov, 2011);

$$N_{lt} = K_1 K_t l N_a \;,\; Q_{lt} = K_1 K_t Q_a \;,\; M_{lt} = K_1 K_t M_a \,. \tag{9}$$

K_l, K_t the coefficients can be calculated by (7) and (8). N_a, Q_a, M_a are reference values of axial force, shear force and bending moment respectively. They can be chosen according to reference building length (126 m) and reference temperature variation (Δt_a = 40°C) from Table 1 or the diagram giving in the Fig. 7.

The inner force values of the longitudinal exterior stiffness braces due to wind and earthquake effects can be calculated by relevant regulations.

Normal force rates forming in the crosswise of the rigidity shear can be applied in design depending on the length of the building, and it can be accepted as constant.

5. The Design of the Industrial Building Structural System Depending on the Temperature Variation

When rigidity connection system arranged longitudinally between columns in industrial buildings is formed in accordance with Type-2, wind affects the rigidity shears in two sides of the building. Moreover, internal forces forming from the effect of the wind then can be added.

The analysis of the rates given in Table 1 and diagram shows that temperature strains in all of the members of the rigidity shear are subject to the accumulation of it with the strains resulting from the effect of the wind and earthquake. Here, internal forces forming from the temperature variation always can be taken into consideration in the same combination with the one, two or three of the internal forces resulting from the effect of the wind, earthquake, machines or mechanisms when they are activated and stopped.

When the rigidity shear is placed in the middle of the building (Type-1), the rate of the internal forces resulting from the temperature variation in rigidity shear members can be ignored as it is low. Calculation will be made considering that in this case, the absorption effect and active stress of the wind will be countered by the single rigidity shear placed in the middle of the building length. The same approach will be adopted when the effect of earthquake is taken into consideration in the design of the building.

Thus, the placement of rigidity shear between columns into the middle of the building length may cause a decrease in the internal forces forming in the structural system members and simplification of the construction and the design of the building. For example, a rigidity shear instead of two rigidity shears can be placed into the building whose length reaches to 120 m. This provides a great economical benefit for industrial building construction.

6. Conclusions

The research results of the behaviors of the rigidity connections between columns in industrial buildings can be summarized as follows:

- The engineering research of the destructive earthquakes has showed that the behavior of the industrial buildings during an earthquake is based on the formation of the rigidity connections between columns. With twisting, breakage and deformations in joints in rigidity connection members can be encountered during an earthquake. These deformations forming in the rigidity shears affect the usage conditions of the buildings.
- The placement of the rigidity shear in the structural system into the middle of the building causes a decrease in the forces depending on temperature variation affecting the connection member and it also causes to the simplification in the formation of the structural system. The length of the industrial building depending on the temperature variation can be accepted as 100 m. In this case, it is offered that rigidity shear between columns should be placed in the middle of the building. Optimal rate of the distance of rigidity shear to the building sides can be 40 m~60 m.
- When the members of the industrial building structural system are dimensioned, it is required that the loads resulting from the temperature variation should be considered. The loads resulting from the temperature variation can be included in the load combinations as static loads.

REFERENCES

Arda TS, Uzgider E (1978). Çelik Çatı ve Binalarda Rüzgar Karşıt-Düzenleri ve Stabilite Bağları. Sakarya Devlet Mühendislik-Mimarlık Akademisi, İstanbul (in Turkish).

Belenya EI (1985). Metallicheskie Konstruktsii. YoYo Media, Moscow (in Russian).

Eyyubov C, Genç Ş, Yılmaz C (2010). Sanayi binalarında kolonlar arası bağlantıların davranışlarının araştırılması. *Yapı Dünyası Dergisi*, 170 (in Turkish).

Eyyubov C, Genç Ş, Yılmaz C (2010). The research of the behavior of the rigidity connections between columns in industrial buildings under the influence of temperature variation, earthquake and wind. *9th International Congress on Advances in Civil Engineering*, Karadeniz Technical University, Trabzon, Turkey.

Eyyubov C (1978). Binaların Depreme Dayanıklılığı. Azerbaijan State Publishing, Baku (in Turkish).

Eyyubov C (2011). Çelik Yapılar 1. Birsen Publishing, İstanbul (in Turkish).

Eyyubov C (2011). Çelik Yapılar 2. Birsen Publishing, İstanbul (in Turkish).

Eyyubov C, Genç Ş, Yılmaz C (2009). Sanayi binalarında kolonlar arası rijitlik bağlantılarının davranışlarının araştırılması. *TMMOB İnşaat Mühendisleri Odası, 3. Ulusal Çelik Yapılar Sempozyumu* (in Turkish).

Karataş ÇA, Çelik OC (2009). Burkulması önlenmiş çaprazlı çelik çerçeve sistemlerinin incelenmesi. *TMMOB İnşaat Mühendisleri Odası, 3. Ulusal Çelik Yapılar Sempozyumu* (in Turkish).

Melnikov NP (1980). Metallicheskie Konstruktsii, Spravochnik Proektirovshchika, Moscow (in Russian).

Süleymanov H (1971). Materialler Mukavemeti, Azerbaijan State Publishing, Baku (in Turkish).

Timoshenko S (1955). Strength of Materials. Van Nostrand, New York.

Wakabayashi M, Nakamura T, Kashibara A, Morizono T, Yokoyama H (1973). Experimental study of elasto-plastic properties of precast concrete wall panels with built-in insulating braces. *Proceedings of the Annual Convention of the Architectural Institute of Japan*, 1041–1044 (in Japanese).

Xie Q (2005). State of the art of buckling-restrained braces in Asia. *Journal of Constructional Steel Research*, 61(6), 727–748.